Proton Induced Gamma-ray Emission in the Analysis of Semiconductors and Energy Materials

By

YERROJU SUNITHA

CHEM01201504016

BHABHA ATOMIC RESEARCH CENTRE, MUMBAI

A thesis submitted to the
Board of Studies in Chemical Sciences
In partial fulfillment of requirements for the Degree of

DOCTOR OF PHILOSOPHY

Of

HOMI BHABHA NATIONAL INSTITUTE

June, 2020

Homi Bhabha National Institute[1]

Recommendations of the Viva Voce Committee

As members of the Viva Voce Committee, we certify that we have read the dissertation prepared by **YERROJU SUNITHA** entitled **Proton Induced Gamma-ray Emission in the Analysis of Semiconductors and Energy Materials** and recommend that it may be accepted as fulfilling the thesis requirement for the award of Degree of Doctor of Philosophy.

Chairman - Prof. P. K. Mohapatra		Date 4.9.2020
Convener - Prof. Sanjiv Kumar	Sanjiv Kumar	Date [illegible] 9 2020
Member 1- Prof. R. Acharya	Raghunath Acharya	Date 4/9/2020
Member 2- Associate Prof. R.H. Naina	Naina Raj.	Date 4/9/2020
Member 3- Asstt. Prof. K. K. Swain		Date 04.09.2020
External Examiner - Prof. Devinder Mehta (PU, Chandigarh)	D Mehta	Date 4/9/2020

Final approval and acceptance of this thesis is contingent upon the candidate's submission of the final copies of the thesis to HBNI.

I/We hereby certify that I/we have read this thesis prepared under my/our direction and recommend that it may be accepted as fulfilling the thesis requirement.

Date: September 04, 2020

Place: NCCCM / BARC, Hyderabad

Sanjiv Kumar
Prof. Sanjiv Kumar
(Guide)

---

[1] This page is to be included only for final submission after successful completion of viva voce.

Homi Bhabha National Institute

Ph. D. PROGRAMME

Letter of Recommendation

Name of the Student:	Smt. Y. Sunitha
Name of the Constituent Institution:	NCCCM, BARC
Enrolment No.:	CHEM01201504016
Viva-Voce Date:	4th September, 2020
Title of the Thesis:	Proton induced γ-ray emission in the quantitative elemental analysis of compound semiconductors and energy materials

Smt. Y. Sunitha appeared at her Viva Voce Examination on 4th September, 2020 through video conferencing. She presented a comprehensive account of her investigations. The development of two PIGE based methods for the determination of bulk oxygen in oxide semiconductors, the standardisation of methodologies for determining the isotopic ratio of boron, and their application to a large number of sintered and powder boron carbide specimens and the development of PIGE based methods for non-destructively depth profiling Li and Si in electrode materials of lithium ion battery and Si based semiconductors are the major outcomes of her investigations. These methods are robust and their applicability was established by analysing a large number of samples. Mrs. Sunitha has a sound understanding of the subject and answered the queries of the committee members eloquently. She also gave satisfactory answers to the queries raised by the external examiner(s) and researchers attending the Viva Voce.

In view of her comprehensive studies which are very large potential applications in the analysis of energy and semiconductor materials and her deep understanding of the subject, the doctoral committee recommends her for the award of Ph.D. from HBNI.

S. No.	Name	Designation	Signature	Date
1.	Prof. P. K. Mohapatra	Chairman		28-10. 2020
2.	Prof. Sanjiv Kumar	Guide/ Convener	Sanjiv Kumar	23·10·2020
4.	Prof. R. Acharya	Member	Raghunath Acharya	28/10/2020
5.	Associate Prof. R.H. Naina	Member	Naina Raje.	28/10/2020
6.	Asstt. Prof. K. K. Swain	Member		28·10·2020

STATEMENT BY AUTHOR

This dissertation has been submitted in partial fulfillment of requirements for an advanced degree at Homi Bhabha National Institute (HBNI) and is deposited in the Library to be made available to borrowers under rules of the HBNI. Brief quotations from this dissertation are allowable without special permission, provided that accurate acknowledgement of source is made. Requests for permission for extended quotation from or reproduction of this manuscript in whole or in part may be granted by the Competent Authority of HBNI when in his or her judgment the proposed use of the material is in the interests of scholarship. In all other instances, however, permission must be obtained from the author.

Y. Sunitha

(Y. Sunitha) 15/06/2020

DECLARATION

I, hereby declare that the investigation presented in the thesis has been carried out by me. The work is original and has not been submitted earlier as a whole or in part for a degree / diploma at this or any other Institution / University.

Y. Sunitha
15/06/2020
(Y. Sunitha)

Sanjiv Kumar
15.6.2020
(Prof. SANJIV KUMAR)
(Guide)

List of Publications arising from the thesis

Journal

a. Published:

1. "Oxygen determination in materials by $^{18}O(p,\alpha\gamma)^{15}N$ nuclear reaction", Sanjiv Kumar, **Y. Sunitha**, G.L.N. Reddy, A.A. Sukumar, J.V. Ramana, A. Sarkar, Rakesh Verma, *Nuclear Instruments and Methods in Physics Research B*, **2016**, *378*, 38–44.

2. "Depth profiling Li in electrode materials of lithium ion battery by $^{7}Li(p,\gamma)^{8}Be$ and $^{7}Li(p,\alpha)^{4}He$ nuclear reactions", **Y. Sunitha**, Sanjiv Kumar, *Nucl. Instr. Method, B*, **2017**, *400*, 22-30.

3. "$^{10}B/^{11}B$ isotopic ratio and atomic composition of boron carbide: determination by proton induced gamma-ray emission and proton elastic backscattering spectrometry", **Y. Sunitha**, Sanjiv Kumar, *Applied Radiation and Isotopes*, **2017**, *128*, 28-35.

4. " $^{18}O(p,p'\gamma)^{18}O$ nuclear reaction in the determination of oxygen by proton induced γ-ray emission", **Y. Sunitha**, Sanjiv Kumar, *J. Radioanal. and Nucl. Chem.*, **2017**, *314*, 1803-1812.

b. Manuscript in preparation:

1. "$^{28}Si(p,p'\gamma)^{28}Si$ nuclear reaction in the detection and depth profiling of Si in materials", **Y. Sunitha**, G. L. N. Reddy, Sanjiv Kumar, for submission in *Nucl. Instr. Method, B*

Other Publications:

Conference/Symposium:

1. Isotopic Analysis of Boron: Rapid and Non-destructive Determination by Particle Induced Gamma Ray Emission; **Y. Sunitha**, A.A. Sukumar, Sanjiv Kumar, Characterization and Quality Control of Nuclear Fuels (CQCNF), **December 1-3, 2015**; Hyderabad.

2. Determination of boron in Al-based materials by proton induced gamma-ray emission technique and nuclear reaction analysis; **Y. Sunitha**, A. Sarkar, G.L.N. Reddy, J. V. Ramana, Sanjiv Kumar; ETAC, **September 21-23, 2016**; AMDER, Bangalore.

3. Determination of atomic composition of silicon carbide by proton induced gamma-ray emission technique; **Y. Sunitha**, S. Kumar, 13th DAE-BRNS Nuclear and Radiochemistry Symposium (NUCAR-2017), February 6-10, 2017; KIIT Bhubneshwar.

4. Oxygen Determination by Particle Induced γ-ray Emission; **Y. Sunitha**, Sanjiv Kumar, 15th International Conference on Modern Trends in Activation Analysis (MTAA-15); **November 17-22, 2019**; BARC, Mumbai.

Y. Sunitha
15/06/2020

(Y. Sunitha)

Dedicated to my loving mother

ACKNOWLEDGEMENTS

First and foremost, I would like to express my sincere gratitude to my research guide **Prof. Sanjiv Kumar,** Head, National Centre for Compositional Characterisation of Materials (NCCCM), Hyderbad for the continuous support of my Ph.D. study and research. His guidance from the initial to the final level enabled me to develop an understanding of the subject and helped me in the timely submission of this thesis. I could not have imagined having a better guide and mentor for my Ph.D. study. He will always be a source of inspiration.

I am grateful to **Prof. A.K. Tyagi,** Associate Director, Chemistry Group, BARC, Mumbai for his support and encouragement.

I sincerely thank my colleagues at NCCCM: Dr. J.V. Ramana, Dr. G.L.N.Reddy, Shri A.A. Sukumar for helping me during experiments and the preparation of the thesis. Thanks are also due to Shri P.V.Kiran Kumar, Shri G. Srikanth, Shri V.N. Shinde, Mrs.P.N. Padmavathi and other colleagues at NCCCM for their co-operation in their own ways during the course of my work. I also express my sincere thanks to Shri U.L.K. Prasad and J. Shanker for their help during experiments. I would also like to thank my colleagues Dr. Remya Devi and Dr. Madhusudhan at ACD, BARC for their support. Thanks are also due to Dr. K. K. Swain and Dr. Rakesh Verma for their valuable suggestions and help on several fronts.

I would like to thank my **family** for all their encouragement. My **parents** deserve special mention for their support in all walks of my life; I owe my every achievement to them. I also thank my sister Sujatha, my brother-in-law (Late) Praveen Kumar, and nephews Supraj and Harsha. I would also like to thank my parents-in-law for their support. I would like to thank my childhood mentor Shri. Rajender Kumar, DRDL for his constant support.

I express my appreciation to my husband Dheeraj Kumar Sahu, son Suraj and daughter Akshara for their persevering encouragement and affection. It would have been extremely difficult to carry out the work without their constant support.

Lastly, I would like to thank everybody who was important to the successful realization of this thesis, as well as expressing my apology that I could not mention everyone personally.

CONTENTS

Summary

Ion beam analysis (IBA) is an important tool for compositional investigations in the surface and near-surface regions of materials. It is unique among surface analytical techniques by virtue of its sensitivity towards several elements, light or otherwise, across the periodic table and non-destructive depth perception capability. It is performed using energetic beams of protons, α-particles or heavy ions extracted from accelerator as probes and represents an array of techniques which are classified on the basis of the nature of the interaction of ions beams with matter. Rutherford Backscattering Spectrometry (RBS), Nuclear Reaction Analysis (NRA), Particle Induced X-ray Emission (PIXE), Particle Induced Gamma-ray Emission (PIGE) are some of the important IBA techniques. Amongst these, PIGE holds an important position by virtue of several features which includes its multi-elemental detection capability, sensitivity to low z elements and capability to analysis bulk materials and thin films as well. Consequently it has been extensively utilized for the analysis of a wide variety of materials. However its applications to compound semiconductors and energy materials are rather limited. The investigations conducted during the course of this doctoral work programme have employed PIGE (proton) to the analysis of these two important class of materials. The analysis encompasses the determination of the depth distribution and or the bulk content of one or more constituents of the materials. Two methods involving $^{18}O(p,p'\gamma)^{18}O$ and $^{18}O(p,\alpha\gamma)^{15}N$ nuclear reactions were developed that enable a precise determination of bulk oxygen in several oxide semiconductors. In an equally important study, methods for depth profiling lithium in lithium ion battery (LIB) materials were formulated and standardized. With a probing depth of more than twenty microns and a few at% detection sensitivity the methods that utilize $^{7}Li(p,\gamma)^{8}Be$ and $^{7}Li(p,\alpha)^{4}He$ reactions, can be suitable substitutes to neutron depth profiling which is the most preferred used technique for depth profiling Li in materials. Similarly a method for depth profiling Si in silicon nitride and silicon carbide has also be established. In addition, a portion of the thesis dwells on the analysis of boron carbide wherein methodologies for the determination of B/C ratio and $^{10}B/\ ^{11}B$ ratio are described. The methods are unique, rapid and precise and especially applicable to sintered specimens. In essence, the investigations led to the formulation and standardization of PIGE based methodologies that are eminently suitable for analysing different carbides and oxides, Si-based compound semiconductors and Li ion battery materials.

List of Figures

List of Tables

Homi Bhabha National Institute

Ph. D. PROGRAMME

Name of Candidate: Yerroju Sunitha

Name of the Constituent Institution: Bhabha Atomic Research centre, Mumbai

Enrollment Number: CHEM01201504016

Title of the Thesis: Proton Induced Gamma-ray Emission in the Analysis of Semiconductors and Energy Materials

Thesis highlights:

- Bulk determination and depth profiling in advanced materials
  - ✓ Compound semiconductors : Nitrides and oxides
    - ➢ Bulk determination of oxygen in binary and multinary oxides
    - ➢ Depth profiling of Si
  - ✓ Energy materials : Lithium ion battery, boron carbide
    - ➢ Depth profiling of Li
    - ➢ Bulk determination of B and C and $^{10}B/^{11}B$ ratio

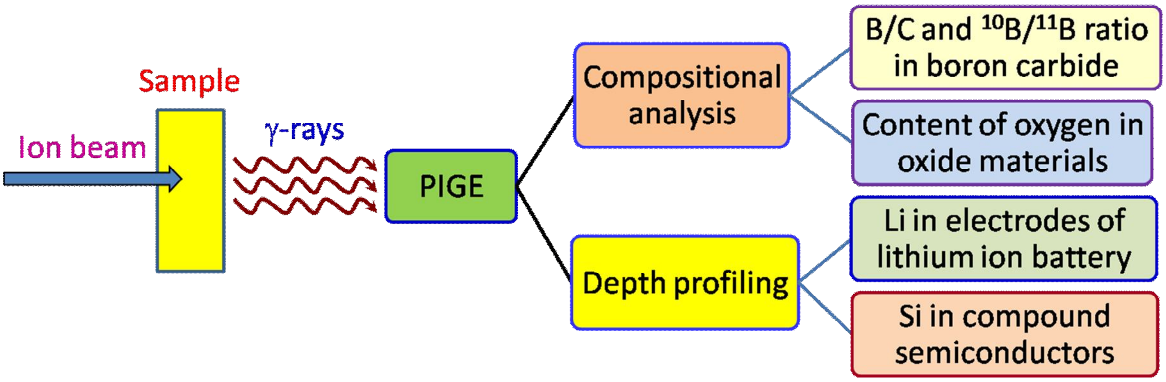

Chapter 1

Introduction

1.1 Introduction

The modern age is an age of materials. Materials have played an important role in the evolution of the modern civilization. The journey of the mankind from the primitive ‘stone age’ to the current ‘space age’ is, in fact, a journey of materials. Materials are ubiquitous: these have touched almost every aspect of human life and will continue to be a dominant force in shaping the future of humanity **[1-4]**. The evolution or the growth of materials, be it semiconductor, superconductor, magnetic, optical or nuclear, on the other hand, is itself, a result of concerted scientific investigations. Synthesis and characterisation of materials have been the main focus of such investigations.

A material with tailor-made properties or of a definite functionality can be prepared by a specific and well standardised synthetic procedure which, in turn, can be established only through a comprehensive study **[5-7]**. In view of the requirements of new and special materials that kept emerging, particularly since the beginning of the last century, for technological advancements, a wide range of methods of synthesis has been developed. For example, a material in powder form can be synthesised either through solid state route or by a wet-chemical method while as thin films, it can be prepared by one of the numerous thin film deposition techniques **[8-10]**. The products, in an additional step, are often subjected to chemical, mechanical or thermal treatments that may involve sintering and or oxidative/reductive annealing. The synthetic procedure, the parameters associated therewith and the conditions of processing have a profound influence on the chemical, physical and or metallurgical properties, and, a result, on the applications of the materials **[11]**. The properties are, in fact, the manifestations of the compositional and the structural features the materials acquire during the synthesis and processing stages. A study on composition-structure-property correlation vis-a-vis synthesis therefore forms the most important component of any material development programme.

Composition lies at the root of the chemistry of materials. It defines both qualitatively as well as quantitatively the elements constituting a material. The elements, in general, are those represented in the chemical formula of the material but may also include extraneous elements, termed as impurities prevailing therein in low concentrations. It is important to note that the terms “composition” and “stoichiometry” are sometimes interchangeably used in literature. Stoichiometry, however, strictly symbolises the quantitative relationship or correlation between the elements in a material according to its chemical formula and does not describe any impurity profile. Any deviation from the nominal stoichiometry introduces “non-stoichimetry” in the material which is classified into “sub” or “super” stoichiometry depending on the fact that the content of an element is deficient or excess in comparison to the one prescribed by the chemical formula. Although the synthesis of stoichoimetric materials is desirable, non-stoichiometry imparts novel properties to many materials and plays a defining role in governing their functionalities and applications **[12,13]**. Non-stoichiometric oxides are a typical example of this class of materials **[14-18]**. Notably, the non-stoichiometry can be introduced in the materials either through an aliovalent substitution during synthesis or in a separate post synthesis step that may involve annealing in reducing conditions. So far as the impurity elements the other component of composition is concerned, these may either be present inherently, having their origin in the chemicals/ synthetic procedure or are added intentionally to introduce a desired property in the material. The concentration of the impurities can range from ppm to down to ppt levels.

1.2 Energy and Semiconducting materials

Clean and sustainable energy is the need of the hour in the wake of rapidly depleting conventional sources of energy and the continually deteriorating climatic conditions resulting essentially from their wanton and extensive usage. Renewable energy sources such as solar, wind, hydelpower, biomass, geothermal etc. are expected to reduce our dependence on the conventional sources and are tipped to provide sustainable energy services **[19]**. Energy storage is also a key component in providing sustainable energy particularly in view of fluctuating energy sources such as wind and sunlight.

1.2.1 Lithium ion battery

Batteries are widely used for energy storage. Amongst the different kinds of batteries, the lithium ion battery (LIB) has revolutionized the energy storage technology and hence occupies a prominent position **[20]**. A LIB, by virtue of their high potential, high energy density and also capacity is the lifeline of the modern portable gadgets, providing them power in unbound and wireless ways. Not stopping here, the LIB is fast becoming the power source of electric vehicles. The importance of energy storage by LIB and its impact on human life is best underlined by the fact that J. B. Goodenough, M.S. Whittingham and A. Yoshino were awarded the Nobel Prize in chemistry in 2019 for the development of LIBs **[21-24]**.

A LIB is an electrochemical device that consists of a cathode (+ve electrode), an anode (-ve electrode), an electrolyte and a separator that prevents the cathode and the anode from coming into physical contact. The cathodes are usually made up of $LiCoO_2$, $LiFePO_4$, $LiMn_2O_4$ etc. while, the anode is invariably made up of graphite **[20,25,26]**. A solution of a lithium salt in an organic solvent serves as the liquid electrolyte. $LiPF_6$, $LiBF_4$, $LiAsF_6$ are some typical examples of such lithium salts where as dimethyl carbonate or ethylene carbonate are among the solvents most frequently used. Separators which as described earlier, prevents short circuit to occur are made up of microporous polyefin materials based polymeric membranes **[20,27]**. A schematic of typical LIB consisting cathode, anode and electrolyte is shown in **Fig. 1.1.**

The commercial cells are usually are assembled in discharged state. These need to be charged for delivering power. During the charging process, the electrons are released at the cathode which move externally to the anode while, lithium ions move internally to the anode through the electrolyte. In this way, the external energy is electrochemically stored in the battery in the form of chemical energy in the anode and cathode with different chemical potential. During discharging (supplying power), the electrons move from anode to cathode through the external load and lithium ions move internally from anode to cathode **[20]**.

The electrochemical reactions taking place at the two electrodes can be summarized as

at cathode: $$LiCoO_2 \rightarrow 0.5Li^+ + 0.5e^- + Li_{0.5}CoO_2 \qquad (1.1)$$

at anode: $$Li^+ + e^- + C_6 \rightarrow LiC_6 \qquad (1.2)$$

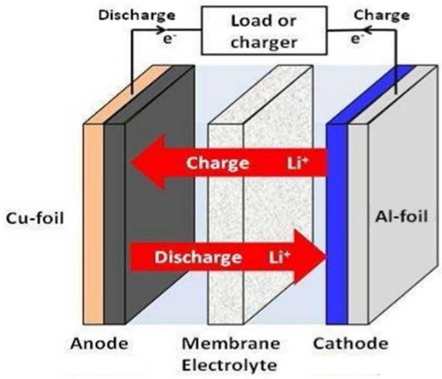

Fig. 1.1: *A schematic of lithium ion battery consisting anode, cathode and electrolyte*

A knowledge of the depth distribution of Li in the anode as well as the cathode of a LIB is essential for a comprehensive understanding of Li transport, and lithiation and delithiation–the basic processes involved in the working of the device **[28]**. It assumes even greater importance while efforts are underway to extend the application of LIB, after a hugely successful usage in consumer electronics, to electric vehicles. Capacity fade - the loss of capacity over time - is a major deterrent in the application of the energy device in this area **[29,30]**. The deterioration in capacity is closely related to the composition and morphology of the solid electrolyte interphase (SEI) existing at the boundary of the anode and the electrolyte, and the concentration profile of Li in the functional layers. Neutron depth profiling (NDP) has often been employed for depth profiling Li in the electrodes, though there are instances of application of mass spectrometry and spectroscopic techniques such as secondary ionisation mass spectrometry and glow discharge optical emission spectroscopy as well **[31-34].**

1.2.2 Materials for nuclear energy

Boron carbide is a non-metallic material and has high neutron absorption cross section for thermal neutrons (~3800 barns), attributable to the ${}^{10}B(n, \alpha){}^{7}Li$ nuclear reaction **[35-38]**. Hence, boron carbide enriched in ${}^{10}B$ isotope is used as control rods in nuclear reactors. It has a band gap of ~ 2.09 eV and displays good thermoelectrical properties as well **[39,41]**. Some of elements and their thermal neutron absorption cross-sections **[42]** are given in **Table 1.1.**

Table 1.1. *Elements and their thermal neutron absorption cross-section*

Element	Isotope	Abundance (%)	Thermal neutron absorption cross-section (barns)
Boron	Natural	100	750
	${}^{10}_{5}B$	20	3800
Cadmium	Natural	100	2450
	${}^{113}_{49}Cd$	12.26	20,000
Samarium	Natural	100	5600
	${}^{149}_{62}Sm$	13.84	40,800
	${}^{152}_{62}Sm$	25.63	244
Europium	Natural	100	4300
	${}^{151}_{63}Eu$	47.77	7700
	${}^{153}_{63}Eu$	52.23	450
Gadolinium	Natural	100	46,000
	${}^{155}_{64}Gd$	14.73	60,000
	${}^{157}_{64}Gd$	15.68	240,000
Dysprosium	Natural	100	950
	${}^{164}_{66}Dy$	28.18	2600
Iridium	Natural	100	440
	${}^{191}_{77}Ir$	38.5	960
	${}^{193}_{77}Ir$	61.5	130
Mercury	Natural	100	380
	${}^{199}_{80}Hg$	16.8	2500

Boron carbide is a non-stoichiometric compound. It exists over a large homogeneity range extending from about B_4C, or according to some researchers, $B_{4.3}C$ at the carbon-rich to $B_{12}C$ at the boron-rich limit **[43-46]**. The mechanical and thermoelectrical properties of boron carbide are profoundly influenced by the carbon content in the ceramic **[47,48].**

Hence the determination of the B/C ratio of the ceramic is required for the optimization of the synthetic conditions for preparing ceramics with requisite properties.

Li_2TiO_3 is a leading candidate material for breeding tritium (T) by way of $^{6}Li(n, \alpha)T$ reaction in a fusion reactor. Incidentlly, $Li_4Ti_5O_{12}$ is eminently suitable for applications as anode in lithium-ion batteries. These two are prominent compounds of the Li_2O-TiO_2 binary system that is characterized by several phases which find applications in different areas **[49]**.

The determination of the elemental composition of lithium titanate ceramics is important not only from the point of view of optimisation of synthetic and processing parameters but also due to the fact that the structural and electrical properties of the material depend considerably on its composition. It is to be noted that non-stoichiometry has a profound influence on these properties of the material **[16]**. The elemental analysis of lithium titanate, however, is challenging due to its refractory nature and low z constituents. The inapplicability of conventional analytical techniques in oxygen analysis is well known. The difficulty in the dissolution of sintered ceramics is an additional problem encountered in these methods. Amongst the instrumental techchiques, the X-ray methods, which are widely used for elemental analysis in materials science, suffer from the limitations of low production and high attenuation of Li (K_α= 54 eV) and O (K_α= 525 eV) X-rays. The mass spectrometry techniques, on the other hand, are destructive in nature and the process of sputtering generally employed for the removal of analytes can cause an alteration in the atomic composition in the surface layers **[50]**.

1.2.3 Semiconductors and dielectrics

Semiconductors and dielectrics are important class of materials that find applications in numerous fields. The following **Table 1.2** illustrates the classification as metals (conductors), semiconductors and insulators (dielectric) according to their electrical resistivity.

***Table 1.2:** Materials and their electrical resistivity*

Classification of materials	Resistivity (Ω.cm)
Metals	10^{-6} to 10^{-2}
Semiconductors	10^{-3} to 10^{6}
Insulators	10^{7} to 10^{20}

In terms of band theory, the classification of these materials can be pictorially (**Fig.1.2**) represented as metals, semiconductors and insulators **[51]**.

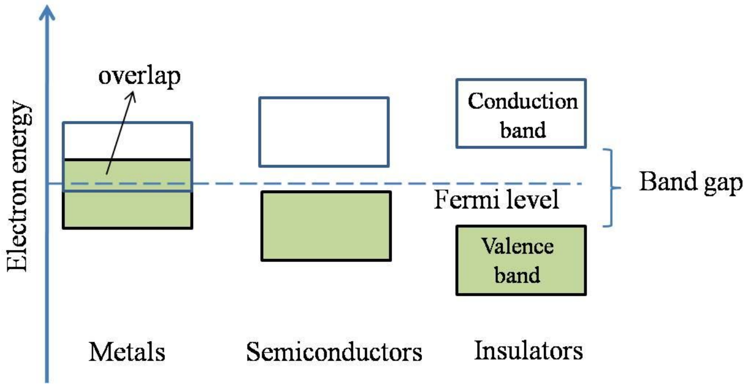

***Fig.1.2:** Metals, semiconductors and insulator in terms of band theory*

The band gap that represents the energy difference between the valence band and conduction band is about 3 eV for semiconductors and > 3eV for insulators. However this criterion for differentiating semiconductors and dielectric materials is somewhat arbitrary as, at times materials with band gaps > 3 eV are also classified as semiconductors. It is instructive to mention that the semiconductors band gap more than 2.5eV are known as wide band gap semiconductors. Semiconductors can be elemental or compound in terms of chemical composition. Si and Ge with a band gap of 1.14 and 0.67 eV respectively are the most important elemental semiconductors. The list of compound semiconductors, on the other hand, is varied and exhaustive **[51,52]**.

Silicon carbide with band gap of 3-7 eV is a typical example of a wide band gap semiconductor. It is a ceramic and is well suited for high temperature operations and finds applications in turbine engines of aircrafts, nuclear power instrumentation etc. AlN, GaN, BN are some premier wide band gap semiconductors for such applications. The properties of silicon carbide depend on its composition. In general, Si-rich composition facilitates improved sintering of the material. Si-SiC exhibit n-type conductivity while C-SiC exhibit p-type conductivity. Both C-SiC and Si-SiC have thermal conductivity higher than SiC **[53]**.

Barium titanate is one of the most important ferro-electric material. It has a perovskite structure and displays several interesting electrical properties. Barium titanate as such is an insulator that acquires n-type semiconductivity on doping with donors such as Sb^{+5} in 0.2 to 0.5 at% concentration. Such n-type barium titanate exhibits positive temperature coefficient of resistivity (PTCR) effect **[54]**. This property of barium titanate has been utilized in making several important electrical gadgets.

Barium titanate exhibits polymorphism with several phases such as hexagonal phase stabilizing at high temperature. However such dopants as managanese have been shown to bring about considerable oxygen non-stoichiometry which stabilize hexagonal phase at room temperature. Titania rich barium titanate, (Ti/Ba>1), known as barium polytitanates are of considerable interest for microwave dielectric applications. Barium tetratitanate ($BaTi_4O_9$) and barium nonatitanate ($Ba_2Ti_9O_{20}$) are two important examples of this class of materials **[55]**.

1.3 Methods of analysis: Wet chemical and Instrumental

The compositional analysis of materials that includes the determination of major, minor and trace elements can be performed by different chemical methods. The analysis can be conducted in solid state or after their dissolution in a suitable medium. GDMS **[56]** is a typical example of methodologies wherein the analysis is performed on solid materials without any treatment. However, such methods are few in number. Generally wet chemical methods are employed for analysis. The analysis is performed using instrumental techniques which vary in their degree of sophistication. Atomic absorption spectroscopy (AAS) **[57,58]** and atomic emission spectroscopy (AES) **[59]** are the most widely used methods for chemical analysis. The major variants of this class of methods are graphite furnace atomic absorption spectroscopy (GFAAS) **[60]** and inductively coupled plasma optical emission spectroscopy (ICP-OES) **[61,62]**. Inductively coupled plasma mass spectrometry (ICP-MS) **[61-63]** is the most popular instrumental technique for the determination of elements and impurities at trace and ultra trace levels. Besides spectroscopic techniques, spectrophotometry and electro analytical techniques such as voltametry, potentiometry are also utilised for analytical purposes**.** However most the instrumental techniques working on liquid samples are not suitable for the determination of low z elements such elements as C, N, O, F etc. The analysis of the samples by wet chemical methods can at times be challenging mainly due to the problems associated with sample dissolution. For sensitive determination blank and likely interferences from the matrix are two major considerations. Therefore analysis of high purity materials wherein the impurities are present in trace and ultractrace levels are carried out in a special clean laboratories equipped with class 10 and class 100 facilities. To achieve the desired sensitivity and to eliminate the interference from the matrix, the trace elements are separated from the matrix using the well defined chemical methodology. The working principles of these instrumental techniques and their applications can be obtained from references **[50,64,65]**.

1.4 Surface analytical techniques

Surface analysis is an important aspect of the modern science and technology. The properties of the surfaces are different from those of prevailing in the bulk of materials. The surfaces are the regions through which a material interacts with the surrounding materials. It is also the region where the processes occurring in the bulk culminate. Therefore the elemental composition and also the chemical environment are different from those prevailing in the bulk. The surfaces beginning from the top are usually in the range of few nm to few microns in thickness **[66]**. Thin films are also considered to be a typical example of surfaces. To probe the surface regions of the materials and thin films in terms of their elemental composition, morphology, defects and crystal structure, a large number of techniques have been developed in the past few decades. Most of the techniques are extremely sophisticated and have significantly different instrumentation in comparison to the bulk analysis techniques described in the pervious section. The surface analytical techniques usually analyse solid samples and work in high / ultra-high vacuum conditions. Some of these are destructive while some are non-destructive in nature. Though these techniques are used for quantitative analysis, the sensitivity and precision are poor in comparison to the wet chemical methods. The surface techniques however are sensitive to a wide range of elements including low z elements such as H, B, C, N, O, F etc. and can provide depth profile information **[50, 64,65,67]**. These techniques are eminently suitable for the analysis of multilayered films that find applications in different areas such as optical coating and solar cells. A few of the surface analytical techniques are described in the following sections.

1.4.1 X-ray photoelectron spectroscopy (XPS)

XPS is also known as electron spectroscopy for chemical analysis (ESCA), is a powerful surface analytical technique with a probing depth of 10-50Å. It is based on photoelectric effect and involves high resolution energy analysis of photoelectrons emitted from the sample surface on its irradiation with characteristic X-rays, mostly Al K_α (1486.6 eV), Mg K_α (1253.6 eV) or synchrotron radiation **[50,68,69]**. XPS is a non-destructive, simultaneous multi-element technique, sensitive to all elements other than H and He. A unique technique of its kind, it is performed in ultra-high vacuum (10^{-9} torr or better) and provides information on the chemical states of elements constituting the surfaces.

The kinetic energy of the electron emitted is related to the energy of the exciting X-ray radiation (hυ) by the equation

$$\text{K.E.} = \mathrm{h}\upsilon - B.E. - \Phi_{sp} \qquad (1.3)$$

where B.E. is the binding energy of the electron and ϕ is the work function of the spectrometer which is typically 2 - 5 eV. The binding energy of core electron in an atom depends on its chemical environment. Any change in the chemical environment, will bring about a change in the B.E. of an electron. The difference in the B.E. of an electron in an element and in a compound is termed as chemical shift, which can be in 0.5 to 5 eV range. The chemical shift is very useful in the identification of chemical state. XPS gives the information about the chemical state by measuring the chemical shift.

1.4.2 Glow discharge mass spectrometry (GDMS)

GDMS is an important solid state analysis technique sensitive to large number elements across the periodic table. It can determine the elements over a wide concentration range i.e, from percentage to down to ultra trace level **[56]**. The technique utilizes a glow discharge typically obtained using Ar gas to cause atomization of the elements constituting the samples followed by their ionization by way of electron impact or Penning ionization. The atomization and ionization are separated in space and time and therefore the technique is considered to be largely independent of matrix. The ionized atoms are analysed by a mass spectrometer, quadrupole or time-of-flight for obtaining the information on the nature of constituents and their nature. The technique is destructive in nature and the quantification is obtained by invoking the concepts of ion beam ratios (IBR) and relative sensitive factors (RSF). In addition to bulk analysis, GDMS can also be utilized for depth profile measurements with nanometric depth resolution. However the lateral resolution is poor and is often in the order of 1 – 8 mm. The technique is mainly utilized for the analysis of electrically conducting samples.

1.4.3 Secondary ionization mass spectrometry (SIMS)

SIMS is the most powerful mass spectrometric technique for surface and the profile analysis of elements at trace and ultra-trace levels. SIMS utilizes energetic ion beams (upto 30 keV) as the excitation source and involves mass analysis of the secondary ions produced **[70]**. The energy of the secondary ions is independent of the energy of the primary ions and usually in the order of 10eV. The primary ions commonly used are Cs^+, O_2^+, Ar^+, $Xe^+$and Ga^+. In comparison to the noble gas primary ions such as $Ar^+$and Xe^+ ions, the use of O_2^+ ions increases the ionization probability of species that tend to form cations and the use of Cs^+ ions, that of anions. In another words, positive or negative secondary ions are analysed in this technique. For example the sensitivity of Zn, As, Se, Pt, Au etc ions is comparatively higher for O_2^+ ions while, for Fe, Co, Zr, Mo, Pd, W etc ions is comparatively higher for Cs^+ ions. In addition to these, neutral species are also emitted from the sample surface on the bombardment with the primary ions. The mass analysis of the neutrals forms the basis of yet another mass spectrometric technique, known as sputtered neutral mass spectrometry (SNMS). SIMS can be operated in two modes namely dynamic and static. In dynamic SIMS, the number of incident ions exceeds the number of surface atoms on the sample. In contrast, in static SIMS, measurements are performed with a number of incident atoms ($<10^{12}$ ions/cm^2) and hence in this mode the damage to the sample surface is minimum. For mass analysis usually time-of-flight analysers are preferred though double focusing magnetic sectors or quadrupole mass analysers are also used.

The quantification by SIMS is a difficult process since the intensity of secondary ions depends on a number of factors that include the type and the energy of the primary ions and the angle of incidence. The quantification can be best carried out using matrix matching standards. SIMS is very useful technique for depth profiling with very good depth and lateral resolutions. SIMS is destructive in nature.

1.4.4 Auger electron spectroscopy (AES)

AES is an important surface analytical technique with a probing depth of 3-10Å. It involves high resolution energy analysis of Auger electrons emitted as a result of irradiation of a material with a beam of electrons **[69]**. The schematic of the ejection of Auger electrons is shown in the **Fig 1.3.** The electrons incident on the atom creates a vacancy in one of the inner shells of the atom. The vacancy decays through radiative or non-radiative process. The radiative process entails the emission of characteristic X-rays, while, in non-radiative process, secondary electrons i.e, Auger electrons are emitted. The emission of Auger electrons takes place when the characteristic X-rays produced in the radiative process are absorbed by the electrons of the higher energy orbitals and are ejected. The emission of characteristics X-rays and that of Auger electrons are competitive processes. The emissions of Auger electrons is favoured in low Z elements while that of X-rays in high Z elements. Aguer electron spectroscopy is two hole process and similar to XPS exhibits the process of chemical shift. However it is not used for chemical state identification. Since it is performed with electrons it is often used for investigating segregation and micro-area elemental distribution.

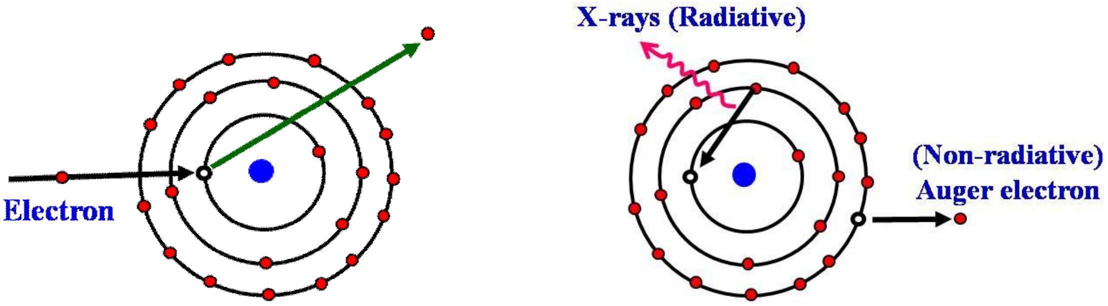

Fig 1.3: *Schematic of Auger electron production*

1.4.5 Neutron activation analysis (NAA) and Charge particle activation analysis (CPAA)

NAA is an isotope specific nuclear analytical technique for the quantitative and qualitative analysis of materials. It is based on high resolution γ-ray spectrometry of radionuclides produced on the irradiation of stable nuclei with thermal neutrons **[65,71]**. The schematic of the formation of the radionuclides and the emission of γ-rays involved in NAA is shown in **Fig 1.4**.

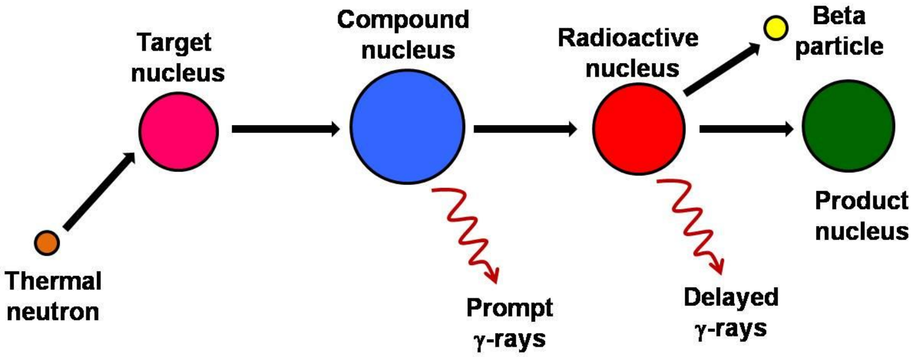

Fig 1.4: *Schematic of neutron activation analysis*

NAA is a simultaneous multi-element technique capable of analysing (bulk) solid, liquid and gaseous sample. It is a non-destructive technique and exhibits high sensitivity (ppm/ppb) for several mid and high z elements. However, it is not suitable for low z elements such as H, He, B, C, N, and O and also for some high z elements such as Tl, Pb and Bi.

There are two approaches to conduct NAA. In the first approach, the γ-ray spectrometry is performed on the irradiated samples without any sample processing step. This approach is known as instrumental neutron activation analysis (INAA). In the second approach, the samples after irradiation are treated chemically to remove spectral interferences or to minimise activity arising from the constituents other than analytes. This approach is known as radiochemical neutron activation analysis (RNAA). It is to be noted that the radionuclides are characterised by unit decay constant (half life) and energy of emitted particles that include γ-ray as well. These features enable the identification and quantification of radioisotopes and in turn the parent nuclei or element. The radionuclides (emitting γ-rays) can also be produced on irradiation with ion beams. This lays the foundation of charged particle activation analysis (CPAA) which is yet another nuclear analytical technique for the determination of elements **[72,73]**. Herein, the particle can be proton, deuteron, triton, ^{3}He or ^{4}He particles having energies in 5 MeV to 50 MeV. Apart from the source of the irradiation, the other aspects of the measurements remain largely identical to those of NAA. This technique is more suitable to low z elements like O, C though applications to mid z elements like Fe are also reported in literature **[68]**.

1.5 Ion beam analysis (IBA)

Ion beam analysis (IBA) is an important tool for compositional analysis of materials. It has been used extensively for elemental and stoichiometric analysis in the surface and near surface regions of materials [74]. It is unique among surface analytical techniques by virtue of its sensitivity towards several elements, light or otherwise, across the periodic table and non-destructive analyses, determination of depth profiles and diffusion parameters and defect analysis in materials that find applications in fields ranging from nuclear industry and semiconductor technology to environmental science and archaeology.

Ion beam analysis refers to the analysis of materials conducted using energetic ion beam as probes. The ion beams can be of protons, deuterons, alpha particles or any other heavy ions with energies ranging from 0.1 MeV to 5 MeV. The energetic ion beams are obtained from a particle accelerator. The ion beams interact with the target materials in multiple ways. The interactions can be nuclear or non-nuclear in nature. Some of these interactions can be exploited for analytical studies and form the basis of ion beam analysis. Apparently, ion beam analysis is an array of techniques, classified primarily on the basis of the nature of the interaction between the incident beam and the target nuclei/atoms and are known accordingly. However, before describing the processes that lay the foundation of the different ion beam techniques, it is important to mention that whether the process is nuclear or non-nuclear, ion beam analysis always entails an interaction between two nuclei, one belonging to the incident beam and the other, to the target element. Thus it is pertinent to present a brief account of some basic concepts, innate to such an interaction, first. It is equally important to note that nuclear reaction is central to ion beam analysis **[65,68]** and, therefore, the key aspects of the process, energetics in particular, are presented as well.

1.5.1 Interaction of ion beams with target nuclei: nuclear reaction and some basic concepts

Lord Rutherford discovered the presence of the nucleus in an atom in 1906 and later, in 1911, discovered the phenomenon of nuclear reactions. A nuclear reaction is a process in which a nucleus reacts with another nucleus, an elementary particle or a photon to produce within 10^{-12} sec or less one or more other nuclei, and possibly other particles **[74,75]**. It can be symbolically presented as A(a,b)B and pictorially as in **Fig 1.5.**

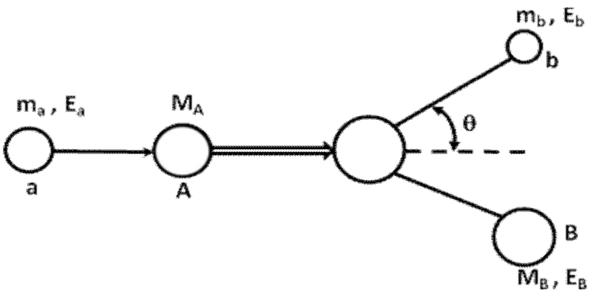

Fig 1.5: *Schematic of a nuclear reaction A(a,b)B*

wherein particle a of mass m_a and energy E_a, often termed as projectile is incident on another nucleus A, of mass M_A and supposedly at rest in laboratory frame of reference and often termed as target, while b, B are the light and heavy reaction products respectively.

A nuclear reaction like a chemical reaction is usually accompanied by a release or absorption of energy and thus is better represented by

$$a + A \rightarrow b + B + Q \qquad (1.4)$$

where Q is the energy absorbed or released and is often known as “Q” of the reaction. The Q of the reaction is given by the relationship

$$Q = (m_a + M_A - m_b - M_B)\, c^2 \qquad \text{or}$$

$$= 931.5\,(m_a + M_A - m_b - M_B)\ \text{MeV} \qquad (1.5)$$

where m_a, M_A are the atomic mass units of a (projectile) and A (target) and m_b, M_B are that of b (light reaction product) and B (heavy reaction product) respectively.

In a nuclear reaction total energy, momentum, angular momentum, statistics and parity are conserved. A nuclear reaction is better represented as

$$ {}^{m_a}_{z_a}a + {}^{M_A}_{Z_A}A \rightarrow {}^{m_b}_{z_b}b + {}^{M_B}_{Z_B}B \qquad (1.6) $$

If the Q value of the reaction is negative, the reaction is referred to as endoergic and if Q is positive, reaction is termed as exoergic and kinetic energy gained in the reaction.

$^{14}N(\alpha,p)^{17}O$, the first nuclear reaction to be discovered by Lord Rutherford and $^{14}N(^{2}H, p)^{15}N$ are the typical examples of endoergic and exoergic nuclear reactions with the Q-values of -1.193 MeV and 8.61 MeV respectively **[74,75]**. The energetic (i.e. Q value) of these two reactions can be pictorially represented in **Fig 1.6** and **Fig 1.7**

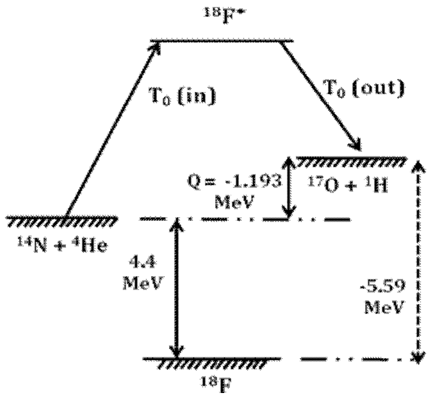

***Fig 1.6**: Energetics of $^{14}N(\alpha,p)^{17}O$ endoergic nuclear reaction*

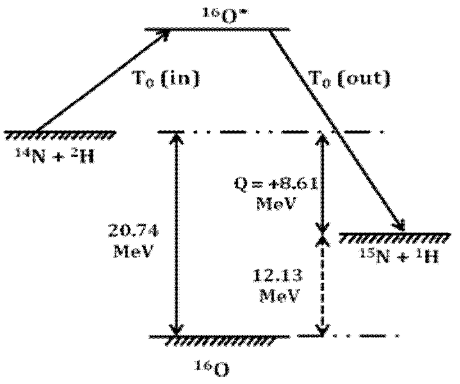

***Fig 1.7:** Energetics of $^{14}N(^{2}H,p)^{15}N$ exoergic nuclear reaction*

1.5.1.1 Threshold energy and Coulomb barrier

As mentioned earlier a nuclear reaction can be induced by neutrons or charged particles such as proton, α-particle or a photon (eg.γ-rays). In the present study, only charged particles, that too mostly protons have been used as the projectiles. For inducing a nuclear reaction, the charged particle (projectile) must overcome the coulomb barrier that exists between the nuclei of the charged particle and the target. The potential barrier (V_c) is expressed by the following equation

$$V_C = \frac{z_1\, z_2\, e^2}{(R_1 + R_2\ )} \quad \text{MeV} \qquad (1.7)$$

where z_1, z_2 are the atomic numbers and R_1, R_2 are the radii represented by $1.5A_i^{1/3}$, where A_i is the mass of the nuclei.

There is a threshold energy, E_{th} for the incident particle below which an endoergic reaction cannot occur. The threshold energy is always greater than |Q| and is given by the relationship

$$E_{th} = Q \frac{M_B + m_b}{(M_B + m_b - m_a)} \qquad (1.8)$$

The Q value, the coulomb barrier and the threshold energy of the reactions $^{14}N(\alpha,p)^{17}O$ and $^{14}N(^2H, p)^{15}N$ are given in the **Table 1.3.**

Table 1.3. *Q value, the coulomb barrier and the threshold energy of $^{14}N(\alpha,p)^{17}O$ and $^{14}N(^2H, p)^{15}N$ nuclear reactions*

Nuclear reaction	Q(MeV)	Coulomb barrier (MeV)	Threshold energy (MeV)
$^{14}N(\alpha,p)^{17}O$	-1.193	3.4	1.53
$^{14}N(^2H, p)^{15}N$	8.61	1.92	-

The reactions having Q values > coulomb barrier will occur at all energies of the projectile. Endoergic reactions characterized by $V_c < E_{th}$ will be induced by particle with energy > E_{th}. The $^{14}N(\alpha,p)^{17}O$ reaction incidently presents an interesting case since $V_c > E_{th}$. Herein, according to the principle of conservation of momentum, α- particles must have at least 4.4 MeV energy to induce the nuclear reaction even as the threshold energy of the reaction is 1.53 MeV. However, as per quantum mechanical treatment, there is a finite probability for the occurrence of the reaction at any energy above 1.53 MeV. But the cross-section of the reaction at lower energy is less and increases with the increase of energy of the α-particles to 4.4 MeV and still higher **[74,75]**.

1.5.2 Classification of nuclear reactions

The interaction between the projectile 'a' and the target 'A' can lead to several nuclear reactions which can be broadly classified into the following categories **[68,75,76]**

(a) Elastic scattering, (b) Inelastic scattering, (c) Coulomb excitation, (d) Radiative capture and (e) Re-arrangement collisions

(a) Elastic scattering

An elastic scattering or collision is the simplest nuclear reaction wherein the projectile and the targets are not modified by the interaction. Thus an elastic scattering can be represented by the equation

$$a + A \rightarrow A + a \; (Q = 0) \qquad (1.9)$$

Apparently both the momentum and kinetic energy are conserved in the process. It can be initiated with the projectiles of any energy and may involve Coulombic repulsions or complicated nuclear interactions. When Coulomb forces are more dominant, the process is known as Rutherford backscattering (RBS). RBS is an important analytical technique for the surface analysis of materials. It has been used on few occasions the present studies. The principles of RBS are presented in **Section 1.8**.

(b) Inelastic scattering

In an inelastic scattering the projectile and the target nuclei retain their identity in the interaction. However, the target is left in an excited state, which subsequently de-excites to the ground state with the emission of γ–rays.

$$a + A \rightarrow A^{*} + a + Q \; (Q < 0) \qquad (1.10)$$

$$A^{*} \rightarrow A + \gamma \qquad (1.11)$$

(c) Coulomb excitation

The prompt γ-rays are emitted from yet another process akin to inelastic scattering. This process is known as Coulomb excitation wherein the excitation of a nucleus occurs through the electromagnetic interaction between the colliding particles. Since the nuclear reactions are not involved, the process can occur at energies lower than the coulomb barrier. The cross-section of the coulomb excitation depends on several features that include: the energy of the incident particle, energy, spin and parity of the excited nuclear state and the extent of the coulomb interaction. The last is defined by the Sommerfield number

$$\xi = \frac{z_p z_t e^2}{\hbar v} \qquad (1.12)$$

where z_p,z_t are the atomic numbers of the incident particle and target respectively. $\hbar$ is the Planck's constant (h/2π) and v is the velocity of the bombarding particle. As pointed out in reference **[75]** Coulomb excitation has good applicability for $\xi \geq 4$. This equation also suggests that the process is more probable for targets with higher atomic numbers and heavier bombarding particles. Some examples of nuclear reactions involving Coulomb excitation are given in **Table 1.4.** The characteristic γ-rays emitted from nuclear reactions are also given.

Table 1.4: *Nuclear reactions and their E_γ involving Coulombic excitation*

S.No	Nuclear reaction	γ-ray energy
1	^{48}Ti(p,γ)^{49}V	981keV
2	^{55}Mn(p,γ)^{56}Fe	126 keV
3	^{56}Fe(p,γ)^{57}Co	847keV
4	^{197}Au(p,γ)^{198}Hg	279keV

(d) Radiative capture

Radiative capture can be defined as the process in which the projectile is captured by the target to form a nucleus 'c' in the excited state that subsequently de-excites to the ground state with the emission of γ-rays. The process can be stated as follows

$$a + A \rightarrow c^* \rightarrow c + \gamma \qquad (1.13)$$

The radiative capture reactions are more intense for light nuclei, mostly for the elements with 3<z<9. It has been observed that for these light nuclei, the energy of capture γ-rays depends on the energy of the particle according to the formula

$$E_\gamma = Q + \frac{(E_p M_A)}{(m_a + M_A)} \qquad (1.14)$$

In view of the dependence of E_γ on the particle energy, it has been occasionally suggested that capture reactions might be used for the energy calibration of the accelerator.

(e) Re-arrangement reactions

Re-arrangement reactions can be defined as those reactions wherein the product or residual nucleus is different from the target nucleus. The product nuclei can be formed in ground state or in excited state. The nuclei formed in excited states de-excite to the ground state with the emission of γ-rays. The examples of such reactions are

$$^{11}B + p \rightarrow {}^{8}Be + \alpha\ ;\ {}^{8}Be \rightarrow 2\alpha \qquad (1.15)$$

$$^{13}C + p \rightarrow {}^{13}N + n \qquad (1.16)$$

$$^{14}N + d \rightarrow {}^{12}C + \alpha + 13.575\ \text{MeV} \qquad (1.17)$$

$$^{19}F + p \rightarrow {}^{16}O^* + \alpha\ ;\ {}^{16}O^* \rightarrow {}^{16}O + \gamma\ (6.1,\ 6.9\ \text{and}\ 7.1\ \text{MeV}) \qquad (1.18)$$

$$^{14}N + d \rightarrow {}^{12}C^* + \alpha + 9.142\ \text{MeV}\ ;\ {}^{12}C^* \rightarrow {}^{12}C + \gamma\ (4.433\text{MeV}) \qquad (1.19)$$

1.5.3 Classification of ion beam analytical techniques

The interactions or processes induced by an incident beam that give rise to different ion beam techniques are pictorially presented in **Fig.1.8** while the classification of the ion beam techniques (based on these processes) are briefly presented in **Table 1.5**. Some of the ion beam techniques are described in detail in the following sections

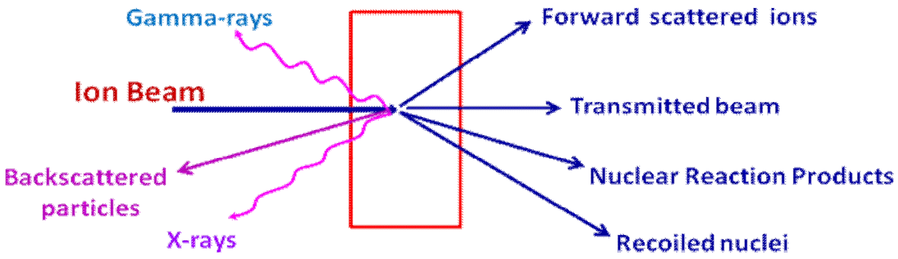

***Fig 1.8:** Schematic of interaction of ion beam with material*

***Table 1.5:** Processes and classification of ion beam analysis*

Method	Acronym	Interaction/Process
Particle- Induced γ-ray Emission	PIGE	Prompt γ-ray emission on irradiation
Particle –Induced X-ray Emission	PIXE	Emission of characteristic x-rays on irradiation
Rutherford Backscattering Spectrometry	RBS	Elastic scattering of incident particles at backward angles
Elastic (Nuclear) Backscattering Spectrometry	EBS	Elastic (non - Rutherford) scattering of incident particles at backward angles
Particle Elastic Scattering Analysis	PESA	Elastic scattering of incident particles at forward angles
Nuclear Reaction Analysis	NRA	Nuclear reaction induced by the incident beam in the target nuclei
Elastic Recoil Detection Analysis	ERDA	Elastic recoil of target nuclei at forward angles

1.6 Nuclear reaction analysis (NRA)

NRA, as the name suggests, utilises a nuclear reaction, preferably with a high Q-value and involves *prompt* measurement of one of the reaction products, and can be schematically represented as **Fig 1.6**. The projectiles often used are protons, deuterons, α-particles or such heavy ions as ^{15}N, ^{19}F etc. while their energy can range from ~100 keV to several MeV. The reaction products can be a charged particle, γ-rays or both as in [^{11}B(p,α)2α], [^{27}Al(p,γ)^{28}Si] and [^{1}H(^{19}F,αγ)^{16}O] respectively **[77,78]**. Nuclear reactions entailing the detection of charged particles are often referred to as “particle-particle” NRA while those involving the detection of γ-rays are classified as “particle-γ ray” NRA. In recent years, the term NRA is exclusively used to represent the former category while PIGE, to the latter. NRA is isotope specific and usually enables its interference free determination. The detection sensitivity of NRA varies from percentage to trace levels. Sensitivity to light elements and non-destructive depth profiling capability are the two most attractive features of NRA which make it a powerful surface technique, particularly in the area of thin film technology **[79]**.

***Table 1.6**: Some of nuclear reactions and their Q-values used in NRA*

Proton induced reactions	Q [MeV]	Deuteron induced reactions	Q [MeV]	^{3}He induced reactions	Q [MeV]	^{4}He induced reactions	Q [MeV]
^{6}Li(p,α)^{3}He	4.02	^{2}H(d,p)^{3}He	4.03	^{2}H(^{3}He,p)^{4}He	18.3	^{10}B(α,p)^{13}C	4.06
^{7}Li(p, α)^{4}He	17.35	^{3}He(d, α)^{1}H	18.3	^{6}Li(^{3}He,p)^{8}Be	6.79	^{11}B(α,p)^{14}C	10.78
^{9}Be(p, γ)^{10}B	6.58	^{12}C(d,p)^{13}C	2.72	^{9}Be(^{3}He,p)^{11}B	10.32	^{14}N(α,p)^{17}O	-1.19
^{11}B(p, α)2α	8.58	^{13}C(d,p)^{14}C	5.95	^{9}Be(^{3}He,α)^{8}Be	18.9	^{19}F(α,p)^{22}Ne	1.67
^{15}N(p, αγ)^{12}C	4.97	^{14}N(d,p)^{15}N	8.61	^{12}C(^{3}He,p)^{14}N	4.78	^{31}P(α,p)^{34}S	0.63
^{18}O(p, αγ)^{15}N	3.98	^{14}N(d, α)^{12}C	13.57	^{12}C(^{3}He, α)^{11}C	1.86		
^{19}F(p,αγ)^{16}O	8.11	^{16}O(d,p)^{17}O	1.92	^{18}O(^{3}He,p)^{20}F	6.87		
^{23}Na(p, αγ)^{24}Mg	11.7	^{16}O(d, α)^{14}N	3.11	^{18}O(^{3}He,d)^{19}F	2.50		
^{27}Al(p, γ)^{28}Si	11.6	^{19}F(d, α)^{17}O	10.03	^{18}O(^{3}He,α)^{19}O	12.51		

The nuclear reactions have a finite probability of occurrence which is denoted by reaction cross-section and is expressed in terms of barns (1 barn = 10^{-24} cm^{2}). A plot of the incident particle energy vs the cross-section of the reaction is termed as the excitation function of the reaction. The excitation function can have elevations and or dips. It can also exhibit resonance, sharp or broad, at specific projectile energies. Such reactions are very useful for depth profiling applications. The related NRA is often referred to as nuclear resonance reaction analysis (NRRA). The resonances should be strong, narrow and isolated for sensitive and high depth resolved measurements. The widths of the resonances may range from 50 eV to several keV. Depth profiling using resonances having widths ≤ 500 eV is known as narrow resonance profiling (NRP) **[80]**. It is instructive to mention that depth profile measurements can be accomplished by non-resonant reactions as well. Incidentally, it is true only for reactions involving particle-particle interactions. List of nuclear reactions generally utilized for analytical purposes are given in **Table 1.6**.

1.7 Particle induced γ-ray emission (PIGE)

Fig 1.9 is a simple graphical illustration of the processes and energetics involved in a nuclear reaction relevant to PIGE. The residual nucleus, B, has, in addition to the ground state, several excited states. These states correspond to set of energy levels unique to the residual nucleus. Following the emission of the particle, the residual nucleus can be formed in the ground state or in an excited state. If the nucleus is left in an excited state, i, following the emission of the particle, it de-excites almost instantaneously (within picoseconds) to its ground state by the emission of γ-rays. These γ-rays have specific energies and are characteristic of the residual nucleus and, in turn, of the target nucleus. In other words, the elements constituting a sample can be identified by their characteristic γ-rays **[68]**.

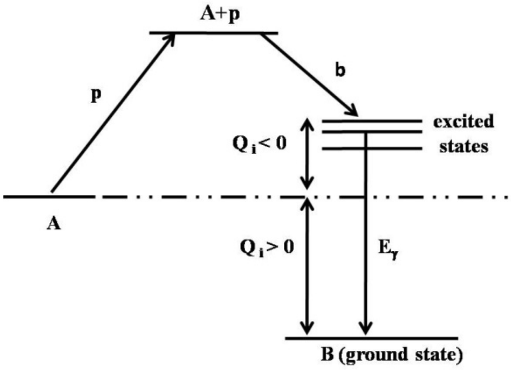

***Fig 1.9:** Schematic of the processes and energetics involved in a nuclear reaction*

It is instructive to mention that the energy of the emitted particles is also characteristic of the nuclear reaction and can provide information of the element(s) present in a sample. The energy of the particles, however, depends on reaction parameters including its

Q value and the angle of the emission. The energy analysis of emitted particles, as mentioned earlier, pertains to NRA and an account of the energetic involved in NRA is presented in **Chapter 3** wherein ^{7}Li(p,α)α nuclear reaction has been employed for the detection and depth profiling of Li in materials.

This is in sharp contrast to activation analysis, another nuclear reaction based analytical technique in which the product is radioactive in nature and emits γ-rays according to its half life. Importantly, activation analysis performed with charged particles and neutrons as projectiles with the techniques referred to as charged particle activation analysis (CPAA) and neutrons activation analysis (NAA) respectively.

In the background of the above discussion, PIGE can be described as the ion beam technique, based on the measurement of prompt γ-rays emitted as a result of such nuclear reactions as inelastic scattering (p,p'γ), proton capture (p,γ), Coulomb excitation (p,γ) or a re-arrangement reaction **[68]**. These reactions are pictorially represented in **Fig 1.10, 1.11 and 1.12**. The prompt γ-rays are often measured with high energy resolution using semiconductor detectors, though scintillator detectors are also used in specific cases. The irradiation with an energetic beam can induce nuclear reactions simultaneously in one or several elements constituting target, causing the emission of their respective characteristic γ-rays in the process. High energy resolution γ-ray spectrometry, therefore makes this a (simultaneous) multi-elemental technique. The technique is more suitable to lighter than heavy nuclei due to Coulomb barrier. Some of the light elements regularly analysed using PIGE are Li, B, F, Na, Mg, Al, Si, P, S, Cl while mid and high z elements amenable to PIGE, though with reduced sensitivity, include Ti, Mn, Fe, As, Au etc. The nuclear reactions involving some of these elements and their characteristics γ-rays are listed in **Table 1.7 and 1.8** for illustrations and referencing. It is to be noted that at times the assignment of the prompt γ-rays is based, instead of nuclear reactions, by notations approved at Analyst's Convention which are as follows **[68]**.

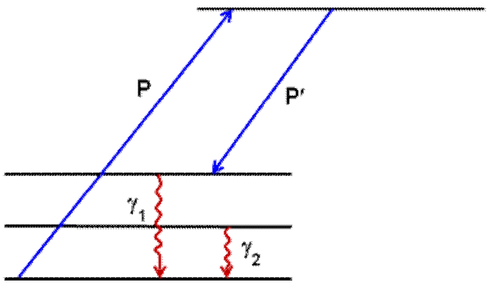

Fig 1.10*: Schematic of (p, p′γ) reaction mechanism*

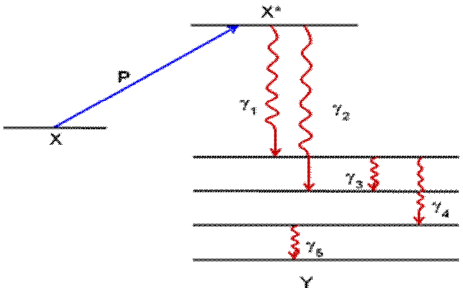

Fig 1.11*: Schematic of (p,γ) reaction mechanism*

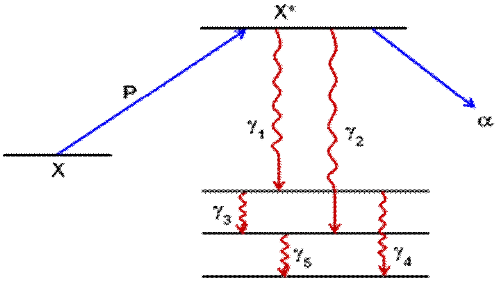

Fig 1.12*: Schematic of (p,αγ) reaction mechanism*

1.7.1 Nomenclature of prompt γ-rays:

Analyst's convention for γ-ray assignment in PIGE:

1. In the nuclear reaction A(a,b)B, the γ-ray is written as A b(r,s) where b is the prompt light product of the reaction and the γ-ray is emitted from the de-excitation of the heavy product (B) from level r to level s.
2. If particle b is the same as particle a, as for example in Coulomb excitation, it may be omitted.
3. When the target nucleus may be inferred unambiguously from the context, it may be omitted.
4. When a prompt γ-ray arises from a reaction not directly induced by the bombarding particle, both incident and product particles are specified.

Fig 1.13 illustrates the convention for γ-ray assignment of ^{19}F p (3,1) nuclear reaction

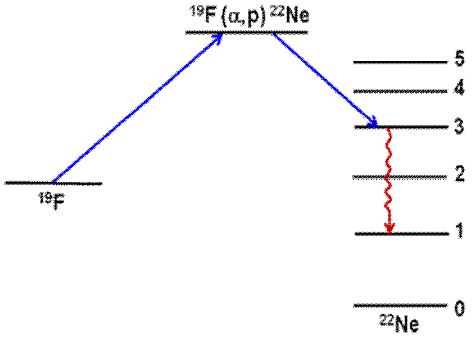

***Fig 1.13**: Schematic of ^{19}F   p (3,1) nuclear reaction*

***Table 1.7:** Nuclear reactions involving low z elements and their characteristic E$_{\gamma}$*

Element/ Nuclear reaction	**E$_{\gamma}$ (keV)**	**Nuclear reaction**	**E$_{\gamma}$ (keV)**	**Nuclear reaction**	**E$_{\gamma}$ (keV)**
Li		^{19}F(p,p′γ)^{19}F	1357	^{28}Si (p,p′γ)^{28}Si	3200
^{7}Li(p,p′γ)^{7}Li	478	^{19}F(p, αγ)^{16}O	6129	**P**	
^{7}Li(p,nγ)^{7}Be	429	**Na**		^{31}P(p,p′γ)^{31}P	1266
^{6}Li(p, γ)^{7}Be	429	^{23}Na(p,p′γ)^{23}Na	440	^{31}P(p,αγ)^{28}Si	1779
Be		^{23}Na(p,p′γ)^{24}Mg	1636	^{31}P(p, γ)^{32}S	2234
^{7}Be(p, αγ)^{6}Li	3562	^{23}Na(p,p′γ)^{23}Na	1951	^{31}P(p,p′γ)^{31}P	2230
^{9}Be(p, γ)^{10}B	718	^{23}Na(p,p′γ)^{23}Na	2391	**S**	
B		**Mg**		^{32}S(p,p′γ)^{32}S	841
^{10}B(p, αγ)^{7}Be	429	^{24}Mg(p,p′γ)^{24}Mg	417	^{34}S(p, γ)^{35}Cl	1219
^{10}B(p,p′γ)^{10}B	718	^{25}Mg(p,p′γ)^{25}Mg	585	^{34}S(p,p′γ)^{34}S	2127
^{11}B(p,p′γ)^{11}B	2124	^{25}Mg(p,p′γ)^{25}Mg	975	^{32}S(p,p′γ)^{32}S	2234
C		^{24}Mg(p,p′γ)^{24}Mg	1369	^{32}S(p,p′γ)^{32}S	4282
^{12}C(p,p′γ)^{12}C	4439	^{24}Mg(p,p′γ)^{24}Mg	2754	**Cl**	
^{13}C(p,p′γ)^{13}C	3089	^{24}Mg(p,p′γ)^{24}Mg	4239	^{35}Cl(p,p′γ)^{35}Cl	1219
N		**Al**		^{35}Cl(p,nγ)^{35}Ar	1410
^{14}N(p,p′γ)^{14}N	1635	^{27}Al(p,p′γ)^{27}Al	844	^{35}Cl(p,p′γ)^{35}Cl	1763
^{14}N(p,p′γ)^{14}N	2313	^{27}Al(p,p′γ)^{27}Al	1014	^{35}Cl(p,αγ)^{31}P	2230
^{14}N(p,p′γ)^{14}N	5106	^{27}Al(p,p′γ)^{27}Al	2210	^{35}Cl(p,p′γ)^{35}Cl	3163
O		^{27}Al(p,p′γ)^{27}Al	2734	**K**	
^{16}O(p, γ)^{17}F	495	^{27}Al(p,p′γ)^{27}Al	2981	^{39}K(p, γ)^{40}Ca	2168
^{17}O(p,p′γ)^{17}O	871	^{27}Al(p,p′γ)^{27}Al	3004	^{39}K(p,p′γ)^{39}K	2814
^{18}O(p,p′γ)^{18}O	1982	**Si**		^{39}K(p,p′γ)^{39}K	3019
^{16}O(p,p′γ)^{16}O	6129	^{29}Si (p,p′γ)^{29}Si	755	^{39}K(p,p′γ)^{39}K	3598
^{16}O(p,p′γ)^{16}O	6919	^{30}Si(p, γ)^{31}P	1266	^{41}K(p,p′γ)^{41}K	1294
^{16}O(p,p′γ)^{16}O	7114	^{29}Si (p, γ)^{30}Si	1273	**Ca**	
F		^{29}Si (p,p′γ)^{29}Si	1779	^{40}Ca(p,p′γ)^{40}Ca	755
^{19}F(p,p′γ)^{19}F	110	^{28}Si (p,p′γ)^{28}Si	2028	^{40}Ca(p,p′γ)^{40}Ca	3736
^{19}F(p,p′γ)^{19}F	197	^{29}Si (p,p′γ)^{29}Si	2230	^{40}Ca(p,p′γ)^{40}Ca	3904
^{19}F(p,p′γ)^{19}F	1236	^{29}Si (p, γ)^{30}P	2235		
^{19}F(p,p′γ)^{19}F	1346	^{30}Si (p,p′γ)^{30}Si	2839		

Table 1.8: *Nuclear reactions involving mid and high z elements and their characteristic E_γ*

Nuclear reaction	E_γ (keV)	Nuclear reaction	E_γ (keV)	Nuclear reaction	E_γ (keV)
Ti		**Ni**		**Zr**	
^{48}Ti(p,p′γ)^{48}Ti	981	^{58}Ni(p,p′γ)^{58}Ni	1412	^{91}Zr(p,γ)^{91}Nb	1082
^{48}Ti(p,p′γ)^{48}Ti	1312	^{60}Ni(p,p′γ)^{60}Ni	1333	**Mo**	
^{48}Ti(p,p′γ)^{48}Ti	1437	**Cu**		^{95}Mo(p,p′γ)^{95}Mo	204
Cr		^{63}Cu(p,p′γ)^{63}Cu	962	**Ag**	
^{52}Cr(p,p′γ)^{52}Cr	1434	^{63}Cu(p,p′γ)^{63}Cu	1327	^{109}Ag(p,p′γ)^{109}Ag	311
^{52}Cr(p,nγ)^{52}Mn	377.5	**Zn**		**Ba**	
Mn		^{64}Zn(p,p′γ)^{64}Zn	992	^{137}Ba(p,p′γ)^{137}Ba	279
^{55}Mn(p,p′γ)^{55}Mn	126	**As**		**Hf**	
^{55}Mn(p,nγ)^{55}Fe	412	^{75}As(p,nγ)^{75}Se	287	^{178}Hf(p,p′γ)^{178}Hf	93
^{55}Mn(p,nγ)^{55}Fe	931	**Se**		**W**	
Fe		^{78}Se(p,p′γ)^{78}Se	613.6	^{184}W(p,p′γ)^{184}W	110
^{56}Fe(p,p′γ)^{56}Fe	846.6	**Se**		**Au**	
Co		^{87}Sr(p,nγ)^{87}Y	232	^{197}Au(p,p′γ)^{197}Au	279
^{59}Co(p,nγ)^{59}Ni	339	**Y**			
^{59}Co(p,p′γ)^{59}Co	1432	^{89}Y(p, p′γ)^{89}Y	2186		

Apart from protons, nuclear reactions induced by other ions can also emit prompt γ-rays. Some of reactions emitting γ-rays, induced by deuterons, tritons, α-particles and heavy ions are given in **Table 1.9.**

Table 1.9*: Some of nuclear reactions and their E_γ induced by deuterons, tritons, α particles and heavy ions*

Deuteron induced reactions	E_γ [keV]	Triton induced reactions	E_γ [keV]	^{3}He / ^{4}He induced reactions	E_γ [keV]	^{35}Cl induced reactions	E_γ [keV]
^{12}C(d,pγ)^{13}C	2070	^{7}Li(t,t′γ)^{7}Li	478	^{11}B(^{3}He,αγ)^{10}B	718	^{177}Hf(^{35}Cl, ^{35}Cl γ)^{177}Hf	123
^{12}C(d,pγ)^{13}C	3090	^{19}F(t,pγ)^{18}O	1982	^{11}B(^{3}He,αγ)^{10}B	1022	^{232}Th(^{35}Cl, ^{35}Cl γ)^{232}Th	113
^{14}N(d,pγ)^{15}N	5300	^{19}F(t,t′γ)^{19}F	110	^{18}O(α,nγ)^{21}Ne	351		
^{14}N(d,nγ)^{15}O	6820	^{23}Na(t,αγ)^{22}Ne	1275	^{23}Na(α,pγ)^{26}Mg	1809		
^{14}N(d,nγ)^{15}O	7300	^{28}Si(t,αγ)^{23}Na	440	^{48}Ti(α,nγ)^{51}Cr	749		
^{14}N(d,nγ)^{15}O	8300	^{28}Si(t,nγ)^{30}P	677	^{48}Ti(α,αγ)^{48}Ti	983		
^{16}O(d,pγ)^{17}O	8710	^{182}W(t,t′γ)^{182}W	100	^{56}Fe(α,αγ)^{56}Fe	847		

1.7.2 Thick target yield

PIGE is utilised for qualitative and quantitative analysis. The technique usually provides the bulk concentration of the elements in materials and is more applicable for thick target. The incident beam loses its complete energy in a thick target and comes to rest at a distance corresponding to its range in that material. The beam during its propagation induces (allowed) nuclear reactions, emitting prompt γ-rays. The measurement of these γ-rays are known as thick target γ-ray yield which is specific for a nuclear reaction and the angle of emission and often quoted after normalisation for charge and solid angle. The thick target yields are measured using targets of known composition. The thick target γ-ray yields has been measured by several researchers, amongst which those reported by Kiss et. al., for a number of low z elements in mid 80's for 2.4 – 4.2 MeV protons and more recently, by Savidou et.al are particularly noteworthy. Thick target yields define the sensitivity of an element under different experimental conditions, facilitate the identification of interferences if any and enable their determination. The detection sensitivity of PIGE varies from isotope to isotope and it ranges from 10 – 1000 ppm for most of the low Z elements. An examination of thick target yields in references **[81,82]** suggests that Li, B, F, Na and Al have the highest detection sensitivity. Also, PIGE can be used for isotopic analysis of ^{10}B and ^{11}B; ^{12}C and ^{13}C;^{14}N and ^{15}N; ^{16}O,^{17}O and^{18}O; ^{28}Si, ^{29}Si and ^{30}Si **[83]**. Notably, the targets are considered to be uniform and at about 4 MeV proton beam energy, it gives the average yield over a depth of several tens of microns in most of the cases. PIGE can also be utilised for the analysis of thin films with reactions exhibiting narrow resonances being more suitable **[84]**. Importantly, the narrow resonances are also used for depth profiling purposes with very good credentials.

The thick target yield (Y) of γ-rays **[76, 85]** can be obtained from the following equation

$$Y_i = N_0 \, f \, I \, \Omega \, \varepsilon \, C_i \int_{E_0}^{0} \frac{\sigma_i(E)dE}{S(E)} \qquad (1.20)$$

wherein, N_0 represents the Avogadro's number; f, natural isoto abundance of element (i); I, the number of incident particles; Ω, the solid angle; ε, the efficiency of the detector; σ (E), the cross-section of the reaction as a function of beam energy; S(E), the stopping power and C_i is the concentration of the element i.

It is important to note that the geometry of γ-ray detection or the geometric arrangement of the γ-ray detector and the total charge are defined by γ-ray emission properties of the nuclei formed. It is well known that the excited states of the nuclei produced in the nuclear reactions have an oriented angular distribution, which depends on the type of the nuclear reaction and also on the multi-polarities of the emitted γ-rays. To minimise the contribution of the angular distribution in the quantitative analysis, the γ-ray detector is traditionally placed at either 55° or 125° with respect to the beam direction **[86]**.

The **equation 1.20** represents the fundamental relationship between the intensity of the emitted γ-rays and the concentration of a target nuclei in a specimen. **Equation 1.20** is also termed as fundamental equation for determining the concentration of an element / isotope in a specimen. Evidently this requires knowledge of a number of parameters such as reaction cross-section as a function of energy, efficiency of detector solid angle etc. which are often difficult to determine with good accuracy. As a result, the determination of the concentration by using the fundamental equation is not considered to be an optimum approach. As a result to circumvent the problems encountered in this method, comparator methods are utilised. In comparator method, a material preferably of known composition equivalent to the composition of the target (known as standard) is irradiated and counted under identical experimental conditions. As a result, the **equation 1.20** can be written as

$$\frac{C_i}{C_R}=\left(\frac{Y_i}{Y_R}\right)\times\frac{S_R(E)}{S_i(E)} \qquad (1.21)$$

where $S_R(E)$ and $S_i(E)$ are stopping powers of standard and sample respectively at an energy of $E_0/2$ **[87]**.

1.8 Rutherford backscattering spectrometry (RBS)

RBS has evolved as one of the most important ion beam analysis techniques for the analysis of thin films in terms of their composition, thickness and defects. It is based on the energy analysis of charged particles scattered in the backward directions following their interaction with the nuclei.

The schematic of a typical backscattering event that forms the basis of the technique is shown in the **Fig 1.14.** Experimentally an energetic ion beam of mass M_1 obtained from an accelerator impinges on an atom of mass M_2 and gets backscatter through an angle θ with respect to its incident direction. The backscattered particles are detected using a particle detector of energy resolution of about 10-15 keV. It is to be noted that for a backscattering event to take place $M_1<M_2$ **[65,88]**.

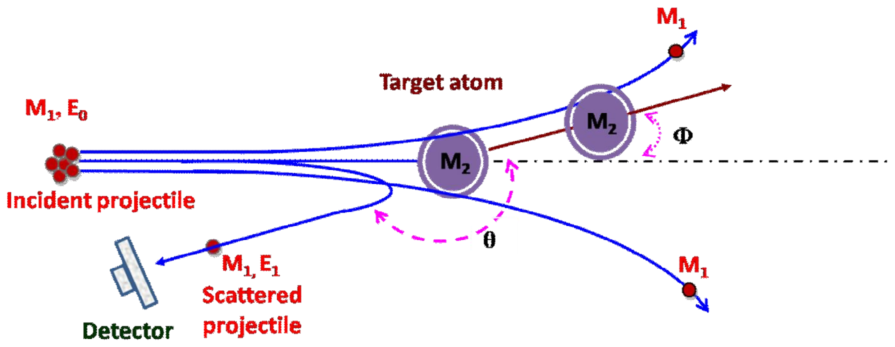

***Fig 1.14**: Schematic of Rutherford backscattering spectrometry*

RBS is based on three basic concepts, namely, kinematics, scattering cross-section and energy loss (stopping power). The later one has been described in **Chapter 2, Section**

2.4. So far as the collision kinematics is concerned, it is related to the energy transfer from the projectile to the target atom. The collision is elastic in nature and gives rise to the concept of kinematic factor ‘K’ which is defined by the equation

$$K = \frac{E}{E_0} \qquad (1.22)$$

$$K = \left[\frac{\left(M_2^2 - M_1^2 \sin^2\theta\right)^{1/2} + M_1 \cos\theta}{M_1 + M_2} \right]^2 \qquad (1.23)$$

$$K = \left\{ \frac{\left[1-(M_1/M_2)^2 \sin^2\theta\right]^{1/2} + (M_1/M_2)\cos\theta}{1+(M_1/M_2)} \right\} \qquad (1.24)$$

The kinematic factor facilitates the identification of elements present in a sample through mass analysis. The mass resolution is higher at backward angles, stated explicitly, the mass resolution increases with increasing the backscattering angle, increase in the energy and also mass of the projectile. The mass resolution is higher in low mass (energy) regions of the target and is low in high mass (energy) regions (**Fig 1.15**). Variation of kinematic factors for ^{1}H and ^{4}He projectiles as a function of scattering angle, for different M_2 are given in **Table 1.10**. Backscattering cross-section is an another concept of RBS. It facilitates the quantification of the elements comprising a target. The scattering cross-section is given by

$$\frac{d\sigma}{d\Omega} = \left(\frac{Z_1 Z_2 e^2}{4E} \right)^2 \frac{4}{\sin^4\theta} \frac{\left\{ \left[1-((M_1/M_2)\sin\theta)^2\right]^{1/2} + \cos\theta \right\}^2}{\left[1-((M_1/M_2)\sin\theta)^2\right]^{1/2}} \qquad (1.25)$$

This equation reveals that the Rutherford differential cross-section is larger for heavier projectiles and also for heavier targets, while it decreases with the increase in energy and the backscattering angle. In other words, RBS is more sensitive to heavy elements and is less sensitive to light elements. Incidentally, as stated earlier, better mass discrimination is possible for low z elements, while it is poorer for high z elements. However, it has been observed that for several low z elements, in the energy region 1-10 MeV, the cross-section is not Rutherford. For some elements or isotopes the excitation functions consists of resonances at which the scattering cross-section is several times higher than the corresponding backscattering cross-sections. Such resonances in the backscattering events are very useful for the determination of light elements with good sensitivity **[88]**.

Rutherford backscattering experiments are performed in vacuum and is highly applicable to the thin films and materials in the surface and near surface regions. Apart from identification and quantification of elements, RBS is also useful for depth profiling with a typical depth resolution of 200Å (20nm). The depth resolution can be improved at glancing incident angle. This concept of RBS has been utilised extensively in diffusion studies.

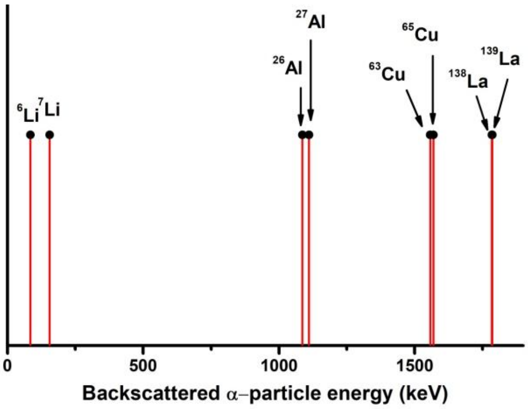

***Fig 1.15**: Discrimination of masses in RBS using 2 MeV α-particles*

***Table 1.10:** Kinematic factors K_{M_2} for ^{1}H and ^{4}He as projectiles for different M_2 at different scattering angles*

Atomic mass M_2 (amu)	Scattering angle				
	180°	170°	150°	120°	90°
	Kinematic factors K_{M_2} for ^{1}H as projectile				
10	0.6673	0.6740	0.6856	0.7382	0.8169
30	0.8742	0.8751	0.8821	0.9041	0.9350
50	0.9225	0.9231	0.9275	0.9413	0.9605
70	0.9440	0.9444	0.9477	0.9577	0.9716
90	0.9562	0.9565	0.9591	0.9670	0.9779
	Kinematic factors K_{M_2} for ^{4}He as projectile				
10	0.1834	0.1857	0.2044	0.2777	0.4283
30	0.5846	0.5869	0.6059	0.6683	0.7646
50	0.7255	0.7273	0.7412	0.7860	0.8518
70	0.7954	0.7967	0.8076	0.8422	0.8918
90	0.8369	0.8381	0.8470	0.8750	0.9148

1.9 Elastic Recoil Detection Analysis (ERDA)

ERDA is a complementary to Rutherford backscattering spectrometry and is well suited for the detection and depth profile measurements of low z elements in the surface regions of the materials. Herein, a beam of ions is incident on the sample surface at low angles and the atom or ions of the target (recoiled) are detected in the forward direction **[65,68]**. Evidently, the particle detector is positioned at a forward angle and a foil of suitable thickness is interspersed between the target and the detector to prevent the entry of the scattered projectiles into the detector. Like the case with the RBS, the kinematic factor and differential cross-section are two important concepts of ERDA. The kinematic factor (K_R) for the elastic recoil derived from the laws of conservation of energy and momentum is given by the relationship

$$E_2 = K_R E_1 \qquad (1.26)$$

$$K_R = \frac{4M_1 M_2}{(M_1 + M_2)^2} \cos^2\theta \qquad (1.27)$$

where M_1 and M_2 are the mass of projectile and mass of target atom. θ is the angle of recoil. Therefore, the energy of hydrogen recoils emitted from the top surface of hydrogen bearing material bombarded with 4 MeV α and 12 MeV carbon beam at a recoil angle of 30° is 1928 keV and 2573 keV respectively.

The recoil cross-section is given by the relation

$$\sigma_R = 5.18\times10^{-27}\left(\frac{Z_1 Z_2\,(M_1 + M_2)}{M_2 E_1}\right)^2 \frac{1}{\cos^3\theta} \qquad (1.28)$$

where Z_1,Z_2 are the atomic numbers of projectile and target atoms.

The detection sensitivity of ERDA for different elements varies in 0.1 to 1 at.%, where as depth resolution is ~ 1000Å. In Rutherford backscattering spectrometry, the mass for the projectile should be less than the mass of the analyte atoms. Where as in ERDA the mass of the projectile should be more than the mass of the analyte atoms.

ERDA like another ion beam technique is a non-destructive in nature and has immense value in the analysis of materials, thin films in particular. One of the important applications of ERDA is to determine the ‘H’ in materials, notably the three isotopes of hydrogen can be identified and differentiated. A typical experimental set up involved in ERDA is shown in **Fig 1.16**.

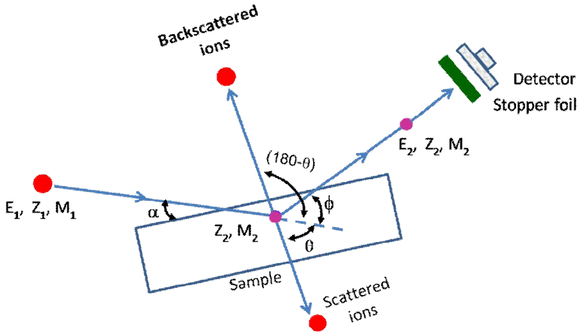

***Fig 1.16**: An experimental set up involved in ERDA*

1.10 Particle induced X-ray emission (PIXE)

PIXE is one of the most important ion beam analysis techniques and is widely used for the determination of major, minor and trace elements in thin films and bulk materials. As the name suggests, the technique is based on the energy analysis of characteristic x-rays from a sample following its bombardment with an energetic charged particle, usually proton **[68, 89]**. Thus this method is analogue to XRF except that the two techniques have different probes. Schematic diagrams representing the process involved in PIXE are shown in **Fig 1.17** and **Fig 1.18** for illustration.

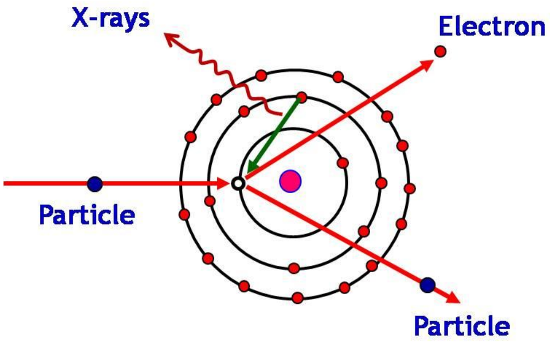

***Fig 1.17**: Schematic of X-ray production in PIXE*

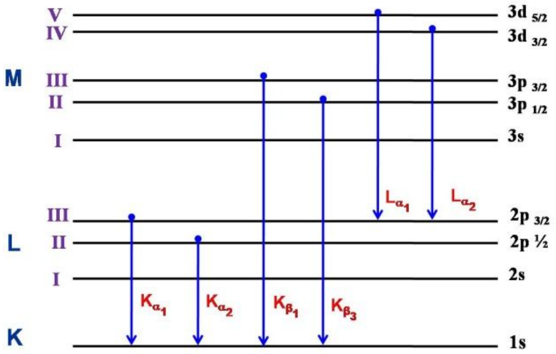

***Fig 1.18:** Energy level diagram showing the origin of K and L X-rays*

PIXE is a simultaneous multi-element technique that provides qualitative and quantitative analysis of materials non-destructively. In terms of nature of elements, those with $z \geq 11$ can be determined with good detection sensitivity. However, quantification by this method is an involved process and simulation codes such as GUPIX is often employed for the quantitative analysis. The quantification of elements in thin targets wherein the energy loss of the beam and also the attenuation of the produced x-rays are insignificant, however, the preparation of such targets is significantly difficult. However, in the case of thick target, the preparation of targets is simpler, but the quantification is difficult. The difficulty in quantification arises due to matrix effects which are the embodiments of significant energy loss of proton beam and attenuation of x-rays in materials. As a result, several approaches have been reported in the literature for quantification of thick targets by taking into consideration of matrix effects.

As stated earlier, PIXE to a large extent resembles XRF. However, there are some distinct dissimilarities between the two techniques **[65]**. A comparison of the features of PIXE and XRF are given in **Table 1.11** for better clarity. Similarly, a comparison of different parameters involved in the analysis of samples by SIMS, GDMS, XPS and IBA are given in **Table 1.12**.

***Table 1.11**: Comparison of features of PIXE and XRF*

	PIXE	XRF
Probe	Charged particles (p : 1- 2.5 MeV)	Characteristic X-rays (Mo K_α= 17.6 keV)
Elements	Z >11	Z >11
Probing depth	20 - 30 µm	> 100 µm
Background	High in low energy region Low in high energy region	Low in low energy region High in high energy region
	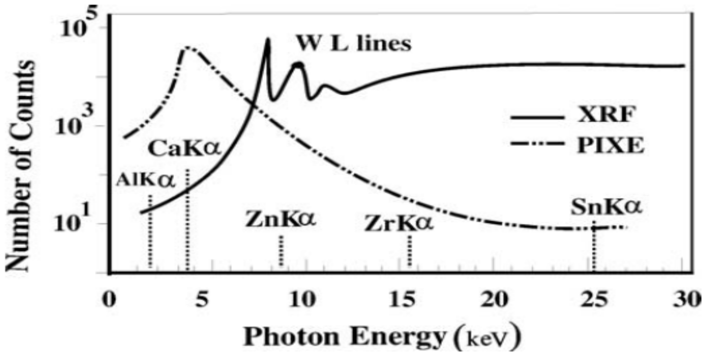	
Limit of detection	Thin targets Low Z matrix: 0.1-100 ppm	Thin targets Low Z matrix: 10-100ppm
	Thick targets Low Z matrix: 10-100ppm	Thick targets Low Z matrix: 10-100ppm

***Table 1.12:** Comparison of features of SIMS, GDMS, XPS and IBA*

	XPS	GD-MS	SIMS	IBA
Primary beam	X-rays	Plasma	keV ions	0.1 – 5 MeV ions
Detected signal	Photo-electrons	Ions	Sputtered ions	Nuclear reaction products; scattered primaries; target recoils; X-rays; γ-rays
Destructive	Yes	Yes	Yes	No
Depth resolution	2 nm	100 nm	2 nm	2 nm
Probing depth	500 nm	300 nm	500 nm	15 µm
Lateral resolution	3 µm	2 mm	50 nm	500 nm
Elemental imaging	No	Yes	Yes	Yes
Molecular information	Yes	No	Yes	No
Ambient analysis	No	Yes	No	Yes
Sample preparation	UHV	No	No	No
Quantitative	Yes	Yes	-	Yes
Standards needed	Yes	Yes	Yes	No
Elemental sensitivity	10^{-3}	10^{-9}	10^{-8}	10^{-6}
Accuracy	5%	10%	10%	1%
Traceability	-	Yes	-	Yes Primary

1.11 Neutron depth profiling (NDP)

NDP is a nuclear analytical technique that utilizes thermal neutrons (0.025eV) obtained from a nuclear reactor. NDP like any other nuclear analytical technique, is isotope specific and involves the detection / measurement of one of the products formed as a consequence of nuclear reaction induced by the incident neutron beam. The products are invariably charged particles which are detected by a silicon surface barrier or by PIPS detector. The charged particles travel from the place of birth to the detector loosing energy in the process in the material. The loss of energy of the charged particle is defined by stopping power which has been described extensively in **Chapter 2, Section 2.4**. NDP is sensitive to low z elements, including Li and has been utilized extensively for their determination and depth profile in materials **[90,91]**. The probing depth is usually higher than realized by ion beam analysis techniques. Some of the reactions used for the determination of elements by NDP and their salient features are described in **Table 1.13.**

***Table 1.13**: Characteristics of reactions used in the neutron depth profiling*

Element	Reaction	Q (MeV)	%Abundance	Energy of emitted particles (keV)		Cross-section (barns)	Detection limit (atoms/cm^2)
He	$^3He(n,p)^3H$	0.764	0.00014	572	191	5333	1.5×10^{12}
Li	$^6Li(n,\alpha)^3H$	4.7821	7.5	2055	2727	940	9.0×10^{12}
B	$^{10}B(n,\alpha)^7Li$	2.7905	19.9	1472	840	3837	2.1×10^{12}
N	$^{14}N(n,p)^{14}C$	0.6259	99.6	584	42	1.83	4.5×10^{15}
O	$^{17}O(n,\alpha)^{14}C$	1.825	0.038	1413	404	0.24	3.5×10^{16}

1.12 Scope of the work

Studies on crystal structure, microstructure, defect chemistry and electrical characteristics of compound semiconductors and energy materials are reported extensively in the literature. However, analytical studies on the elemental composition of these materials are rather limited or scarce. The objective of the present thesis is to develop particle induced gamma ray emission methods using proton beam for the determination of light element constituents of compound semiconductors and energy materials. As these materials find applications in bulk form or as thin films, investigations have been directed to develop methods for the bulk determination or for depth profiling of elements. More explicitly, methods have been developed for the determination of bulk boron, carbon and oxygen while those for depth profiling were standardised for Li and silicon. The former methods are based on the thick target yields of the characteristic gamma rays while the latter employ the resonances in the excitation functions of the relevant reactions. The experiments were conducted with 1-4.2 MeV proton beams obtained from the 3MV Tandetron at NCCCM, Hyderabad and such analytical features as limit of detection, probing depth and depth resolution of methodologies were established. The methods were validated by analysing stoichiometric materials and in certain cases, also by other ion beam methods namely nuclear reaction analysis (NRA) and backscattering spectrometry (BS).

The PIGE methods for the determination of bulk boron and carbon were employed for analysis of powder and also sintered boron carbide specimens in terms of $^{10}B/^{11}B$ ratio and B/C ratio. The method is found suitable particularly to sintered specimens which, due to refractory nature, is not amenable to analysis by wet-chemical methods. Similarly methods based on $^{18}O(p,p'\gamma)^{18}O$ and $^{18}O(p,\alpha\gamma)^{15}N$ reactions were used to determine bulk oxygen in a large number of binary and ternary oxide semiconductors with good statistical attributes. Between the two $^{18}O(p,p'\gamma)^{18}O$ reaction is more suitable for the analysis. The γ-ray spectrum from $^{18}O(p,\alpha\gamma)^{15}N$ reaction is rather complex and the features therein have been investigated and explained.

Comprehensive experiments were conducted for establishing a methodology for depth profiling Li by $^{7}Li(p,\gamma)^{8}Be$ nuclear resonance reaction. Another method based on NRA [reaction: $^{7}Li(p,\alpha)\alpha$] was standardised for the validation of results obtained by the PIGE method. Both methods were utilised for the analysis of cathode and anode materials of lithium ion battery (LIB) and were found to yield identical results. The analysis by PIGE is experimentally time consuming while quantification by NRA is complex in nature. Similarly silicon was depth profiled in several Si_3N_4 and SiC samples by $^{28}Si(p,p'\gamma)^{28}Si$ nuclear resonance reaction.

Chapter 2

Materials and Methodology

2.1 Introduction

This chapter provides a description of (a) the materials and (b) the experimental facilities and parameters/conditions used in the investigations described in the succeeding chapters. In addition, some basic aspects, innate to IBA in general and PIGE and NRA in particular, are also elucidated. The materials examined are essentially solids existing either as powders, discs or as thin films on a substrate. Since IBA is performed in vacuum and involves the bombardment of a target with energetic ion beams, stability in vacuum and also under ion beam irradiation were the two main criteria behind the selection of the materials. Materials possessing these properties are essential for the development of robust IBA methodologies capable of yielding reproducible results.

In accordance with the objectives of the studies, semiconductors and energy materials have been the foci of the investigations. Amongst semiconductors, a large number of binary and ternary oxides that include silicon dioxide (SiO_2), titanium oxide (TiO_2), zinc oxide (ZnO), yttrium oxide (Y_2O_3), lanthanum oxide (La_2O_3), semiconducting barium titanate ($BaTiO_3$) and calcium manganite ($CaMnO_3$) were analysed. In addition to semiconductors, some dielectric materials of barium titanate family namely barium tetratitanate ($BaTi_4O_9$) and barium nonatitanate ($Ba_2Ti_9O_{20}$) were also examined. These materials were either in the form of powders or sintered discs. Single crystals of silicon carbide (SiC) and thin films of silicon nitride (Si_3N_4) on gallium arsenide (GaAs) substrates were the other semiconductors analysed.

So far as the energy materials are concerned, those used in lithium ion batteries (LIB) were prominently analysed. These include graphite that serve as an anode and lithium cobaltate ($LiCoO_2$) and lithium iron phosphate ($LiFePO_4$) are used as cathodes in a LIB. Experiments were also conducted on lithium titanate that serves not only as an anode in a LIB, but is also a candidate material for tritium breeding in ITER **[92]**.

Extensive measurements were also performed on boron carbide. Though the material, similar to $LiCoO_2$ or Li_2TiO_3, is not directly involved in the production of energy, it is of immense significance in nuclear reactors wherein it is used in the manufacture of control rods **[41]** for regulating the nuclear fission for the production of electricity. Importantly, boron carbide displays semiconducting properties as well and is characterised by a band gap of about 2.09 eV **[39]**.

For the characterisation of these materials by PIGE and other ion beam techniques, the 3MV Tandetron at the Surface and Profile Measurement Laboratory, NCCCM, BARC Hyderabad was utilised. The experiments were conducted with proton beams possessing energy in 0.4-4.1 MeV region. The accelerator meets the safety protocols outlined by BARC Safety Council (BARC) and is operated by trained personnel.

2.2 Materials

The binary oxides were procured from E-Merck, sd Fine Chemicals, Qualigens Fine Chemicals or Alfa Aeser. $CaCO_3$ (E-Merck) served as a standard for quantifying oxygen. The minimum assay of each of these chemicals was in 99.5% – 99.9 % range. A known amount of each of these powder materials (usually ~ 300mg) was mixed with about 30mg of high purity graphite in an agate mortar and pestle. To ensure homogeneity the powders were mixed for about 2 hours with continuous addition of doubly distilled acetone. The homogenised powders were dried in a hot air oven at about 60°C and were subsequently compressed using a hydraulic press into pellets that measured 10 – 20 mm in diameter and about 1mm in thickness. These pressed pellets served as targets for their analysis by the IBA techniques.

$BaTiO_3$, $BaTi_4O_9$ and $Ba_2Ti_9O_{20}$ were prepared in the laboratory using wet-chemical methods. $BaTiO_3$ was synthesised by oxalate precursor method while the polytitanates were synthesised by gel to carbonate method. The procedures are described in references **[54,55]** in detail. Briefly, the synthesis of $BaTiO_3$ entailed the preparation of barium titanyle oxalate

(BTO) and its thermal treatment at 800°C in air. The thermal treatment lead to the decomposition of BTO and resulted in the formation of phase pure $BaTiO_3$ powders. The powders were in fact doped with 0.5% Sb (added during the course of precipitation). Doping imparts semiconducting properties to the ceramic, which otherwise is non-conducting (dielectric) in nature. The preparation of barium polytitanates, on the other hand, involved co-precipitation of the gels of hydrated metal oxide ($TiO_2.xH_2O$) and $BaCO_3$ by the addition of ammonium carbonate to a solution containing $TiOCl_2$ and barium chloride ($BaCl_2$) in required molar proportions. The powders of barium titanate and barium poly titanates were pressed into pellets and sintered in air at 1300°C. The sintered discs exhibited good (>97%) phase purity and were coated with a thin layer of carbon for their analysis **[54]**. The other ternary ceramics, namely $CaMnO_3$ and Li_2TiO_3, were in powder form and were procured from BARC. These two compounds were also (96%) phase pure.

The single crystals of SiC were procured from Centre for Materials for Electronics Technology (C-MET), Hyderabad while the thin films of Si_3N_4 on GaAs substrates were procured from Gallium Arsenide Enabling Technology Centre (GAETEC), Hyderabad. The films were prepared by plasma enhanced chemical vapour deposition (PECVD) technique **[93]** and contained, as determined by $^{1}H(^{19}F,\alpha\gamma)^{16}O$ nuclear resonance reaction analysis, about 20-30 at.% hydrogen.

The cathode ($LiCoO_2$ and $LiFePO_4$) and anode (graphite) of LIB were from a commercially available lithium ion battery. Pure (>99%) lithium carbonate (Li_2CO_3) and, Li_2CO_3 and graphite mixed in 50:50 wt. % proportions were used for the preparation of thick targets which were about 20mm in diameter and <1mm in thickness. Thin films of LiF were used extensively in the development of the methodology for depth profiling lithium. The films were deposited on Si and also glass substrates by physical vapour deposition (PVD, resistive heating) using a HIND HIVAC evaporation system (**Fig 2.1**). The deposition involved the heating of LiF powder (~100mg) in a molybdenum boat by passing a current of ~50 amps **[94]**. The depositions were carried out at a vacuum of 10^{-6} torr generated through a combination of rotary and diffusion pumps. The films were deposited at rate of about 0.3 Å/s at 100°C substrate temperature. The rate of deposition was monitored *in-situ* by a quartz crystal monitor.

Fig 2.1: *A photograph of a HIND HIVAC evaporation system*

The powders of elemental boron (99.0%, Alfa Aeser), elemental graphite (99.5%, BARC) and homogenized powders consisting of elemental boron and graphite in 80/20, 70/30 and 50/50 weight proportions were pressed into about 1 mm thick and 20 mm diameter discs to serve as targets. The powders of boron carbide (~99.5 %) were also examined after pressing them into discs of similar dimensions. In addition, a large number of sintered boron carbide discs obtained from BARC were also analysed. These were prepared by carbothermic reduction of boric acid (H_3BO_3) **[95]**.The sintered specimens were identical in shape and size, and measured 16.5 mm in length and 17.4 mm in diameter. A typical sintered boron carbide disc is shown in **Fig 2.2.** Incidentally, the powders of elemental boron and graphite were of natural isotopic abundance while the sintered discs of boron carbide had different $^{10}B/^{11}B$ isotopic ratio.

Fig 2.2: A photograph of sintered boron carbide pellet

2.3 Measurements with ion beam techniques: Basic considerations

The ion beam analysis experiments involved the following steps:

a. Irradiation of samples with a beam of energetic particles,

b. Detection of radiation and data acquisition and

c. Data reduction for qualitative and quantitative analysis

The three processes involved in the experiment are depicted in **Fig 2.3** for illustration

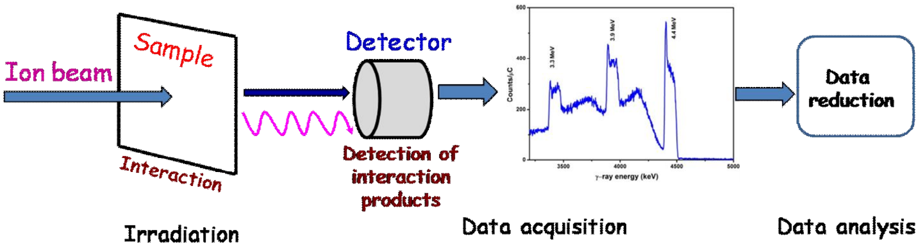

Fig 2.3: Steps involved in the ion beam analysis experiments

2.3.1 Irradiation of samples with energetic particle (beam)

The irradiation of a target with energetic particles (ion beams) is the first step any IBA experiment. The ion beams are obtained from a particle accelerator which can be (a) a Van de graaff accelerator or (b) a Tandem accelerator with terminal voltage in 1 – 5 MV range. The Van de graaff is a single ended machine while in a tandem accelerator, the acceleration takes place in two stages. The basic principles and the working of the two kinds of accelerator are described in references **[96]**. However, a brief account of the tandem accelerator used in the present investigations is given in **Section 2.6.**

The ion beam experiments are conducted in a scattering chamber. The ion beam, on exiting from the accelerator, is transported to the scattering chamber through a beamline that houses beam focussing devices, collimators and other gadgets. The scattering chamber and the beamlines are made up of stainless steel. The targets are fixed on a X-Y or X-Y-Z sample manipulator which, in turn, is mounted on the scattering chamber. The chamber also houses such gadgets as collimators and electron suppressor. The radiation detectors are located inside or outside the scattering chamber at a predetermined angle with respect to the beam direction. The scattering chamber also has provision for Faraday cup for charge integration and has several ports which are used for multiple purposes. The experiments are conducted in high (10^{-6} torr) vacuum. This is to avoid any loss of beam energy and also to ensure the cleanliness of the sample surfaces. Therefore high vacuum is maintained all along the beam path i.e. right from the ion source (place of generation) to the scattering chamber. The vacuum is created by (several) vacuum pumps fixed at different locations along the beam path **[97]**. Incidentally, PIGE and PIXE experiments can also be conducted in non-vacuum conditions wherein the energetic beam is taken out of the beamline or scattering chamber through a suitable thin exit window. The exit window isolates the vacuum of the entire accelerator system from the ambience of the laboratory. Non-vacuum PIGE or PIXE is generally used for analysing large or odd shaped objects **[98,99]**. Objects not compatible with vacuum are also analysed by these methods.

2.3.2 Detection of radiation and data acquisition

As described in **Chapter 1, Section 1.6, 1.7** and **1.8**, PIGE involves detection of prompt γ-rays emitted from a nuclear reaction while NRA and backscattering spectrometry (BS) are based on the detection of charged particles resulting from a nuclear reaction and a backscattering event respectively. Thus the detection of the nuclear radiations is a vital component of an ion beam experiment. The nuclear radiations, γ-rays or charged particles are detected by specific detectors which are made up of materials possessing certain distinct properties. The detection is based on the interaction of the radiation with the detector material. The radiation loses its energy to the material by way of these interactions (described later). This energy is spent in exciting and ionising the atoms of the medium. The ionisation leads to the generation of an electric current (free charge carriers) while, the excited species can undergo de-excitation emitting a luminescent photons in the process. The measurement of the electric current or the photons forms the basis of the detection of the radiation.

2.3.3 Electronics for data acquisition

The electrical signals generated in the detector are very small and therefore need to be amplified. For amplification and processing of the basic detector signal, suitable electronics is required. The signal amplification is achieved through a combination of pre-amplifier and amplifier with the former mounted close to the detector **[100]**. **Fig 2.4** gives a block diagram of the electronics setup used in the present studies.

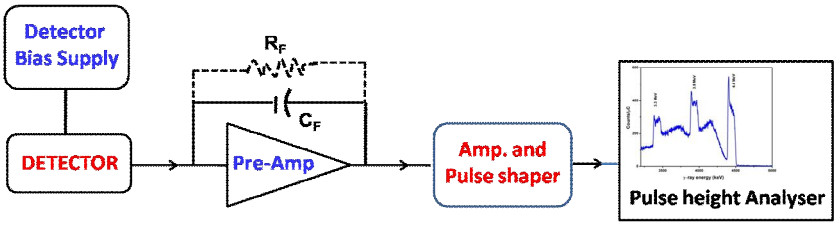

Fig 2.4: Block diagram of electronics setup

2.3.4 Data reduction for qualitative and quantitative analysis

Elemental (isotopic) identification and quantification are the two main objectives of an analytical endeavour. The qualitative analysis by PIGE or PIXE is often unambiguous as the γ-rays or X-rays of different isotopes or elements are well-documented. In NRA, the identification of an isotope is based on the energy of the ejecticles and or γ-rays emitted from the nuclear reaction. Care must be exercised while determining the energy of ejecticles as these would lose energy in stopper foils or any overlying layer on the sample. An improper accounting of the energy of the ejectiles would bring about ambiguity and can cause serious errors in not only in qualitative analysis but in quantification as well. So far as the quantification **[101]** is concerned, two methods can be employed. The first method is based on fundamental principles wherein the concentration of an isotope is derived by solving a yield equation made up of basic factors that define the propagation of the beam in the sample, the occurrence of the nuclear reaction and the detection process. The second method is the relative method wherein the knowledge of the different parameters as described earlier is not mandatory. The method utilizes reference targets or standards which are examined under identical conditions as those of samples. The details of the methods and also the software and simulation codes such as SRIM and SIMNRA used in the qualitative and quantitative analyses are described in the subsequent sections **[102,103]**.

*2.*4 Interaction of radiation with matter

For a comprehensive understanding of the functioning of detectors and for an unambiguous spectral and quantitative analysis, a fair knowledge of the interaction of radiation with matter is desirable. It is important to note that the charged and neutral (γ-ray) radiations interact with the matter in qualitatively different ways. The processes involved in the interaction of the two types of radiations with matter are described briefly in the following sections.

2.4.1 Interaction of charged particles with matter: Concept of stopping power

The energetic charged particles interact primarily with the electrons of the atoms and molecules of the medium by way of Coulombic interactions and lose energy through the excitation and ionisation of the atoms of the medium. The concept underlying the interaction of charged particle with the matter and the resulting energy loss is described by stopping power or stopping cross-section **[88,104,105]**.

An energetic charged particle travelling through a material – an element or a compound – loses energy in steps. The loss in the energy experienced by the particle is represented in terms of stopping power. It essentially signifies the capability of a material to cause decrement in the energy of moving charge particle and is defined as the energy lost by the particle in travelling unit distance through the material. The stopping power is described by the equation

$$S(E) = -\frac{dE}{dx} \qquad (2.1)$$

and has the units of eV/Å or keV/μm. The energy loss of the particle arises from its interaction with the (a) atomic nuclei and (b) electrons of the material. As a result, S(E) is often represented as

$$S(E) = S(E)_n + S(E)_e \qquad (2.2)$$

where $S(E)_n$ is the nuclear stopping and $S(E)_e$ is the electronic stopping. The two interactions are independent of each other, but depend on the energy of the particle.

The nuclear stopping originates from elastic collisions with the screened / unscreened nuclei, wherein a portion of the particle energy is transferred to the atom, resulting in its translatory motion. Nuclear stopping is of fundamental importance in the process of sputtering. Importantly, no nuclear reaction is involved during nuclear stopping.

The electronic stopping on the other hand, arises from inelastic collision, wherein the energy transferred from the particles is spent in the excitation / ionisation of the bound or free electrons of the material.

The stopping power of a material can be calculated using SRIM software **[102]**. **Table 2.1 and 2.2** show the electronic stopping, nuclear stopping and the net stopping power of some elements as well as compounds for protons and α- particles of 50 keV and 1 MeV energies. It can be observed that the stopping power increases with the z or mass of the target and that of projectile and decreases with the increase in the energy of projectile. In fact, the energy dependence of the stopping power, in general, and the relative contributions of electronic and nuclear stoppings can more clearly visualised in **Fig 2.5** and **2.6** which show the electronic and nuclear stopping powers of silicon and copper for 10 keV – 4 MeV protons and α- particles respectively.

Two important inferences that emerge from an examination of the stopping powers vs. particle energy plots in **Fig.2.5** and **2.6** are: (a) nuclear stopping is substantial only at lower projectile energy and is negligibly small at higher energy and (b) the electronic stopping, first increases with increase in the projectile energy, reaches a maximum and subsequently decrease with further increase in the projectile energy.

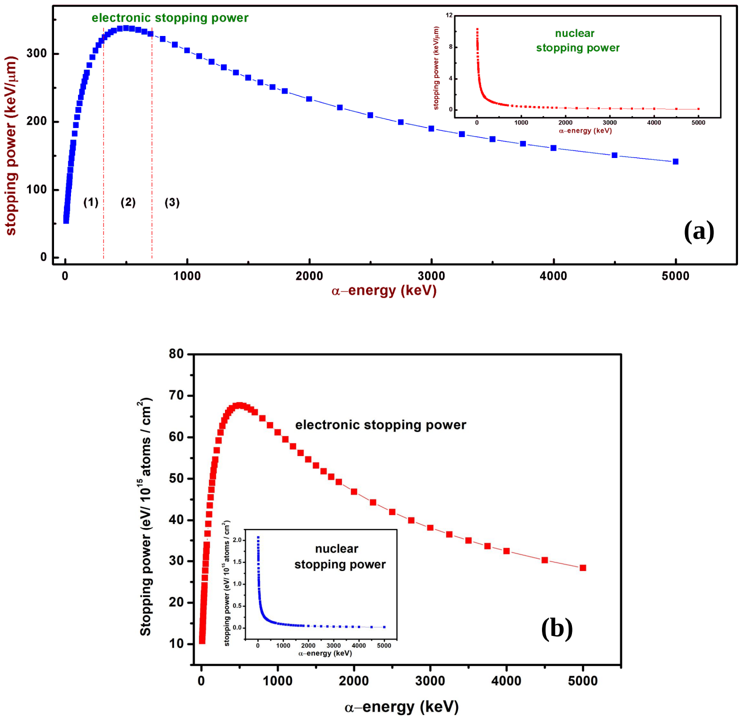

Fig 2.5: *Stopping power of Si in (a) keV/μm and (b) eV/10^{15}atoms/cm^2 as a function of α-particles energy*

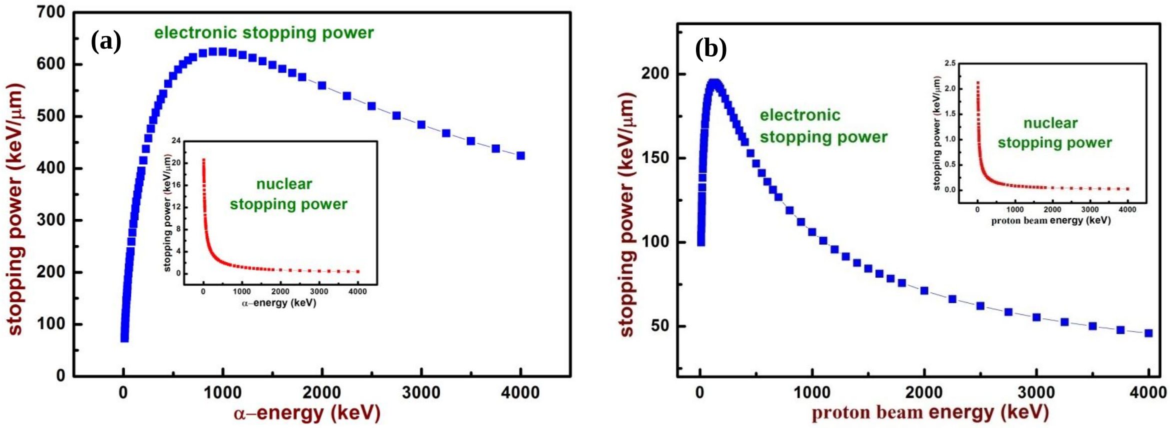

Fig 2.6: *Stopping power of copper as a function of (a) α-particles and (b) protons energy*

The overall predominance of the electronic stopping stems from the fact that electrons, due to their lighter mass, absorb more energy in a collision in comparison to the nuclei. The predominance of the nuclear stopping at lower energy can be attributed to lower velocity of the moving atom in comparison to the electrons of the target, which makes their excitation rather improbable. Conversely, the excitation / ionisation of the target electrons becomes more probable at higher projectile energy, wherein, its velocity is greater than or equal to the velocity of electrons of the target **[88]**. Furthermore, it is generally accepted as a rule of thumb, that excitation / ionisation of electrons (inelastic collision) is not significant for atoms moving with the energy (in keV) lower than its atomic weight. Thus this limiting energy is 1 keV for protons, 2 keV for deuterons and 65 keV for Cu atoms.

The plot (**Fig 2.5**) portraying the variation of electronic stopping with particle energy, as such, can be divided into three regions. In the first region the electronic stopping increases with particle energy, in the second region it passes through a maximum and subsequently decreases while in the third it decreases monotonously with increase in energy.

The experiments the present study were conducted with protons while their energy fell under the realm of the third region, which is also known as Bethe- Bloch region, as herein the electronic stopping is given by the Bethe-Bloch formula **[106].**

$$-\frac{dE}{dx} = \frac{4\pi \mathrm{e}^4 z^2}{m_0 v^2}\mathrm{NB} \qquad (2.3)$$

$$B \equiv Z\left[\ln\frac{2m_0v^2}{I} - \ln\left(1-\frac{v^2}{c^2}\right) - \frac{v^2}{c^2}\right] \qquad (2.4)$$

The formula describes the variation of electronic stopping not only with the particle energy, but also with the atomic density (N), atomic number and mass of the projectile and the atomic number of the target elements.

The three regions are separated by comparing the velocity of the projectile with Thomas- Fermi velocity $z_1^{2/3}v_0$, where v_0 is the Bohr velocity

$$v_0 = \frac{e^2}{\hbar} = 2.2\times10^8 cm/s \qquad (2.5)$$

In the first region, only those electrons close to the Fermi level are excited and hence the stopping is comparatively lower. The maximum stopping occurs in the second region around the energy equivalent to $z_1^{2/3}v_0$, i.e, 25 keV for protons and 250keV for α- particles. In the third region, the energy of the projectile is very high and thus it spends progressively lesser time for interaction with the electrons and hence the stopping power decreases **[88]**.

***Table 2.1**: Stopping power, range and straggling of protons and alpha particles in elemental Si and Au calculated using SRIM*

Element	Energy (keV/MeV)	Stopping power (keV/µm)			Range (Å/µm)	Straggling (Å/µm)	
		Electronic	Nuclear	Net		Longitudinal	Lateral
				Proton			
Si	50 keV	124.9	0.34	125.2	4704Å	814Å	942Å
	1MeV	40.73	0.03	40.76	16.33 µm	7871 Å	9972 Å
	4MeV	16.03	0.01	16.04	148.36 µm	6.11 µm	7.24 µm
Au	50keV	171.7	0.89	172.6	1963Å	1147Å	998 Å
	1MeV	121.1	0.12	5.51	5.51µm	7015Å	1.02 µm
	4MeV	61.09	0.04	61.13	41.33µm	3.37µm	5.81µm
				Alpha			
Si	50 keV	138.0	4.15	142.15	4194 Å	1266 Å	1265 Å
	1MeV	304.6	0.42	305.03	3.51µm	2237 Å	2874 Å
	4MeV	161.3	0.13	161.43	17.76µm	6619 Å	6478 Å
Au	50keV	209.8	9.49	219.29	1113 Å	954 Å	762 Å
	1MeV	731.8	1.55	733.35	1.51µm	2990 Å	3426 Å
	4MeV	504.4	0.53	504.93	6.29µm	5090 Å	7472 Å

The stopping power can be expressed in several units. While energy loss in terms of eV/Å or keV/µm is most frequently used, some of the other units used are

$$\frac{1}{\rho}\frac{dE}{dx} \rightarrow keV/\left(mg/cm^2\right) \qquad (or) \qquad \frac{1}{N}\frac{dE}{dx} \rightarrow eV/\left(atoms/cm^2\right)$$

where ρ is the density(g/cm^3) and N is the atomic density (atoms/cm^3). The stopping power expressed in terms of keV/µm depends on the density of target, where as stopping power when expressed in the latter two units are independent of density. Since the density of a material, may be different from its theoretical density, the stopping power is generally expressed in terms of stopping cross-section **[88]** to avoid any ambiguity. The stopping cross-section ε is defined as

$$\varepsilon = \frac{1}{N}\frac{dE}{dx} \qquad (2.6)$$

ε is expressed in terms of eV/ (atoms/cm^2)

***Table 2.2**: Stopping power, range and straggling of protons and alpha particles in some binary and ternary compounds (B_4C, Si_3N_4 and Li_2TiO_3) calculated using SRIM*

Compound	Energy	Stopping power (keV/μm)			Range (Å/μm)	Straggling (Å/μm)	
		Electronic	Nuclear	Net		Longitudinal	Lateral
Proton							
B_4C	50 keV	187.6	0.42	188.02	3555 Å	382 Å	488 Å
	1MeV	54.7	0.03	54.73	11.58 μm	4967 Å	3919 Å
	4MeV	20.24	0.01	20.25	114.58 μm	4.4 μm	3.19 μm
Si_3N_4	50keV	187.2	0.5	187.7	3340 Å	528 Å	623 Å
	1MeV	59.69	0.04	59.73	10.91 μm	5055 Å	5743 Å
	4MeV	23.68	0.01	23.69	99.79 μm	3.99 μm	4.22 μm
Li_2TiO_3	50keV	173.5	0.48	174.0	3648 Å	643 Å	740 Å
	1MeV	61.45	0.04	61.49	10.62 μm	5033 Å	5969 Å
	4MeV	24.16	0.01	24.17	97.7 μm	3.97 μm	4.42 μm
Alpha							
B_4C	50 keV	257.1	5.34	262.44	2520 Å	386 Å	443 Å
	1MeV	471.2	0.48	471.68	2.27 μm	893 Å	1002 Å
	4MeV	230.4	0.14	230.54	11.88 μm	4035 Å	2281 Å
Si_3N_4	50keV	199.0	6.21	205.21	2945 Å	769 Å	794 Å
	1MeV	481.5	0.61	482.1	2.37 μm	1374 Å	1779 Å
	4MeV	247.1	0.187	247.3	11.55 μm	4159 Å	3678 Å
Li_2TiO_3	50keV	184.5	6.0	190.5	3027 Å	837 Å	852 Å
	1MeV	487.5	0.59	488.1	2.43 μm	1524 Å	1994 Å
	4MeV	254.8	0.18	255.0	11.32 μm	4133 Å	3946 Å

For a multi-elemental target, the stopping power (cross-section) is represented by the summation of the stopping powers (cross-sections) of individual elements weighted by their respective abundances in the target. This is known as Bragg's rule of linear additivity **[88]**.

As a result, the stopping cross-sections of B_4C, Li_2TiO_3, $LiFePO_4$ are can be calculated by the formula

$$\varepsilon_{B_4C} = \frac{4}{5}\varepsilon_B + \frac{1}{5}\varepsilon_C \qquad (2.7a)$$

$$\varepsilon_{Li_2TiO_3} = \frac{2}{6}\varepsilon_{Li} + \frac{1}{6}\varepsilon_{Ti} + \frac{3}{6}\varepsilon_O \qquad (2.7b)$$

$$\varepsilon_{LiFePO_4} = \frac{1}{7}\varepsilon_{Li} + \frac{1}{7}\varepsilon_{Fe} + + \frac{1}{7}\varepsilon_P + \frac{4}{7}\varepsilon_O \qquad (2.7c)$$

where ε_i is the stopping cross-section of element i, for 1MeV protons. The stopping cross-sections of these compounds calculated from the above formulae are given in **Table 2.2.**

The loss of energy experienced by particle is a statistical process, which is expressed in terms of straggling. The straggling depends upon the atomic number of the ion beam and that of the target, and on the number density of the target. It shows rather weak dependence on energy.

2.4.2 Interaction of γ-rays with matter

The γ-rays can interact with material in multiple ways. However, only three interactions viz, photoelectric effect, Compton scattering and pair production **[104,105]** are used for the detection and measurement of γ-rays.

(a) Photoelectric effect

The photoelectric effect involves ejection of energetic electrons from one of the bound shells, following the complete absorption of X-ray by the conserved electron. As a consequence, the photoelectron appears with an energy

$$\mathrm{E_c} = h\upsilon - E_b \qquad (2.8)$$

where $h\upsilon$ is the energy of γ-rays and E_b is the binding energy of the photoelectron.

A schematic of the photoelectric effect is given in **Fig 2.7**.

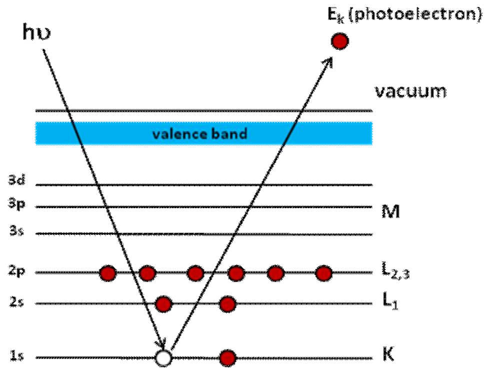

Fig 2.7: *A schematic of photoelectric effect*

The photoelectric absorption cross-section varies as $\tau \cong c \times \frac{Z^n}{E_\gamma^{3.5}}$ (2.9)

where n varies from 4-5, Z is the atomic number of the element and E_γ is the energy of the incident γ-rays. Evidently the photoelectric effect is more pronounced in high Z materials in low energy regions. As a result, high Z materials are generally used as detector materials.

(b) *Compton scattering*

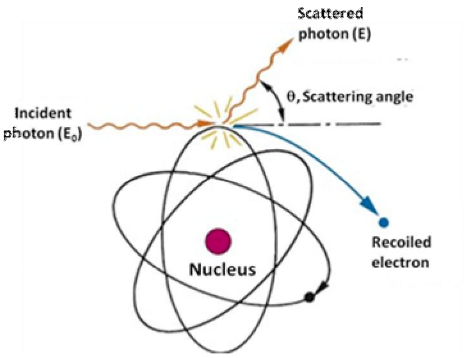

Fig 2.8: *A schematic of Compton scattering*

The scattering is a consequence of the transfer of a certain fraction of photon energy to the electron of the material; such an electron is termed as a recoil electron. The Compton scattering therefore results in a creation of a recoiled electron and a scattered γ-ray photon **[104]**. The energy of the scattered γ-ray photon (hυ′) and that of the recoiled electron (E_e) can be given by the formulae

$$h\upsilon' = \frac{h\upsilon}{1+\left(h\upsilon/m_0c^2\right)\left(1-\cos\theta\right)} \qquad (2.10)$$

$$E_e \quad = h\upsilon - h\upsilon' = h\upsilon\left(\frac{\left(h\upsilon/m_0c^2\right)\left(1-\cos\theta\right)}{1+\left(h\upsilon/m_0c^2\right)\left(1-\cos\theta\right)}\right) \qquad (2.11)$$

where hυ is the energy of the incident beam, θ is the scattering angle of the photon and m_0c^2 is the rest mass of an electron. In normal circumstances the scattering event will takes place at all angles from θ=0° to θ=180°. As a result, a continuum of energies can be transferred from the γ-rays to the electrons. The gap between the maximum Compton recoil electron energy and the incident γ-ray energy is given by

$$E_C \quad = h\upsilon - E_e(\theta=\pi) = \frac{h\upsilon}{1+\left(2h\upsilon/m_0c^2\right)} \qquad (2.12)$$

Therefore the gap between the full energy peak and the Compton edge for 1 MeV γ-rays is 0.203 MeV while it is 0.226, 0.235 and 0.240 MeV for 2, 3 and 4 MeV γ-rays respectively. The electron energy distribution for γ-rays of energy hυ (1MeV), and E_c are shown in the **Fig. 2.9.**

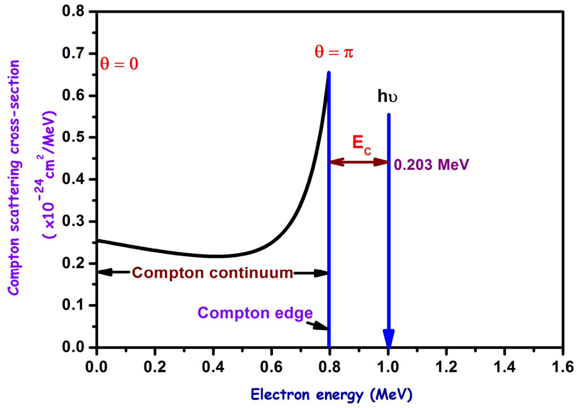

***Fig 2.9**: Electron energy vs Compton scattering cross-section for 1 MeV γ-ray photons*

(c) Pair Production

Pair production represents the third most important interaction between the γ-rays and matter and occurs with γ-rays having energy more than $2m_0c^2$ i.e. 1.02 MeV. It corresponds to the creation of an electron (e^-) and positron (e^+) pair in the electrostatic field of the nucleus of the absorbing material **[104,105]**. The incident photon is totally absorbed in this mode of interaction and the energy in excess of 1.02 MeV is shared by the electron and the positron as their kinetic energy as per the following formula

$$E_{e^-} + E_{e^+} = h\upsilon - 2m_0c^2 \qquad (2.13)$$

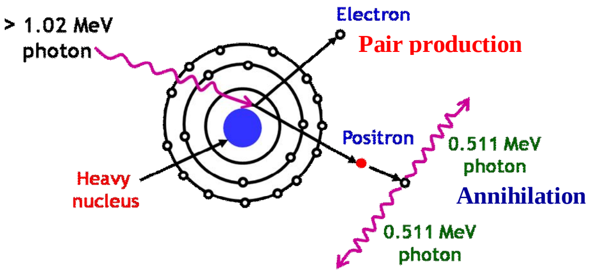

***Fig 2.10**: A schematic of pair production and annihilation*

A schematic of pair production and annihilation processes is given in **Fig 2.10**. The electron and the positron thus produced lose their energy by way of excitation and ionisation in the detector medium. The positron, on thermalisation, undergoes annihilation by combining with an electron in the medium **[104]**. The annihilation results in the production of two photons with each having 511 keV energy which is equivalent to the total rest mass of an electron-positron pair. The two annihilation photons move in opposite directions and may interact with the detector medium and may get absorbed or escape. The absorption of both the photons contributes to the full energy peak. However, if one photon escapes, the energy deposited is (E_γ-511) keV while if both photons escape, the energy deposited is (E_γ-1022) keV. The γ-ray spectrum may contain peaks at (E_γ-511) keV and or (E_γ-1022) keV which are termed as single escape peak and double escape peak respectively. **Fig.2.11** shows the spectrum of 3089 keV γ-rays acquired with a HPGe detector wherein the full energy peak that corresponds to the photoelectric effect; the Compton edge, the outcome of the Compton scattering process and the first and second escape peaks resulting from the phenomenon of pair production- are seen vividly.

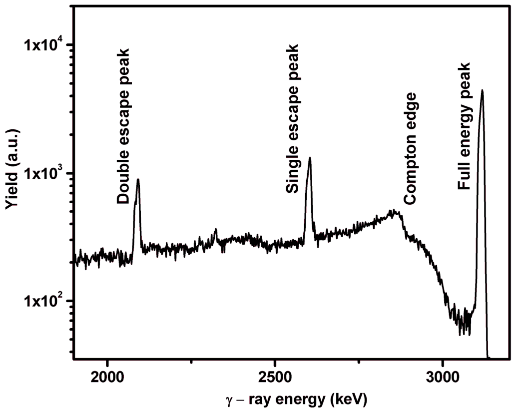

***Fig 2.11**: High resolution γ-ray spectrum of 3089 keV γ-rays acquired with a HPGe detector.*

The cross-section of pair production is given by the expression

$$\sigma_{pp} \propto Z^2 \cdot \ln(E_\gamma - 2m_0c^2) \qquad (2.14)$$

The interaction becomes important for 5 MeV or higher energy γ-rays. It is instructive to mention that the the pair production can also occur in the electric field of an electron, however, the minimum energy for the production to take place is 4 m_0c^2 **[104]**.

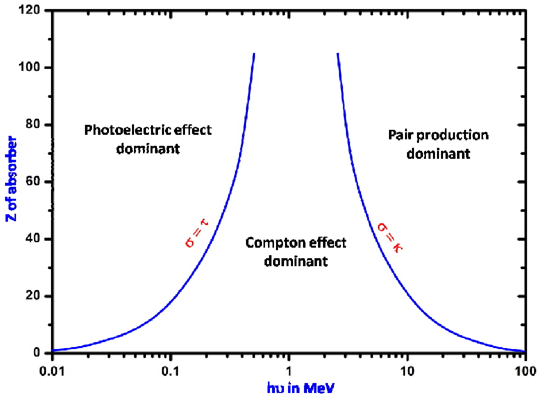

***Fig 2.12**: Probability of occurrence of the photoelectric effect, Compton scattering and pair production as a function of energy of the γ-rays*

The probability of the occurrence of the three processes i.e. photoelectric effect, Compton scattering and pair production as a function of energy of the γ-rays and the atomic number of the interaction medium is shown in **Fig.2.12**.

(d) Attenuation coefficients

As described earlier, the γ-rays traversing through a medium can undergo interaction by way of photo electric effect, Compton scattering and in permissible energy range through pair production. The photons undergoing these interactions are removed from the main beam which can be termed as attenuation **[68,104]**. In other words, the attenuation coefficient is a measure of primary γ-rays which have interactions via these processes so it can be written as

$$\mu = \tau\ (\text{photo electric}) + \sigma\ (\text{Compton}) + \kappa\ (\text{pair}) \qquad (2.15)$$

The μ is known as linear attenuation coefficient and has the dimensions of length^{-1} i.e, cm^{-1}. A schematic of attenuation of γ-rays passing through a medium of thickness 't' in shown in the **Fig 2.13.**

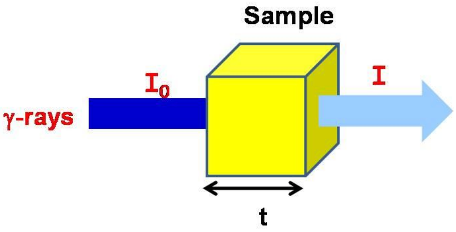

Fig 2.13*: A schematic of attenuation of γ-rays*

The concept of attenuation coefficient is very important to determine the number of photons that emerge out of an absorber. The relationship between the intensity of the incident (I_0) and that of the transmitted (I) photons can be given as

$$I = I_0 e^{-\mu t} \qquad (2.16)$$

The attenuation coefficient has another variant which is known as mass attenuation coefficient which is obtained by dividing the linear attenuation coefficient by the density of the absorber material. The mass attenuation (μ_m) coefficient is generally expressed as (μ/ρ) and has the units of cm^2/gm. The mass attenuation coefficient is more fundamental in nature as it is independent of the actual density and the physical state i.e, gas, liquid or solid of the absorber.

$$I = I_0 e^{-\mu_m \rho t} \qquad (2.17)$$

At this juncture, it is instructive to mention that the photons do not lose any energy while traversing through a medium, though there is an absorption or attenuation of photons. In contrast the charged particles passing through a medium experience loss of energy which, as described earlier, is given by the stopping power or stopping cross-section while there is no discernable change in the intensity of the beam.

It is seen that the stopping power for charged particles is analogous to linear attenuation coefficient of photons; while the stopping cross-section for the former bears resemblance with the mass attenuation coefficient. (The stopping cross-section and mass attenuation coefficient are independent of density of the material).

2.5 Detection of nuclear radiation

As mentioned earlier, a radiation detector detects a radiation by measuring its energy. A charged particle deposits its energy in a medium by interacting with its nuclei and electrons while γ-rays deposit their energy by way of interactions that involve photoelectric effect, Compton scattering and pair production. The net result of these energy loss processes is the generation of an electric current or the production of luminescent photons. The nuclear detectors, in essence, work by sensing the electric current or the luminescent photons and therefore are often classified as ionisation or scintillator detectors **[104,105]**. In the present work the charged particles have been detected by a Passivated Implanted Planar Silicon (PIPS) detector while, the γ-rays have been detected by either scintillator detectors (NaI(Tl) and bismuth germanate ($Bi_4Ge_3O_{12}$-BGO) or by ionisation detector semiconductor detector.

2.5.1 Charged particle detectors

The silicon charged particle detector is made of silicon wafer, having surface contacts that form a p-n junction. These contacts may be junction (doped) contacts as in the modern high-performance Passivated Implanted Planar Silicon (PIPS) detectors or may be surface barriers (thin metal films) as in the case of the conventional Surface Barrier detectors **[104,105]**. In order to establish an electric field across the device, a bias voltage is applied in the reverse direction which helps in the formation of a depletion region. The thickness of the depletion region should be more than the range of particles to be detected.

During the detection, the particle is stopped in the depletion region and electron-hole pairs are formed in the process. The energy required to form a single electron-hole pair depends on the detector material and is independent of the energy of the incoming particle. Hence the total number of electron-hole pairs formed is directly proportional to the energy of the particle. The electric field in this region sweeps the electrons to one terminal and the holes to the other and creates a charge pulse. The charge pulse is integrated to a detectable voltage pulse, using a charge sensitive pre-amplifier.

2.5.2 High purity germanium (HPGe)

HPGe detector is a semiconductor detector and, as the name suggests, is made up of a high purity Ge single crystal. The total concentration of impurities in the crystal is ~10^{10} atoms/cm^3. A high purity Ge crystal tends to be p-type either due to the residual acceptor impurities or to acceptor centres associated with the lattice defects. The n^+ contact on the one side of the crystal is normally made by the controlled diffusion of Li while a non-injecting contact on the other side is achieved by a metal to semiconductor surface barrier by evaporating a thin layer of gold, platinum or palladium. The detector thus essentially has n^+-p-p^+ configuration in which the depletion region is formed by reverse biasing the n^+-p junction **[104]**. HPGe is operated at liquid nitrogen temperature and it exists in planar and coaxial geometries. A schematic of a HPGe detector along with the liquid nitrogen dewar is shown in **Fig. 2.14.**

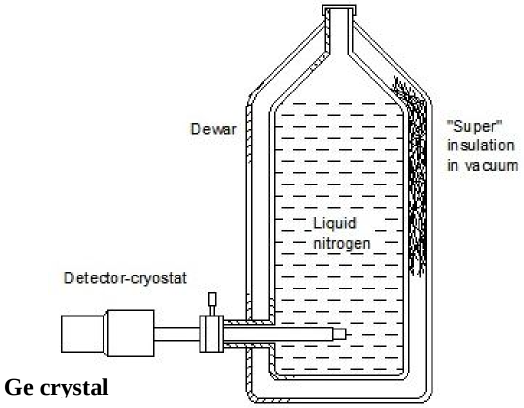

Fig. 2.14: *A schematic of a HPGe detector*

2.5.3 Scintillator detectors (NaI(Tl) / BGO)

As described earlier, the detection of radiation by a scintillator detector is based on the measurement of scintillation (photons) in the medium produced by the radiation. A scintillating material should possess certain properties for its utilisation as a nuclear radiation detector. These properties are described detailed in reference **[104]** which include

i) It should convert the kinetic energy of the ionizing radiation into detectable light

ii) The efficiency of conversion should be high and linear and

iii) The scintillating material should be transparent to the wavelength of its own emission

A scintillator detector essentially consists of two components a) a scintillating material and b) photomultiplier tube. The scintillator is optically coupled with a photomultiplier. The photomultiplier converts the weak light signals from the scintillator into a measurable electrical signal and thus enables the detection of the radiation. The photomultiplier tube (**Fig 2.15**) is made of a photocathode and an electron multiplier structure. The photocathodes converts the incident light photons (from the scintillator material) into low energy electrons, which are amplified through the multiplier structure to produce 10^7 to 10^{10} electrons which is collected at the anode or the output stage of the multiplier.

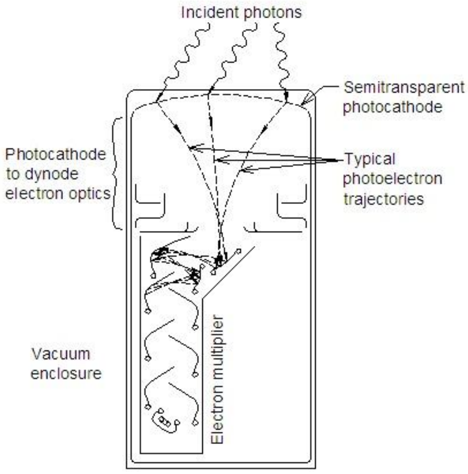

Fig 2.15*: Schematics of the processes involved in photomultiplier tube*

NaI(Tl) (Thallium doped NaI) and BGO, by virtue of high Z of the constituents and good optical absorption and emission characteristics, are the two important and most widely used scintillator detectors**[104]**. The NaI(Tl) contains about 10^{-3} mole fraction of thallium(Tl) as an activator. The absolute scintillation efficiency of Tl activated NaI is about 12%. BGO in comparison, does not contain any activator and its luminescent property is associated with an optical transition of Bi^{3+} ion. The BGO has relatively poor scintillation efficiency which at 2.8%, is about 20% of that of NaI(Tl). It is important to note that the scintillation efficiency of BGO as such depends strongly on the purity of the crystal.

2.5.4 Properties of detectors

A detector is characterised by several features amongst which (detector) efficiency and resolution are of paramount importance in analytical applications. Efficiency that represents the efficacy of a detector in registering the incident nuclear radiation is classified into absolute and intrinsic categories **[104,105]**. The absolute efficiency can be defined as

$$\varepsilon_{abs} = \frac{number\ of\ \ pulses\ recorded}{number\ of\ \ radiation\ quanta\ emitted\ by\ source} \tag{2.18}$$

whereas the intrinsic efficiency can be defined as

$$\varepsilon_{\text{int}} = \frac{number\ of\ \ pulses\ recorded}{number\ of\ \ quanta\ incident\ on\ detector} \tag{2.19}$$

therefore the absolute efficiency and intrinsic efficiency are related through the equation

$$\varepsilon_{\text{int}} = \varepsilon_{abs}\ (4\pi / \Omega) \qquad (2.20)$$

where Ω is the solid angle that the detector subtends at the radiation emitting source. The intrinsic efficiency depends on the detector material, the radiation energy (inverse dependence) and the physical thickness of the detector. It has rather less pronounced dependence on other geometrical parameters (Ω) and is therefore much easier to calculate.

Energy resolution represents the ability of detector to distinguish two radiations of nearby energies. The smaller the value of the energy resolution, the better is the capability of the detector to detect such radiations. The energy resolution (R) is represented by the full width at half maximum (FWHM) of a peak divided by its energy centroid (E_0):

$$R = \frac{FWHM}{\mathrm{E}_0} \qquad (2.21)$$

It is to be noted that for a Gaussian peak with standard deviation σ, FWHM is given by 2.32σ.

The energy resolution of detector has contributions from charge collection statistics, electronic noise, drift in operating parameters during the course of the measurements and the variations in the detector response over its active volume. The energy resolution as such decreases with energy and for γ-rays **[104]**, the variation of R with energy E is given by the formula

$$\ln R = \ln K - \frac{1}{2}\ln \mathrm{E} \qquad (2.22)$$

where K is a constant.

2.6 Experimental Details

The PIGE measurements and also NRA and BS experiments were performed using the 3 MV Tandetron (High Voltage Engineering Europa, The Netherlands) at the Surface and Profile Measurement Laboratory of NCCCM, Hyderabad. The Tandetron, as the name suggests, is a tandem type accelerator with both low and high energy ends at ground potential. The final energy of the particle emerging from the accelerator is due to its acceleration in two stages. The operation of a tandem accelerator involves the following three steps: (a) the production of low energy single negatively charged ions at an ion source **[107]** and their acceleration (as the first stage) to the positive high voltage terminal, (b) the conversion of the single negatively charged ions into single or multiple positively charged ions at the terminal **[108]** and (c) acceleration (as the second stage) of the positively charged particle to the ground. The final energy of the ion beam depends on the charge state of the ion (q) and the applied terminal voltage (TV) and is given by the relationship

$$\mathrm{E} = \left(q+1\right) TV \qquad (2.23)$$

The experiments were conducted with 3 – 4.2 MeV proton beam. The salient features of the Tandetron, and the irradiation and detection conditions of the measurements are described below.

2.6.1 3 MV Tandetron facility at NCCCM, Hyderabad

The tandetron consists of three major components namely; i) injection system, ii) accelerator and iii) experimental end-stations. The injector system consists of two ion sources: a) Duoplasmatron and b) Sputter ion source and several different beam guiding systems. Duoplasmatron source produces the beams of H^- and He^+ ions. The He^+ ions are converted into He^- ions in a lithium charge exchange canal. A 90° bending magnet with a mass energy product of 8.8 MeV amu and a resolving power of 100 directs the beam in to the accelerator. The injector system also consists of a Q-snout to produce a beam waist at the stripper for the conversion of the negative ions into positive ions. A pictorial view of the injector system is given in **Fig 2.16**.

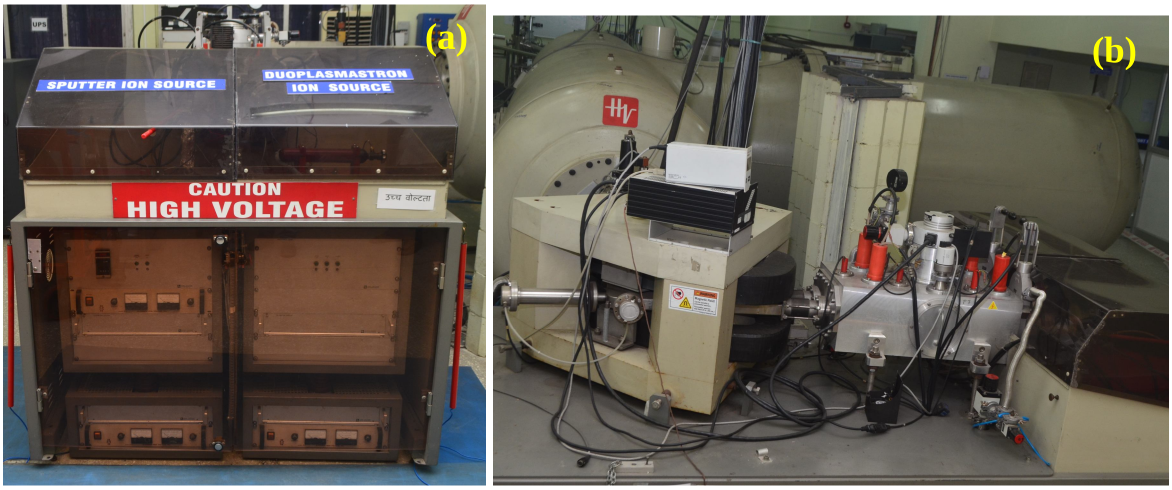

Fig 2.16*: Injector system of 3 MV Tandetron at NCCCM, Hyderabad: (a) ion sources and (b) 90° bending magnet.*

The accelerator consists of high voltage power supply, accelerating tubes and a terminal with a stripper and stripper gas re-circulation system. These are housed in a T-shaped tank that is filled with 7 bar of SF_6 gas **[109]**. The high voltage power supply is a solid-state power supply based on Cockcroft – Walton principle. It consists of high voltage multiplier and rectifier stacks with two driver electrodes, and a high voltage end mates with the dome at the terminal.

The accelerating tubes, designated as low and high energy accelerating tubes, are made of titanium electrodes sandwiched between glass insulation rings. The electrodes have central hole for the passage of ion beams. The electrodes are surrounded by equi-potential rings to reduce electrical stress and to prevent corona and sparking. A vacuum of 10^{-6} torr or better is maintained in the accelerating tube using turbomolecular pumps **[97]**, which are located outside the pressure vessel.

The high voltage terminal is located at the centre of the pressure vessel between the low and high energy acceleration tubes. A gas stripper at the terminal converts the single negatively charged ions into positive ions. The stripper has a turbomolecular pump for the re-circulation of the stripper (nitrogen gas). Depending on atomic number, the charge state (q) of the ions emerging from the stripper can be $\geq +1$.

The high energy extension of the accelerator outside the pressure tank consists of a quadrupole triplet lens for the focussing of the beam and a high energy switching magnet for directing the beam in one of the four (± 15°, ± 30°) experimental beam lines which are dedicated to NRA, RBS, PIGE and PIXE techniques.

A schematic of the 3MV Tandetron showing the major sub-systems and components including the ion sources and the experimental beamlines is shown in **Fig 2.17** while a photograph of the beamlines is shown in **Fig 2.18**. The linear portion of the T-shaped pressure tank is also visible in the photograph.

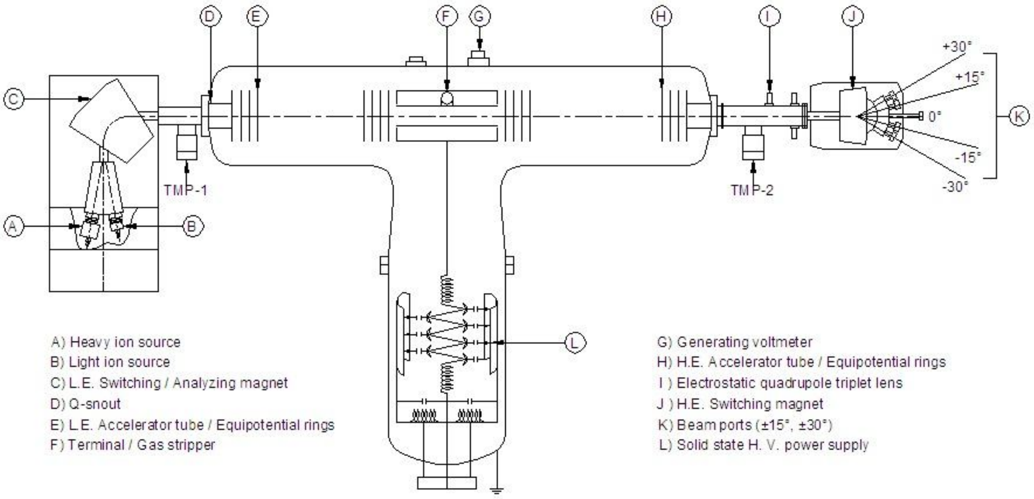

***Fig 2.17**: A schematic of the 3MV Tandetron (HVEE) at NCCCM, Hyderabad.*

***Fig 2.18**: A photograph of experimental beam lines of 3 MV Tandetron at NCCCM, Hyderabad.*

2.6.2 Facility for irradiation

Each beam line is equipped with (i) a vacuum system that comprises turbomolecular pumps, rotary pumps (backing) and vacuum gauges, (ii) beam defining gadgets (for example, collimators), and (iii) a scattering chamber wherein the particle - matter (sample) interaction takes place. Each scattering chamber is fitted with a XY sample manipulator on which the samples are mounted. The chamber also has an electron suppressor, view ports and vacuum feedthroughs for biasing the detectors fixed inside and the electron suppressor (-900V). The electron suppressor surrounds the sample on the XY manipulator which is electrically isolated from the scattering chamber and other gadgetries. It enables an accurate and precise beam current monitoring and charge integration. A vacuum of about 10^{-6} torr is maintained all along the beam path and also in the scattering chambers. **Fig. 2.19** gives a glimpse of the inside view of a typical scattering chamber. A 5KV bias supply (Tennelec; Mod. TC 950A) was used in the present studies.

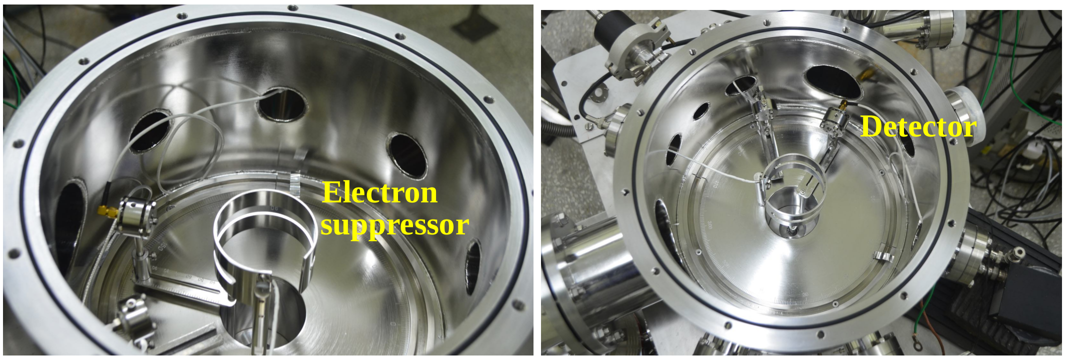

***Fig 2.19**: An inside view of scattering chamber used for RBS measurements*

(a) Irradiation conditions

The targets (pellets and thin films supported on substrates) were irradiated with, as per requirement, 0.4-4.1 MeV protons. The beam was collimated to ~ 1.5 mm diameter using a pair of ‘Ta’ slit assembly before its impingement on the target. Depending on the nature of the target, the beam current ranged from a few nA to a few hundreds of nA. The beam current was read directly from the targets. The dead time during acquisition was kept ≤ 5%. The precise energy, current and other necessary details are described separately in the individual chapters.

(b) Detection and signal processing

The detectors employed for the detection of details of γ-rays and charged particles and their salient features are given in **Table 2.3**.

***Table 2.3**: Details of γ-ray / charged particle detectors used in the present studies*

Detector type	Size	Radiation	Efficiency (%)	FWHM	Bias
Passivated implanted planar silicon; PIPS (Canberra)	Active area: 50 mm^2 Depletion depth: 100 μm	Charged particle	100%	12 keV at 5486 keV alphas from ^{214}Am	+40V
Sodium iodide (Thallium doped); NaI (Tl) (Harshaw; type 12S12)	7.6 cm × 7.6 cm	γ-rays	-	9% at 662 keV of ^{137}Cs	+900V
Bismuth germanate; BGO (Scionix, Holland)	7.6 cm × 7.6 cm	γ-rays	-	10% at 1332 keV of ^{60}Co	+1000V
High purity germanium; HPGe (Bruker Baltic)	5.9 cm × 6.4 cm	γ-rays	36% relative to NaI(Tl)	1.78 keV at 1332 keV of ^{60}Co	+3000V

The γ-ray detectors were positioned in the direction of the beam outside the scattering chamber. They were surrounded by a 2.0 cm thick cylindrical lead shield. The PIGE scattering chamber has a special provision for housing the lead shield of the detector. The experimental arrangement for measurements with HPGe is shown in **Fig. 2.20** while the photographs of the NaI(Tl) and BGO detectors are given in **Fig. 2.21**.

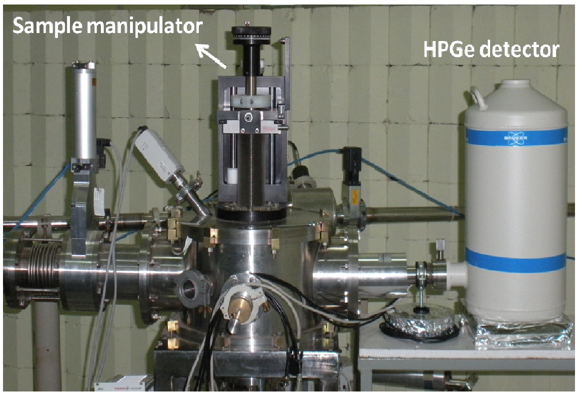

Fig 2.20: *Experimental arrangement for analysis by PIGE*

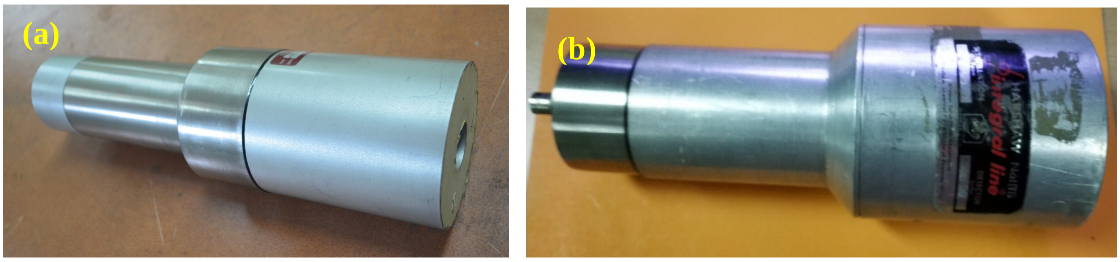

Fig 2.21: *Photographs of (a) BGO (bismuth germanate) and (b) NaI(Tl) scintillator detectors*

The charged particle detector (**Fig.2.22**) was mounted inside the scattering chamber and can be placed at any angle between 0° to 180° with respect to the beam direction through an external drive without breaking the vacuum.

Fig 2.22: *A photograph of PIPS detector*

Spectroscopic amplifier (C.A.E.N.; Mod N968) was used for the amplification of the pulses and the data was acquired by a 8K multichannel analyser. The energy calibration of the γ-ray spectra, in low energy region was performed using a set of radiation standards that included ^{133}Ba (E_γ = 356 keV), ^{137}Cs (E_γ = 661.7 keV), ^{60}Cs (E_γ = 1332.5 keV) and natural radioactivity, for example ^{40}K (E_γ =1460.8 keV) and ^{208}Tl (E_γ = 2614.5 keV) while in high energy region, nuclear reactions namely ^{15}N(p,αγ)^{12}C (E_γ = 4.44 MeV) and ^{19}F(p,αγ)^{16}O (E_γ = 6.13 MeV).

2.7 Qualitative and quantitative analysis: some important considerations

As the main objective of the investigations is to develop methodologies for the analysis of materials composed of low Z elements, the methods developed for quantification are described in the succeeding chapters. The standard methods of quantification are also presented therein for the sake of better continuity. Though the fundamental equations describing the relationship between the signal intensity and the content of an analyte in a material has been described at few places, for example in **Chapter 6,** comparator method was always used for quantification.

To find out the depth profile of an element by a resonance reaction experiments to be conducted at suitable energy intervals beyond the resonance energy **[79, 80]**. Resonances in nuclear reactions are the most effective means of depth profiling an element or an isotope in a material. The detection sensitivity and the depth resolution of the measurements are governed by the cross-section and the width of the resonance respectively while the probing depth, yet another important aspect of the depth profiling, is governed by the presence of other resonance(s) in the excitation function. Literature is replete with instances wherein the resonances in nuclear reactions have been employed for depth profiling elements, in particular those with low atomic numbers, in matrices finding applications in different fields. This exercise can be summarily portrayed by the following **Fig 2.23**.

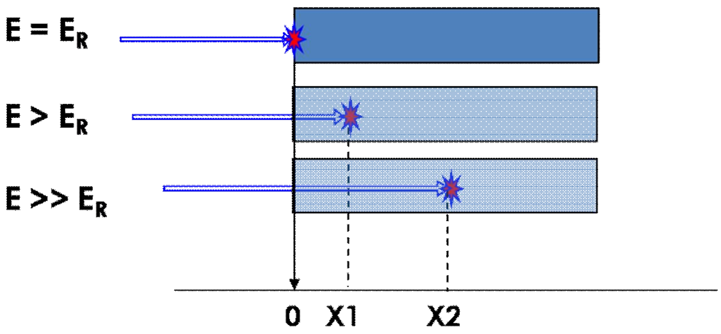

***Fig 2.23**: Schematic of depth profiling*

The depth scale is obtained can be using the following relationship

$$x = \frac{E - E_R}{S(E)} \qquad (2.24)$$

where E_R is the resonance energy. It require to experiments to be conducted at suitable energy intervals beyond the resonance energy.

Similar approach is employed for the construction of depth scale by non-resonant reactions. However it is slightly complicated as one need to take the energy loss of the projectile as well as that of ejectile into consideration for calculation. These aspects are described in the relevant chapters. As mentioned earlier, the depth resolution depends on the width of the resonance: lower width implies better depth resolution. Moreover, the depth resolution is higher for resonances occurring at lower beam energy because stopping power is lower at higher beam energies. For nuclear reactions involving the detection of charged particle, the resolution of the detector is also a dominant factor in defining the depth resolution. In the case of analysis by backscattering spectrometry, the elemental composition and also the thickness can be calculated by SIMNRA, a powerful and popular code for simulating backscattering events.

2.7.1 Radiation (γ-ray) background

A consideration of γ-ray background is necessary for spectral analysis and also for the measurement of the sensitivity of a reaction. The two sources of γ- ray background are: (a) natural radioactivity and (b) beam induced activity. Natural radioactivity that contribute to the background consist of radiation for ^{40}K and 4n and (4n+2) radioactive series present in the ambience of accelerator hall. The high resolution spectrum in **Fig 2.24** shows the γ-ray background due to natural radioactivity **[110]**.

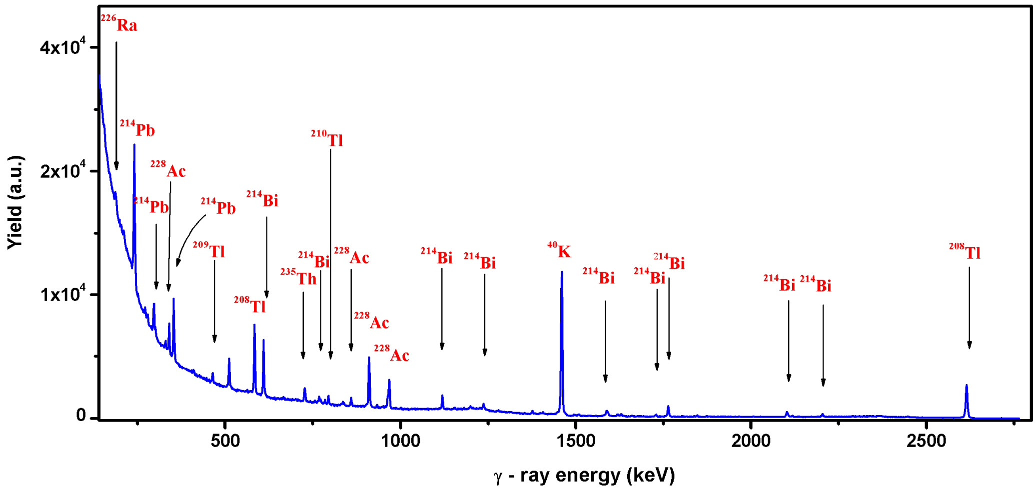

Fig 2.24: *The γ-ray background due to natural radioactivity aquired by HPGe*

So far the beam induced activity is concerned, it mainly arises from the constituents of the structural materials and the collimator material. Though it is not possible to completely eliminate the beam induced background, it can be appreciably reduced by a proper design and beam steering and focussing parameters.

Chapter 3

Depth Profiling of Li in the Electrodes of Lithium Ion Batteries

3.1 Introduction

Lithium ion battery (LIB) is one of the most widely used portable energy storage devices **[111,112]**. It is a kind of electrochemical cell. In a typical configuration, graphite is used as an anode, lithium cobalt oxide ($LiCoO_2$) as a cathode and lithium hexafluorophosphate ($LiPF_6$) as an electrolyte in a LIB. Lithium manganese oxide ($LiMn_2O_4$) and lithium ironphosphate ($LiFePO_4$) are other common cathode materials **[113].** As described in **Chapter 1** the working of LIB involves the transport of Li ions from cathode to anode during charging and back again to cathode from anode during discharging **[28]**. Li forms intercalated compound namely, C_6Li with graphite. Apparently the content of residual Li in anode or corresponding deficiency of Li in cathode is of immense significance. Also, the capacity of LIB has been found to be closely related to solid electrolyte interphase (SEI) existing at the boundary of the anode and electrolyte. Hence it is essential to determine the concentration of Li in both cathode and anode as a function of depth from their respective surfaces. Depth profiling Li is challenging and has more often been accomplished by NDP **[31,32]**. NDP of Li is based on $^6Li(n,\alpha)^3H$ reaction (Q= 4.78 MeV) and involves the detection and energy analysis of ^4He and or ^3H particles whose energies at the point of interaction are 2055 and 2727 keV respectively **[90].** The methodology, contrary to mass spectrometry methods, is non-destructive, has a detection limit of about 9.0×10^{12} at./cm^2 and is endowed with good depth resolution (≤200 nm) and high (15-30 μm) probing depth capabilities **[90]**. By virtue of these features the method has been utilized to probe real time in-situ transport of Li in Li-ion batteries **[114-117]**. As a result, NDP is the choice of technique for depth profiling lithium in this important energy device. The method, however, has two major limitations. Firstly, it is selective to ^6Li isotope that has only 7.5 % natural abundance and secondly, it requires a beam of cold or thermal neutrons of $>10^8$ n/cm^2/s flux as probe and, therefore, the measurements can be conducted only at a research nuclear reactor facility.

Lithium in materials can also be determined non-destructively by ion beam analysis (IBA) techniques. A glimpse of the capabilities of IBA techniques in addressing the different requirements in Li determination can be obtained from a review article by Raisanen published in early nineties **[118]**. Briefly, proton induced γ-ray emission (PIGE) employing ^{7}Li(p,p′γ)^{7}Li (E_{γ}=478 keV) reaction can be utilised for determining bulk Li while proton elastic backscattering spectrometry (p-EBS) is useful for the compositional analysis of Li-bearing films. Similarly, (a) nuclear reaction analysis (NRA) involving ^{7}Li(p,α)^{4}He reaction and (b) PIGE involving ^{7}Li(p,γ)^{8}Be, a proton capture reaction that displays a resonance at E_p= 441 keV, are recommended for depth profiling lithium. However, the application of these techniques, in general, and ^{7}Li(p,α)^{4}He and ^{7}Li(p,γ)^{8}Be reactions, in particular, in analysing materials used in LIB has been rather meagre. In fact, the two reactions have seldom been used for depth profiling Li even in other materials since the initial studies reported in references **[119-123]**. The recent study by Gonzalez-Arrabal et al. on depth profiling Li by ^{7}Li(p,α)^{4}He nuclear reaction in the $LiFePO_4$ cathode of a commercial LIB is probably the only instance of the application of an IBA method for such an analysis **[124]**. However, as a major limitation, the authors reported extensive interference from F existing in the cathode material that made an unambiguous determination of Li, difficult. The source of F was polyvinylidene fluoride (PVDF), used as a binding agent in the fabrication of $LiFePO_4$ based electrodes while the interference arose from ^{19}F(p,α)^{16}O reaction occurring simultaneously with ^{7}Li(p,α)^{4}He reaction.

As mentioned in **Chapter 2, section 2.7**, depth profiling of an element or an isotope by resonances in nuclear reactions **[79,80]** is the most effective method. A resonance reaction has not been hitherto utilised for depth profiling Li in LIB-specific materials. It prompted us to undertake the present work that aims at investigating the efficacy of ^{7}Li(p,γ)^{8}Be resonance reaction in depth profiling Li in the electrode materials commonly used in a LIB. The work encompassed a comprehensive evaluation of the analytical capabilities of the reaction prior to its application to the battery materials. A study on the capabilities of the reaction was necessitated due to the lack of any comprehensive treatment of the reaction in the previous reports. It is shown, by way of the analysis of the anode (graphite) and the cathode ($LiCoO_2$) of a commercial LIB, that the reaction can facilitate interference-free profiling of Li up to a depth of ~20 µm with a sensitivity and depth resolution of ~0.2 at.% and ~150 nm respectively. A part of the work reported herein is devoted to the depth profile measurements by $^7Li(p,\alpha)^4He$ reaction as well. Herein we show that, the interference from F can be circumvented, at least, up to a depth of about 5-8 µm through a proper selection of experimental parameters, namely the beam energy and the angle of detection. The method, as a result, too can provide reliable depth profiles of Li up to sizable depths.

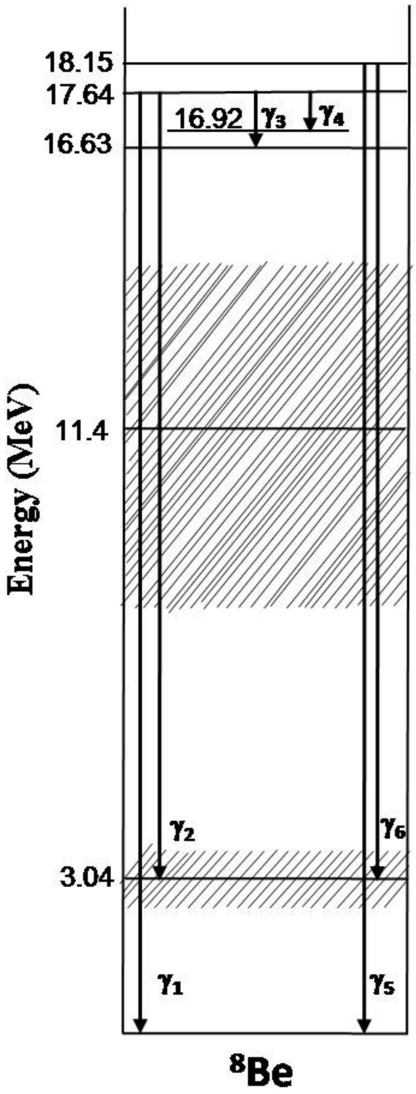

***Fig.3.1**: A schematic of energy levels of ^{8}Be nucleus and nuclear transitions leading to the emission of γ-rays (γ_1 = 17.6 MeV, γ_2 = 14.6 MeV, γ_3 = 1.0 MeV, γ_4 = 0.72 MeV, γ_5 = 18.15 MeV and γ_6 = 15.1 MeV)*

3.2 Depth profiling of Li by PIGE: $^7Li(p,\gamma)^8Be$ proton capture reaction

3.2.1 Energetics and energy level scheme of ^8Be

The $^7Li(p,\gamma)^8Be$ proton capture reaction is exoergic and is characterised by a Q-value of 17.2543 MeV. **Fig.3.1** shows the energy level diagram of the ^8Be nucleus and transitions leading to the emission of γ-rays of different energies **[125]**. 17.64 MeV (γ_1) and 14.6 MeV (γ_2) γ-rays are emitted as a result of transitions from the excited state at E_x= 17.64 MeV to the ground and the first excited states of the nucleus respectively.

In addition to the high energy γ-rays, 1.0 MeV (γ_3) and 0.72 MeV (γ_4) γ-rays are also emitted following transitions from the excited state at E_x = 17.64 MeV to the states with E_x = 16.63 MeV and E_x = 16.92 MeV respectively. Resonance occurs at E_p= 441 keV for both γ_1 and γ_2 -rays. The first excited state has a width of about 1.5 MeV and therefore 14.6 MeV γ-rays (i.e. γ_2) are very broad. Notably, the first excited state and the second excited state (which, incidentally, has a width of 3.5 MeV) decay by way of α-emission. The width of the state at E_x = 17.64 MeV is about 11 keV and thus the resonance is expected to have a comparable width. The resonance, as a result, is suitable for depth profile measurements. It is important to note that in addition to the resonance at E_p = 441 keV, another resonance occurs at E_p = 1.03 MeV for the excited state with E_x = 18.15 MeV and width of about 138 keV. The resonance is observed for 18.15 (γ_5) and 15.1 MeV (γ_6) γ-rays that are emitted as a result of the transitions from E_x =18.15 MeV to the ground and the first excited states respectively.

The resonance has a large width and therefore is not suitable for depth profile measurements. On the contrary, it can limit the probing depth of the resonance at E_p = 441 keV.

3.2.2 Experimental details

3.2.2.1 Materials for analysis

Compacted discs of pure lithium carbonate (Li_2CO_3), those containing Li_2CO_3 and graphite powder, thin films of lithium fluoride (LiF) and lithium cobalt oxide ($LiCoO_2$), and thick coatings of graphite and $LiCoO_2$ were used as the targets. The source and the preparation of materials have been described in **Chapter2, Section 2.2.**

3.2.2.2 Proton beam irradiation

The irradiation of the samples (targets) and the measurement of the emitted radiations are described in detail in **Chapter 2, Section 2.6**. Briefly, the samples were bombarded with energetic and a well-collimated proton beam (Φ~2mm) in 390 – 1800 keV region at normal incidence in a scattering chamber maintained at 1×10^{-5} torr vacuum. For depth profile experiments the incident beam energy was successively increased in steps of 2 keV in the vicinity of resonance energy (i.e, 441 keV) and in steps of 30-40 keV above it. The beam current during irradiation was ≤30 nA.

3.2.2.3 Acquisition of γ-ray spectrum

The prompt γ-rays emitted from ^{7}Li(p,γ)^{8}Be reaction were detected by NaI(Tl) and HPGe detectors. The details of the features of the detector and the experimental geometries and the electronics of the data acquisition system are described in detail in **Chapter 2, Section 2.6**. The γ-ray spectra were recorded at each proton energy for a charge of 5-10 μC to obtain peaks with statistically significant counts.

3.2.3 γ-ray spectra / spectral features

Fig.3.2(a) shows a typical γ-ray spectrum acquired by the NaI(Tl) detector on irradiating the disc of Li_2CO_3 with 500 keV protons. The spectrum consists of two broad structures that correspond to 17.6 and 14.6 MeV γ-rays emitted from ^{7}Li(p,γ)^{8}Be reaction. The 14.6 MeV peak, in accordance with the decay scheme of ^{8}Be nucleus represented in **Fig.3.1**, has comparatively larger width. The structures are composed of 17.6 or 14.6 MeV full energy peak and the corresponding single and double escape peaks. This is illustrated for 17.6 MeV γ-rays by the spectrum acquired by HPGe (**Fig. 3.2**(a′)) wherein the three kinds of peaks are conspicuously seen. These components, however, are not discernible for 14.6 MeV peak due to its larger width and higher Compton background of 17.6 MeV γ-rays.

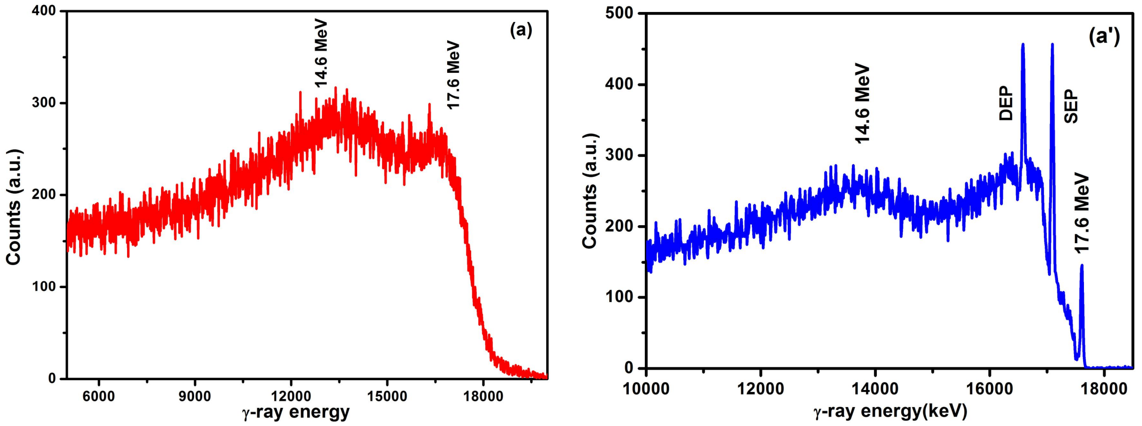

***Fig.3.2**: Prompt γ-ray spectra of a disc of Li_2CO_3 recorded with (a) a NaI(Tl) detector and (a') a HPGe detector on irradiating with 500 keV protons.(SEP : single escape peak ; DEP : double escape peak)*

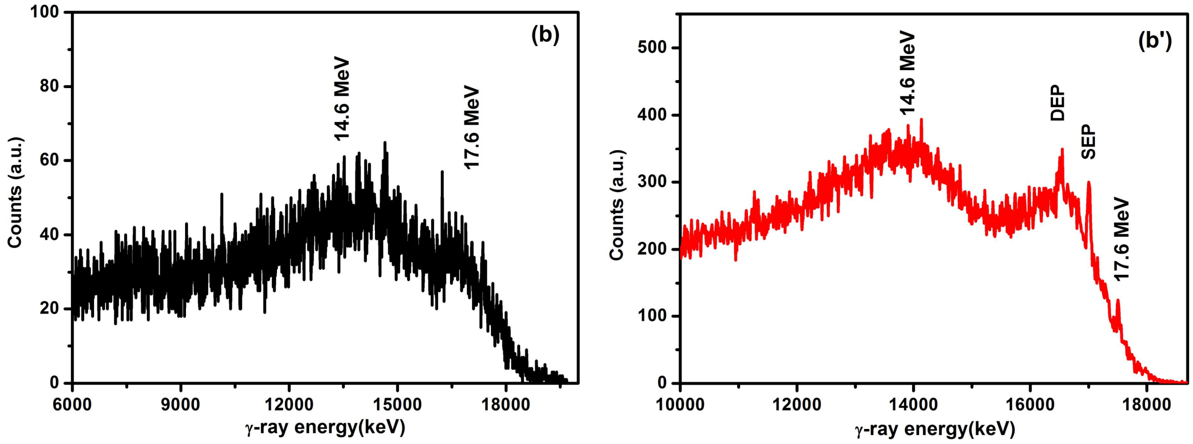

***Fig.3.3**: Prompt γ-ray spectra of a disc of Li_2CO_3 recorded with (b) a NaI(Tl) detector and (b') a HPGe detector on irradiating with 1200 keV protons.(SEP : single escape peak ; DEP : double escape peak)*

Notably, the irradiation of the target with 1030 keV or higher energy protons produced γ-ray spectrum nearly identical to that recorded at E_p = 500 keV with, contrary to the postulations in reference **[125]**, no discernible presence of 18.15 and or 15.1 MeV γ-rays. The NaI (Tl) and HPGe spectra of the target acquired at E_p= 1200 keV is shown in **Fig. 3.3** for illustration.

3.2.4 Yield curve and identification of resonances

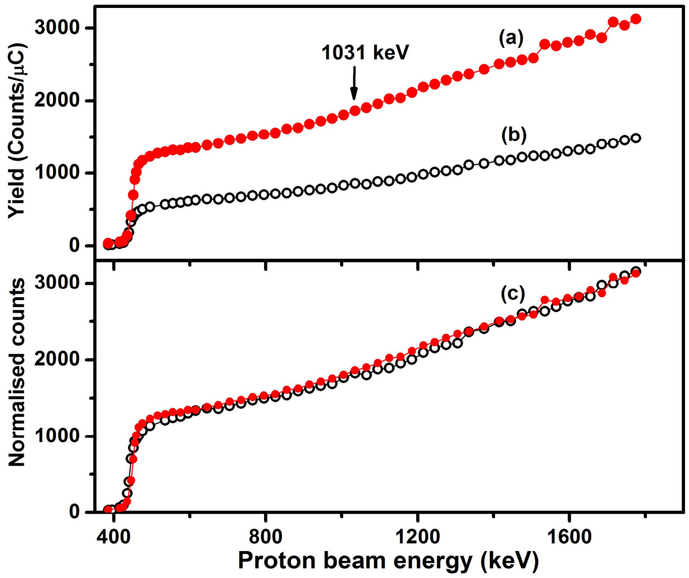

***Fig. 3.4**: Charge-normalised thick target γ-ray yield curves of (a) Li_2CO_3 and (b) Li_2CO_3 and graphite mixed in 1:1 weight proportions. The yield curve of Li_2CO_3 and graphite mixture (i.e. plot(b)) is converted to that of Li_2CO_3 by making appropriate corrections for Li content and stopping power. The resulting 'theoretical curve' is superimposed on the experimental curve of Li_2CO_3 (i.e. plot (a)) in plot(c)*

Fig. 3.4(a) and (b) show the charge normalised thick target yield curves of 17.6 and 14.6 MeV γ-rays in 390-1800 keV proton energy region for Li_2CO_3 and a mixture containing Li_2CO_3 and graphite in 1:1 weight proportions. The cumulative counts appearing in 10-19 MeV energy window in the γ-ray spectra recorded using the NaI(Tl) detector served as the yield of the γ-rays. To ascertain the constancy of the yields, the yield curve of the mixture (i.e; **Fig. 3.4(b)**) is converted into that of Li_2CO_3 by making appropriate corrections for Li content and stopping power. The resulting 'theoretical curve' and the experimental curve of Li_2CO_3 in **Fig. 3.4**(a) are plotted in **Fig.3.4**(c) for the sake of comparison. It is observed that the two yield curves superimpose quite well on each other in the entire proton energy region. This observation adequately validates the yield curve of lithium recorded by measuring the 17.6 and 14.6 MeV γ-rays emitted from ^{7}Li(p,γ)^{8}Be proton capture reaction.

The analysis of the yield curve showed the prevalence of a resonance at 441±1 keV. The resonance energy was measured by derivative method and is consistent with that reported in literature **[125]**. The curve also shows a continuous but gradual increase in γ-ray yields with proton energy in E_p= 465 - 1800 keV region. Importantly, the target was stable under beam irradiation. It was ascertained by the constancy of γ-ray yields on repeated measurements at particular beam energy. In some cases measurements at certain energy was carried out also after acquiring data over the entire energy range. The absence of any perceptible discontinuity in the yield curve points to the non-occurrence of any resonance in this energy region. This observation is in sharp contrast to the prevalence of a wide yet strong resonance at 1031 keV in ^{7}Li(p,γ)^{8}Be reaction which is not only suggested by the decay scheme of ^{8}Be nucleus (described in **Section 3.2.1**) but has also been experimentally observed by Golicheff et al. **[119]**. The present result, therefore, is highly significant. Though a precise explanation is lacking at the moment, a significant anisotropy in the distribution of 18.15 MeV γ-rays may be one of the plausible reasons for the non-occurrence of the resonance. It must be pointed out that γ-rays in reference **[119]** were measured at 90° angle as against 0° angle in the present study.

3.2.5 Interferences

Detection sensitivity is an important feature of an analytical methodology. It depends on reaction cross-section and, in turn, on the thick target yield of γ-rays in the present context and interferences arising from the elements constituting the matrix. The spectral interferences can arise from reactions giving rise to high energy γ-rays. Since the objective of the investigations is to establish a methodology for depth profiling Li in lithium ion batteries (LIB), the interferences that can arise from the elements constituting anode and / or cathode materials were investigated in detail. Graphite is used as an anode in a LIB while copper, as a current collector. Carbon predominantly undergoes ^{12}C(p, γ)^{13}N and ^{13}C(p, γ)^{14}N nuclear reactions with 390–1800 keV protons that emit 2.36 MeV and 2.4-8.6 MeV γ-rays respectively. Apparently, the energies of these γ-rays are too low to cause any interference in the measurements of 17.64 MeV and 14.6 MeV γ-rays from $^{7}Li(p,\gamma)^{8}Be$ reaction. The possibility of interferences from pile up is also unlikely due to low cross-sections of these reactions. This is well illustrated by the γ-ray spectrum (**Fig. 3.5**) recorded for a thick graphite disc on irradiating with 1800 keV proton beam. The detection limits of Li in graphite at E_p = 1200, 1600 and 1800 keV are estimated to be about 0.2, 0.26 and 0.35 at.% respectively. These estimations are based on 3 σ (σ = standard deviation) value of the cumulative counts in 10-19 MeV γ-ray energy region in the spectra of graphite at the respective beam energies.

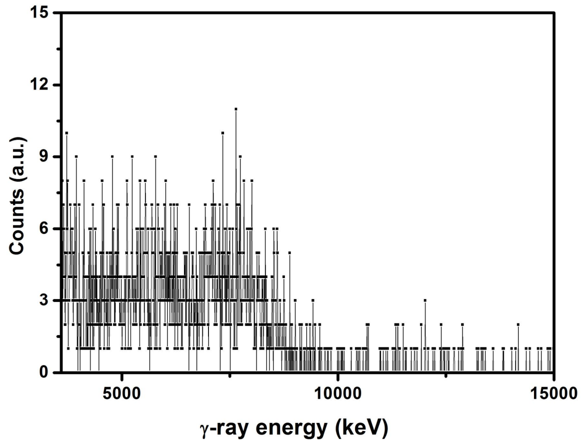

***Fig.3.5**: Prompt γ-ray spectrum of a graphite disc acquired by NaI(Tl) detector on irradiating with 1800 keV protons.*

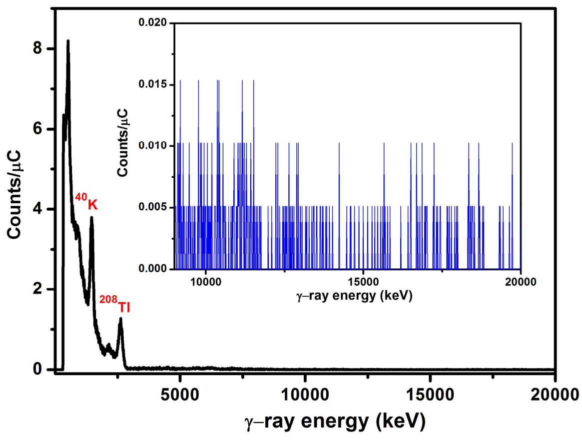

***Fig.3.6**: Prompt γ-ray spectrum of a copper sheet acquired by NaI(Tl) detector on irradiating with 1800 keV protons.*

In order to ascertain the possible spectral interference from Cu (i.e; current collector), a thick sheet of copper metal was irradiated with 1200 keV protons. The spectrum of the emitted γ-rays is presented in **Fig.3.6** with the inset showing the spectrum in 10-20 MeV energy region for better illustration. It can be observed that there is no serious spectral interference from Cu with the γ-rays integrated in 10-20MeV region corresponding to

0.02 at% of lithium. In other words, the limit of detection of Li in graphite is 10 times better than in copper.

The cathode of a LIB, on the other hand, generally consists of lithium cobalt oxide ($LiCoO_2$), lithium manganese oxide ($LiMn_2O_4$) or lithium ironphosphate ($LiFePO_4$). Herein, no interference is anticipated from oxygen and metallic (transition elements) constituents, since protons with $E_p \leq$ 1800 keV do not induce any high-energy γ-ray emitting nuclear reaction in these elements. It is important to note that due to the lack of cohesion the electrode materials are seldom used in their pure states in the fabrication of devices. These are, in fact, mixed with compounds like polyvinylidene fluoride (PVDF) which not only function as a binder but also facilitate good contact between the active materials and the current collector (i.e; aluminium).

Table 3.1*: Resonances for 6-7 MeV γ-rays in* $^{19}F(p, \alpha\gamma)^{16}O$ *nuclear reaction*

E_p (keV)	Γ(keV)	σ (mb)
224.4	1	0.2
340.5	3.3	160
483.6	0.9	32
596.8	30	7.1
671.6	6	57
834.8	6.5	19
874	5	540
902.3	5.1	23
935.1	8.6	180
1090	0.7	13
1123	22	-
1140	2.5	15
1189	110	19
1283	18.6	29
1348	5.6	89
1375	11	300
1607	6	-
1694	35	-
1949	40	-

Fluorine undergoes $^{19}F(p, \alpha\gamma)^{16}O$ nuclear reaction emitting 6.1, 6.9 and 7.1 MeV γ-rays **[126].** The reaction is highly prolific. As is evident from **Table 3.1** it has several strong resonances and therefore enables the sensitive determination of fluorine. In order to ascertain the extent of interferences, a 500nm film of LaF_3 on Si was examined at 875 keV incident energy. The relevant γ-ray spectrum recorded with NaI (Tl) detector is presented in **Fig.3.7**. An examination of the high energy (7-17MeV) portion of the spectrum in the inset of the figure clearly shows the prevalence of significant counts in the energy window of our interest. This is suggestive of the occurrence of a spectral interference from F present in PVDF. The detection limit of Li in a typical F bearing matrix is about 0.7 at.% at a proton incident energy of 900keV. So far as the interferences from $^{27}Al(p,\gamma)^{28}Si$ reaction is concerned, it is highly significant as represented by the γ-ray spectrum recorded on bombarding a thick sheet of Al with 1800 keV protons. The relevant spectrum is shown in **Fig.3.8**.

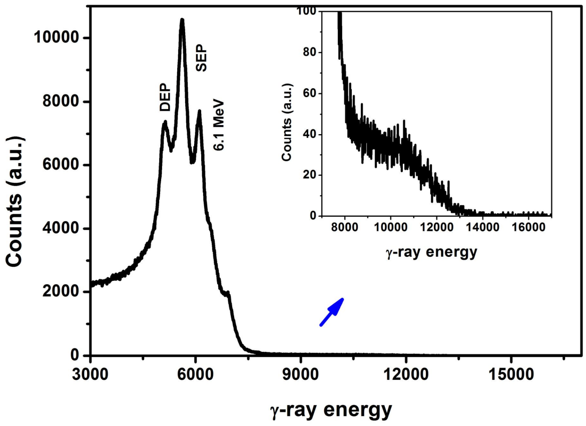

Fig.3.7: *Prompt γ-ray spectrum of thin film of* LaF_3 *acquired with NaI(Tl) detector on irradiating with 875 keV protons*

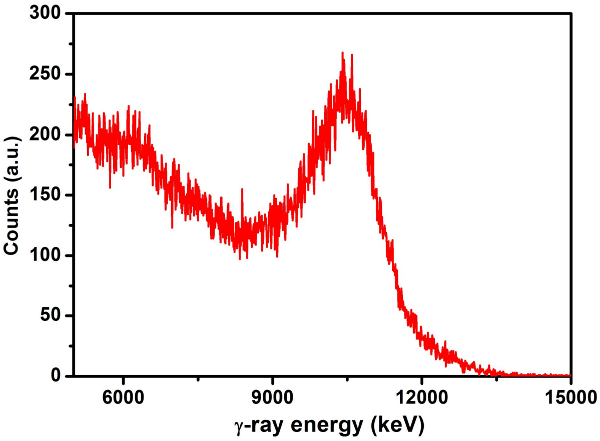

Fig.3.8: *Prompt γ-ray spectrum of a aluminium sheet acquired by NaI(Tl) detector on irradiating with 1800 keV protons. The high energy γ-rays are produced as a result of* $^{27}Al(p,\gamma)^{28}Si$ *reaction.*

3.2.6 Methodology of depth profiling by PIGE

The depth profile of Li in a material by PIGE was obtained from its yield curve which represents the yields of the characteristic γ-rays as a function of incident proton energy. The yield at the proton energy at the *i* th step, E_i, is a measure of the content of Li at a depth represented by energy E_i. The content of Li was calculated by comparator method by means of the following formula with the compacted disc of Li_2CO_3 serving as a standard:

$$(x_{Li})_{samp} = \frac{(Y)_{samp} \times (x_{Li})_{std} \times \varepsilon_{samp}}{(Y)_{std} \times \varepsilon_{std}} \tag{3.1}$$

where the subscripts 'samp' and 'std' refer to the sample and the standard respectively, x_{Li} is the atomic fraction of Li, Y_{samp} is the charge normalized yield (counts/μC) of γ-rays of the sample at the proton energy E_i, Y_{std} is the charge normalized yield of γ-rays of the standard at 465 keV proton energy and ε is the stopping cross-section (eV/10^{15}at./cm^2) of the materials for 441 keV protons. Y_{samp} is, in fact, corrected for non-resonant yield (described in detail in **section 3.2.8**). It is to be noted that the compound samples were assumed to bear binary chemical composition. For example, lithium fluoride was represented as $Li_xF_{(1-x)}$, the mixture of lithium carbonate and graphite as $Li_x(CO_3)_{1-x}$ while lithium cobalt oxide as was represented as $Li_x(CoO_2)_{1-x}$. The values of ε of the elements and the compounds were calculated using SRIM **[102]** and for some of them are listed in **Table 3.2**.

Table 3.2: *Stopping cross-sections of C, Al, Fe, Li_2CO_3 and $LiFePO_4$* for 465 keV protons

Sl.No.	Element/ Compound	Stopping cross-section (eV/10^{15} at./cm^2)
1	C	7.41
2	Al	11.66
3	Fe	19.12
4	Li_2CO_3	6.92
5	$LiFePO_4$	10.23

The concentration of Li can also be calculated directly from the yield equation i.e. first principle. However, this approach was not utilized due to the lack of data on the cross-section of the resonance and the efficiency of the NaI(Tl) detector for high energy γ-rays.

The thickness (T) of a film was calculated using the formula

$$T = \frac{\Delta E}{\varepsilon} \qquad (3.2)$$

where ΔE corresponds to the width of the yield curve and ε is the stopping cross section (eV/10^{15} at./cm^2) at the proton energy corresponding to midpoint of the yield curve.

The distribution of Li at a depth D in a thick target was obtained using the following formulae

$$D_1 = \frac{(E_1 - E_R)}{\varepsilon\left[(E_1 + E_R)/2\right]} \qquad (3.3)$$

$$D_i = D_{i-1} + \frac{(M_i - E_R)}{\varepsilon\left[(M_i + E_R)/2\right]} \qquad (3.4)$$

$$M_i = E_i - D_{i-1}\varepsilon\left[(M_i + E_R)/2\right] \qquad (3.5)$$

where D_1 represents the depth at E_1, D_i depths at energies E_i for $i \geq 2$, E_R is the resonance energy (i.e. 441 keV) and ε is the sopping cross-section (eV/10^{15}at./cm^2) of the sample at the energy in the bracket. The stopping cross-section is calculated for the composition of the sample estimated at energy $E_{i.}$ The thickness or depth in linear dimension was obtained by taking the standard density of the respective compound into consideration.

3.2.7 Features of resonance: depth resolution, probing depth and detection sensitivity

Depth resolution and probing depth are the two most important aspects of a depth-profiling methodology. The depth resolution of a resonance-reaction based technique is governed by the width of the resonance, which for the 441 keV resonance of $^7Li(p,\gamma)^8Be$ reaction is about 10 keV and other factors such as uncertainty in beam energy, thermal effects etc. which contribute to the broadening of the resonance. An estimation of the contributions of the individual parameters is non-trivial and thus the depth resolution is best measured in terms of energy difference between 12% and 88% of the leading step of the yield curve. Presently, it was measured to be 19±1 keV which corresponds to a depth resolution of about 230 nm in graphite (density=2.25 gmcm^{-3}) and 155 nm in $LiCoO_2$ (density=5.03 gmcm^{-3}) in surface regions. The depth resolution deteriorates in interiors of the specimens due to energy straggling of the proton beam. So far as the probing depth is concerned, it is considerably higher due to the absence of the resonance at 1031 keV or at any other energy up to E_p= 1800 keV and is about 28 and 18 µm in graphite and $LiCoO_2$ respectively. Notably, in cases wherein the resonance at 1031 keV is observed, the probing depth of the resonance in the two matrices is expected to be only 9 and 6 µm respectively.

In addition to depth resolution and probing depth, detection sensitivity is another important feature of an analytical methodology. The probable sources of interferences are described briefly in **Section 3.2.5**. The spectra in **Fig. 3.5, 3.7 and 3.8** portray the interferences from graphite, fluorine and aluminum. In order to assess the maximum extent of interference that can occur, the spectra of graphite and Al were acquired at E_p= 1800 keV while the spectrum of F was recorded at 875 keV with thick elemental discs of graphite and Al and a 500 nm film of LaF_3 on Si serving as the targets of the respective elements. As can be seen from the absence of any appreciable counts in 10-19 MeV γ-ray energy window in the spectrum of graphite, the interference from the element is largely insignificant. In contrast to graphite, the spectra of F and Al contain substantial counts up to 13.4 MeV, much beyond their respective highest (i.e. 7.1 and 11 MeV) energy γ-rays. The counts appearing in the high energy region are apparently the manifestations of pile up and can cause serious errors in the determination of Li. The interference, however, can be circumvented by integrating yields in 13.5 to 19 MeV energy region instead of 10 to 19 MeV region as is the case with graphite or other matrices not producing γ-rays in this window. As an alternative, the contribution of pile up can be evaluated using the approach described by Molodstov and Gurbich **[127]**. The detection limit of Li in a typical fluorine bearing matrix at about E_p= 900 keV is 0.70 at.% while in Al at E_p= 1200 and 1800 keV, it is about 0.25 at.% and 0.50 at.% respectively. So far as thin films are concerned, interferences from the substrate can have a profound influence on the detection sensitivity. However, in the event of the absence of any interference, the detection sensitivity for films of thicknesses comparable to the system resolution is expected to be identical to that estimated for thick targets.

3.2.8 Off-resonance cross-section: correction in yield

Apart from showing the absence of the resonance at E_p=1031 keV, another notable feature of the yield curve in **Fig. 3.4(**a) is an ever increasing yield of γ-rays throughout the proton energy range. In other words, the curve is devoid of a plateau of constant height which ideally holds true for a thick target yield curve of a reaction consisting of an isolated resonance in its excitation function. The constantly increasing yield is attributable to the off-resonance cross-section of the reaction. It implies that the yield at an incident energy E has contributions from two sources: (a) ^{7}Li(p,γ)^{8}Be resonance reaction at a depth 'D_i' where the resonance occurs and (b) ^{7}Li(p,γ)^{8}Be reaction occurring in regions preceding depth 'D_{i-1}' with off-resonance cross-sections. Apparently, corrections for the "off-resonance yields" are required for an unambiguous and precise depth profiling of lithium. The determination of off-resonance cross-section at different incident beam energies is difficult. However, a satisfactory estimation of the off-resonance yields can be accomplished from a thick target yield curve recorded at a constant proton energy interval, ΔE, for example, the curve in **Fig.3.4**(a). The percentage contribution of the off-resonance yield at an energy E > 465 keV relative to the E_i can be obtained from the equation

$$Y(E)_{off-resonance} = \frac{Y(E) - Y(E-\Delta E)}{Y(E_i)} \times 100 \qquad (3.6)$$

where $Y(E_i)$ corresponds to yield at E_p = 465 keV i.e. the proton energy at which the saturation of γ-ray yields is first realised.

3.2.9 Analysis of samples

The applicability of this methodology in depth profiling Li was examined by analysing several specimens that included thin films of lithium fluoride and lithium cobalt oxide, a mixture containing Li_2CO_3 and graphite powders in 1:1 weight proportions, and thick coatings of films of $LiCoO_2$ and graphite on Al and Cu substrates respectively. The films of lithium fluoride and lithium cobalt oxide were deposited by physical vapour deposition methods while the thick coatings of anode and cathode, as described earlier, belonged to a LIB. The former two films were also examined by proton-elastic backscattering spectrometry (p-EBS) for the sake of validation. **Fig. 3.9** shows the p-EBS spectra of the two films acquired at E_p= 2.09 and 2.4 MeV energies respectively. The average content of Li in the films and their respective thicknesses obtained by depth profiling by $^7Li(p,\gamma)^8Be$ resonance reaction and the quantitative results obtained by p-EBS are listed in **Table 3.3**. Notably, the atomic compositions of the films by p-EBS were determined by simulating the spectra by SIMNRA **[103]**. The scattering cross-sections of Li and F reported recently by Paneta et al. and those of Si reported by Rauhala et al. **[77,128,129]** were used in the simulations. The yield curve of the thin lithium fluoride film is shown in **Fig.3.10** for comparison. A good resemblance in the values obtained by the two approaches is indicative of the robustness of the depth profiling methodology. It is worthwhile mentioning that since the films are thin and proton lose 25-50 keV energy while traversing them, corrections for off-resonance yields described earlier were not employed during quantification.

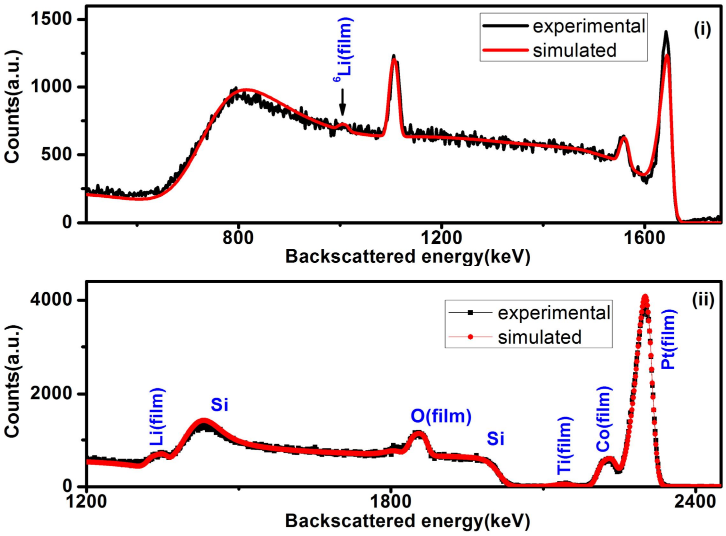

Fig.3.9*: Proton elastic backscattering spectra of thin films of (i) LiF and (ii) $LiCoO_2$ / Pt/ TiO_2/Si acquired on irradiating with 2.09 and 2.4 MeV protons respectively. The solid curve overlapped on spectra represent the simulated curve.*

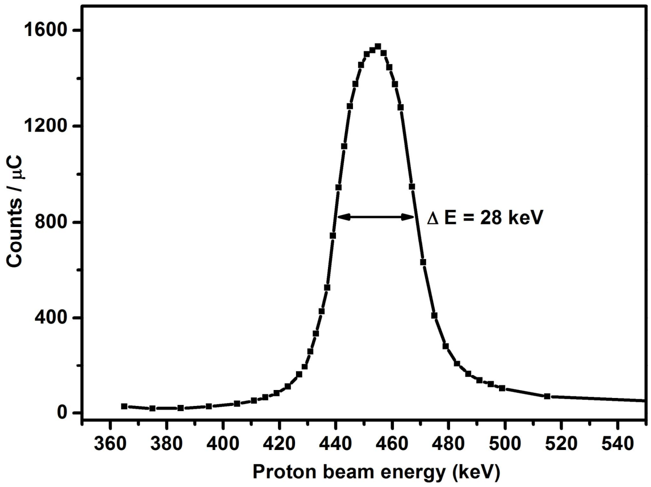

Fig.3.10*: Yield curve of thin lithium fluoride film constructed using $^7Li(p,\gamma)^8Be$ resonance reaction.*

Table 3.3: *Composition and thickness of thin films of lithium fluoride and lithium cobalt oxide determined by p-EBS and PIGE*

	Lithium fluoride				Lithium cobalt oxide				
	Composition (at.%)		Thickness		Composition (at.%)			Thickness	
	Li	F	10^{18} at./cm^2	nm	Li	Co	O	10^{18} at./cm^2	nm
p-EBS	55	45	4.14	338	26.4	25.5	48.1	4.9	396
PIGE	51	49	4.03	329	26.5	24.5	49.0	5.3	435

However, before embarking on the analysis of thick coatings of anode and cathode of the LIB, the mixture containing Li_2CO_3 and graphite powders in 1:1 weight proportions was analysed by taking the proposed method for the correction of off-resonance yields into consideration. **Fig. 3.4**(b) shows the charge normalised thick target yield curve of the sample. The average content of Li in the mixture was estimated to be ~ 15.8 at. % which is in good agreement with its theoretical content (16.45 at.%). Furthermore, the element is distributed uniformly up to ~ 25 μm - the probing depth achievable in the mixture under the present experimental conditions. As an exercise to cross-validate the results, the yield curve of the mixture was converted into that of Li_2CO_3 by making appropriate corrections for the content of Li and stopping cross-sections. The resulting curve, as can be seen from **Fig.3.4**(c), agrees very well with the experimental yield curve of Li_2CO_3. These data not only corroborate and lend credence to the previous findings on the absence of the resonance at 1031 keV and the trend on the variation of γ-ray-yields with proton energy but also signify the efficacy of the methodology for depth profiling lithium up to a depth of about 25 μm in materials.

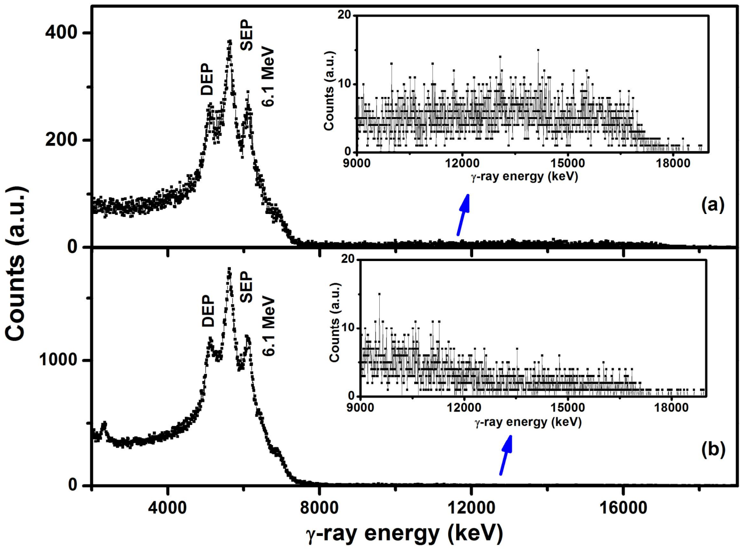

***Fig. 3.11**: NaI(Tl) γ-ray spectra of thick coatings of (a) lithium cobalt oxide and (b) graphite acquired at 895 keV proton energy. 6.1 MeV γ-rays are emitted from $^{19}F(p, \alpha\gamma)^{16}O$ reaction. SEP and DEP represent the single and double escape peaks (corresponding to the full energy peak i.e. 6.1 MeV) respectively.*

The γ-ray spectra of the coatings of anode and cathode of the LIB acquired at E_p = 895 keV are shown in **Fig.3.11**. Similar to the compacted disc of $CaCO_3$, the coatings were also found to be stable against proton beam irradiation. The occurrence of strong peaks of 6.1 MeV γ-rays from $^{19}F(p,\alpha\gamma)^{16}O$ nuclear reaction and the associated single and double escape peaks in the spectra confirm the presence of fluorine, albeit in different proportions, in the two coatings. The spectra in **Fig.3.11** form a part of spectra recoded to depth profile F in the coatings by the resonance at 872 keV of $^{19}F(p, \alpha\gamma)^{16}O$ nuclear reaction. The coatings were also analyzed by $^{19}F(p,p'\gamma)^{19}F$ (E_γ =197 keV) to determine the net content of fluorine. These measurements suggested that the coating of cathode contained about 3 wt.% and that of anode slightly less, PVDF. The content of PVDF was taken into account during quantification. In view of the presence of F, the concentration of Li in these specimens were obtained by integrating γ-ray yields in 13.5-19 MeV energy window. At this stage it is pertinent to mention that except for the differences in absolute counts, no perceptible disparity was observed in the yield curves of Li_2CO_3 (or 50% Li_2CO_3 + 50 % graphite) constructed by integrating counts in 10.0-19.0 MeV and 13.5-19.0 MeV regions. As can be observed from the depth profile data in **Fig.3.12**(a), the coating of anode is deficient in Li in surface regions while its interior contains the element in the nominal chemical composition of $LiCoO_2$. Importantly, the distribution of Li in the interiors of the coating is homogeneous. The prevalence of $LiCoO_2$ as the major constituent of the coating was also substantiated by X-ray diffraction (***Fig. 3.13)***.

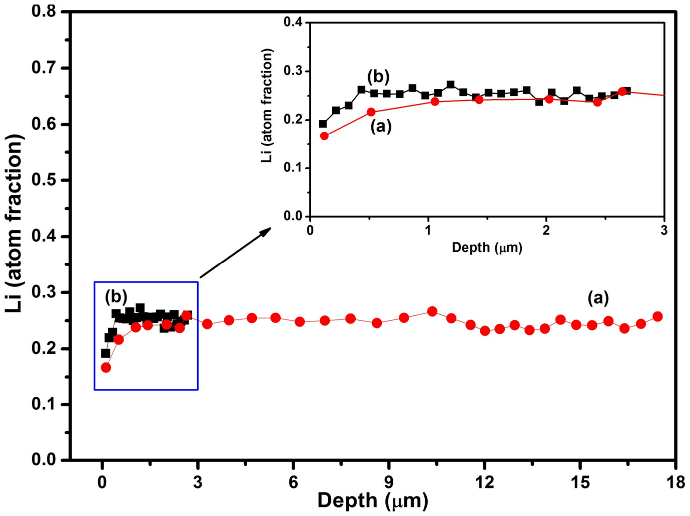

Fig.3.12: Depth profile of Li in the thick coatings of lithium cobalt oxide obtained by (a) $^{7}Li(p,\gamma)^{8}Be$ reaction and (b) $^{7}Li(p,\alpha)^{4}He$ reaction.

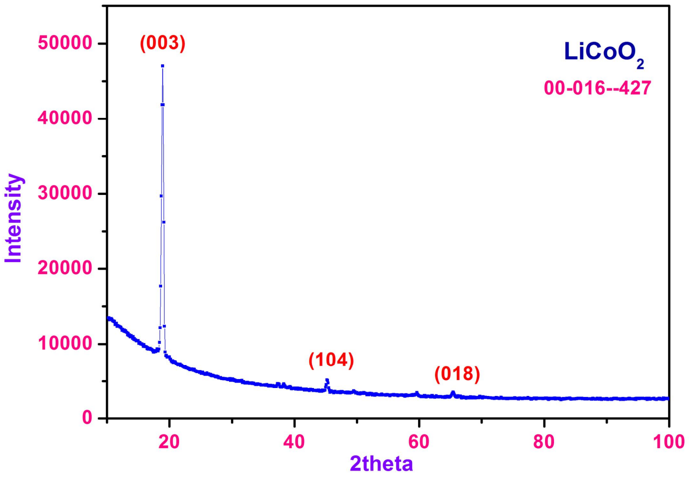

Fig. 3.13: XRD pattern of cathode material of LIB

So far as the coating of cathode (graphite) is concerned, the surface is enriched in Li but its content decreases rapidly with depth (**Fig.3.14 (a)**). The opposite distribution of Li in the surface regions of the anode and cathode probably reflects the incipient stages of lithiation and de-lithiation of the respective electrodes though the presence of Li at the surfaces of anode due to contamination from cathode cannot be completely ruled out. The combined uncertainty in the determination of Li in thin targets is about 6% which has contributions from yield measurement (1%), charge integration (2%) and stopping cross-section (4%) for the sample as well the standard. In the case of thick targets, the combined uncertainty is marginally higher due to the contribution (3%) from uncertainty associated with the subtraction of off-resonance yields. The uncertainty in depth scale is about 5 % which has contribution from the uncertainties related to stopping cross-sections (3-4%) and mean energy approximation (3-4%) used in **equations (3.3)-(3.5)**.

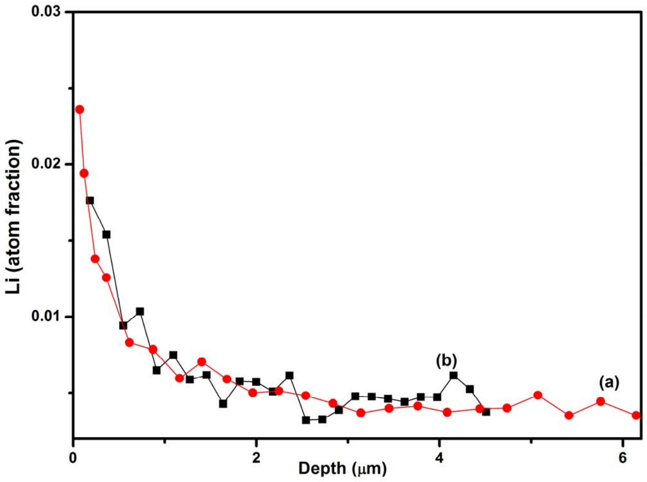

***Fig.3.14**: Depth profile of Li in the thick coatings of graphite obtained by (a) $^{7}Li(p,\gamma)^{8}Be$ reaction and (b) $^{7}Li(p,\alpha)^{4}He$ reaction.*

3.3 Depth profiling of Li by NRA: $^{7}Li(p,\alpha)^{4}He$ nuclear reaction

In addition to the PIGE method described in (**Section 3.2**), a nuclear reaction analysis method involving particle-particle interaction was also developed for depth profiling Li in materials, in particular the electrode material of LIB. This is a simple method and competes with the PIGE as well as NDP in Li depth profiling capabilities. The method involves $^{7}Li(p,\alpha)^{4}He$ nuclear reaction and is based on the detection of α-particles. The salient features of the reaction and the development of the methodology are described in the following sub-sections.

3.3.1 Kinetics and energetics

The $^{7}Li(p,\alpha)^{4}He$ reaction (pictorially represented in **Fig.3.15**) is characterised by a Q value of 17.3462 MeV **[125]**. The higher Q value of this reaction as compared to that of $^{7}Li(p,\gamma)^{8}Be$ reaction is ascribable to the Q-value (0.9189 MeV) of $^{8}Be \rightarrow 2\ ^{4}He$ reaction.

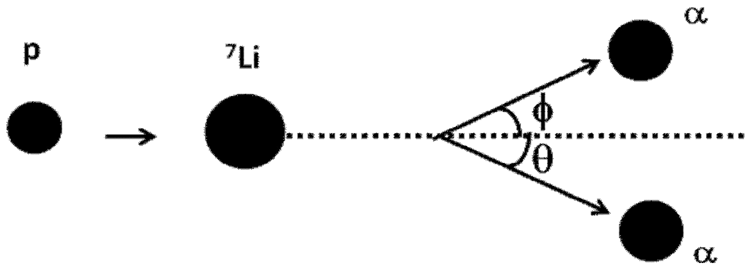

***Fig.3.15**: Schematic of $^7Li(p,\alpha)^4He$ nuclear reaction*

The depth profiles of lithium can be directly deduced from the spectrum of α-particles. The cross-section of the reaction and the energy of the emitted α-particles depend on the incident proton energy and also on the angle of emission. The cross-section of the reaction has been reported in wide energy range at several detection angles while the energy of the α-particles at any incident proton energy and angle of emission can be calculated by the kinematic relationship given by the following formulae **[74,128]**.

$$\sqrt{\mathrm{E}_\alpha} = V \pm \sqrt{V^2 + W} \qquad (3.7)$$

where

$$\mathrm{V} = \frac{\sqrt{\mathrm{M_p} \times \mathrm{M}_\alpha \times \mathrm{E_p}}}{2 \times \mathrm{M}_\alpha} \cos\theta \qquad (3.8)$$

$$\mathrm{W} = \frac{M_\alpha \times Q + E_p \times (M_\alpha - M_p)}{2 \times \mathrm{M}_\alpha} \qquad (3.9)$$

The energies of the α-particles (E_α) calculated for 0.55 to 3 MeV protons (E_p) at several detection angles (θ) in 60-150° range are shown in **Fig.3.16**. It is observed that at 60° and 90° angles, the reaction exhibits normal kinematics wherein dE_α/dE_p is positive. However at 150° angle, it follows inverse kinematics with E_α decreasing with increase in E_p i.e. dE_α/dE_p is negative. The transition from normal to inverse kinematics takes place around 120° angle at which $dE_\alpha/dE_p \cong 0$. The occurrence of inverse kinematics for $^7Li(p,\alpha)^4He$ reaction has not been previously observed though it is known to occur in other nuclear reactions such as $D(^3He,p)\alpha$ **[78].**

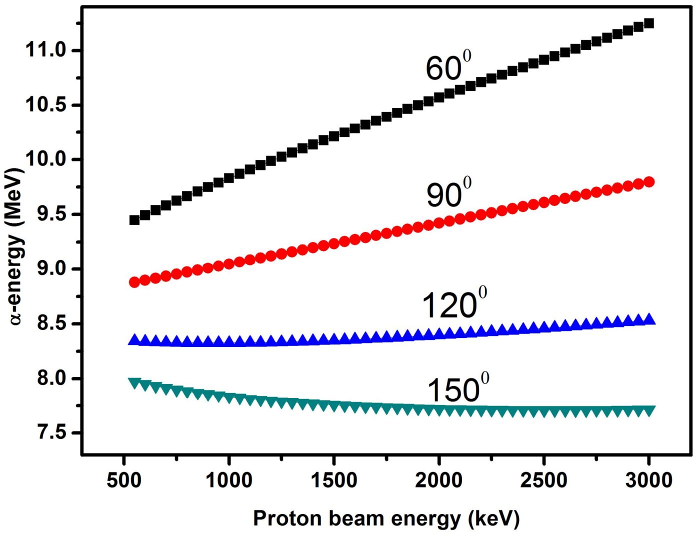

Fig.3.16: *Energy of α-particles emitted from* $^{7}Li(p,\alpha)^{4}He$ *reaction at 60°, 90° 120° and 150° angles (with respect to the beam direction). The reaction is induced by 0.55-3.0 MeV protons.*

Amongst the elements constituting the electrodes, interferences can arise from oxygen and fluorine through $^{18}O(p,\alpha)^{15}N$ (Q=3.98 MeV) and $^{19}F(p,\alpha)^{16}O$ (Q=8.11 MeV) nuclear reactions respectively. **Fig.3.17** shows the energy of α-particles emitted from the two reactions for 0.55-3.0 MeV protons at 90° and 150° angles. The energy of the α-particles have been calculated using **equations** similar to those represented by **(3.7), (3.8)** and **(3.9).** Both reactions exhibit normal kinematics. An examination of **Figs.3.16** and **3.17** shows that $^{18}O(p,\alpha)^{15}N$ reaction would not interfere up to sizable depths in the depth profile measurements of Li conducted at any proton energy and detection angle. However, extensive interferences can result from $^{19}F(p,\alpha)^{16}O$ reaction in measurements performed with 2.5-3.0 MeV protons at 150° angle. It, therefore, can be concluded that a detection angle of 150° is not suitable for depth profile measurements of Li in materials containing fluorine. This limitation is caused partly due to the inverse kinematics of the $^{7}Li(p,\alpha)^{4}He$ reaction at 150° angle and partly due to rather large cross-section of $^{19}F(p,\alpha)^{16}O$ reaction. The measurements, instead, can be best accomplished at a detection angle of 90° at which the α-particles from $^{7}Li(p,\alpha)^{4}He$ have substantially higher energy than those emitted from $^{19}F(p,\alpha)^{16}O$ reaction.

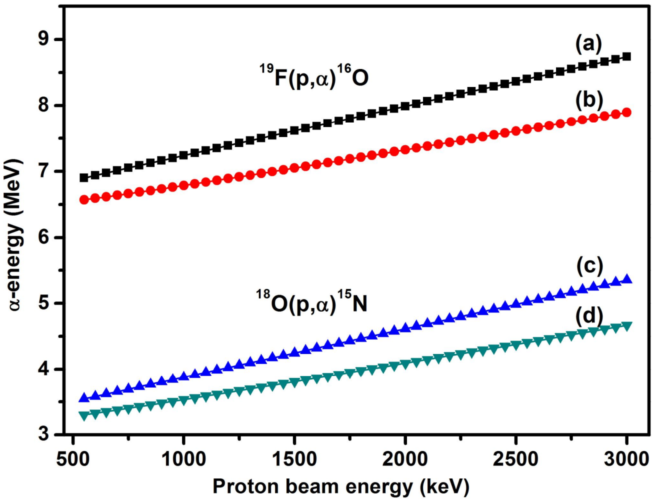

Fig.3.17: *Energy of α-particles emitted from ^{19}F(p,α)^{16}O reaction at (a) 90° and (b) 150° angles and those emitted from ^{18}O(p,α)^{15}N reaction at (c) 90° and (d) 150° angles. The reactions are induced by 0.55-3.0 MeV protons.*

3.3.2 Experimental details

3.3.2.1 Materials for analysis

The materials examined by PIGE were also investigated by NRA. The materials are described in detail in **Section 3.2.2.1**.

3.2.2.2 Proton beam irradiation

The NRA experiments entailed irradiation of targets with 2.0-3.0 MeV protons beams. The typical beam current was about 15 nA over a spot of 1.5 mm in diameter. The spectra of charged particles were recorded by a passivated implanted planar silicon (PIPS) detector (**Chapter 2, Section 2.6**) placed at 150° or 90° angles with respect to the beam direction. The detector was positioned at a distance of about 10 cm from the point of interaction and was covered with a 1.5 mm wide rectangular aperture. No stopper foil (between the detector and the sample) was used during the course of measurements. The experiments involving detection at 90° angle were carried out at a tilt angle (angle between sample surface normal and incident beam) of 30° while in rest of the cases, the beam was incident normally on the targets. The duration of an experiment ranged from 1.5 to 2.5 h depending on the nature of the sample.

3.3.3 Methodology of depth profiling by PIGE

The depth profile of Li in the samples by NRA was calculated using an approach similar to that suggested by Sagara et al. **[121]** with the main differences lying in the application of **equation (3.1**) for quantification and the utilisation of Li_2CO_3 as a standard for the purpose. The spectra were not analysed by simulation due to the lack of data on the cross-section of $^{7}Li(p,\alpha)^{4}He$ reaction at 90° angle around 3 MeV proton energy.

3.3.4 Analysis of samples

Fig. 3.18 compares the α-spectra of the thin film of LiF acquired at 2.0, 2.6 and 3.0 MeV at 90° and 150° detection angles. The peaks correspond to Li and F that arise from $^{7}Li(p,\alpha)^{4}He$ and $^{19}F(p,\alpha)^{16}O$ reactions respectively. The probing depth of the $^{7}Li(p,\alpha)^{4}He$ reaction in a material consisting of Li and F depends on the difference in energy between the α-particles emitted from $^{7}Li(p,\alpha)^{4}He$ reaction i.e. $(E\alpha)_{Li}$ and $^{19}F(p,\alpha)^{16}O$ reaction i.e. $(E\alpha)_F$. **Fig. 3.18,** in fact, provides an experimental depiction of an interesting trend in the variation of $(E\alpha)_{Li}$ and $(E\alpha)_F$ with beam energy for measurements carried out at 150° detection angle. Expressing more explicitly, at this detection angle, at E_p= 2.0 MeV $(E\alpha)_{Li} > (E\alpha)_F$, at E_p= 2.6 MeV $(E\alpha)_{Li} \cong (E\alpha)_F$ (this causes extensive overlap of Li and F signals), while at E_p= 3.0 MeV $(E\alpha)_{Li} < (E\alpha)_F$. This trend in the variation in $(E\alpha)_{Li}$ and $(E\alpha)_F$ is a direct consequence of the inverse kinematics exhibited by $^{7}Li(p,\alpha)^{4}He$ reaction at 150° detection angle. Thus it can be concluded that while 2.0 MeV protons have a limited probing depth (~ 1 μm), 2.6 as well as 3.0 MeV protons are not suitable for depth profiling Li in this geometrical condition due to the interference from fluorine. The depth profile of Li reported by Gonzalez-Arrabal et al. suffers from such a limitation **[124]**. On the other hand, the interference is obviated in measurements conducted at 90° angle since $(E\alpha)_{Li} > (E\alpha)_F$ for any proton energy, enabling profiling of Li up to a depth of a few microns. These results are consistent with the postulations made in **Section 3.3.1** on the basis of kinematics of the reactions. However, it must be emphasised that for materials not containing F, the analysis can be performed at any of the two or any other suitable angle. Also, for measurements conducted at 90°angle (a) the signals of Li or F are comparatively broader due to beam incidence at 30° tilted angle and (b) 2.0 MeV protons offer a marginal advantage over higher energy beams (e.g. 3.0 MeV) in terms of probing depth but it is offset by larger reaction cross-sections around E_p=3.0 MeV.

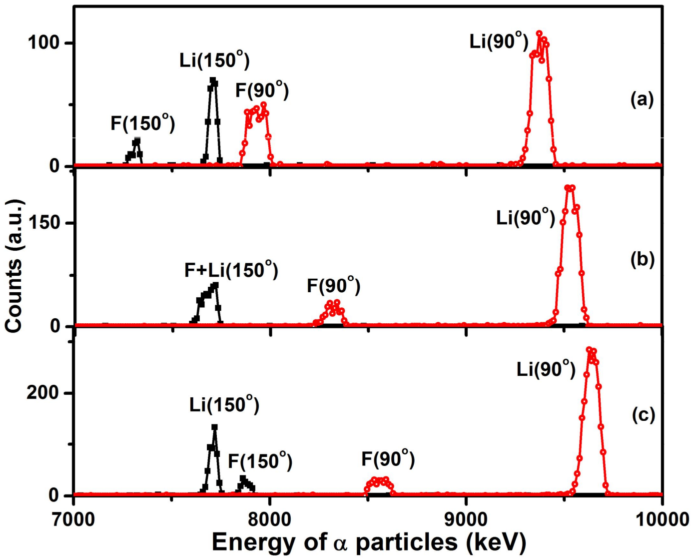

***Fig.3.18**: α- spectra of a LiF thin film acquired with (a) 2.0 MeV, (b) 2.6 MeV and (c) 3.0 MeV protons at 90° and 150° detection angles. The peaks designated as Li and F result from* $^{7}Li(p,\alpha)^{4}He$ *and* $^{19}F(p,\alpha)^{16}O$ *reactions respectively.*

Fig.3.19 shows the α-spectra of Li_2CO_3 (standard), and cathode (lithium cobalt oxide) and anode (graphite) recorded at E_p=3.0 MeV and 90° detection angle. The presence of F in cathode is indicated by the corresponding spectrum but its presence in the anode is barely discernible. The concentrations of Li in the specimens as a function of depth are presented in **Figs 3.12 (b)** and **3.14(b)** respectively. The probing depth in the specimens is limited to only about 5-8 µm due to the presence of fluorine in the specimens. In materials that do not contain fluorine, for example, Li_2CO_3, the probing depth is about 30 μm. The sensitivity of the method is about 0.1 at.% while its depth resolution, dominated mainly by the energy resolution of the charged particle detector is ~ 100 nm in graphite and ~ 60 nm in $LiCoO_2$. The combined uncertainty associated with the method is about 6%. As evidenced by the plots in **Figs.3.12** and **3.14**, the profiles of Li measured by PIGE and NRA are in good agreement. It demonstrates the efficacy of both the methods in depth profiling Li in materials.

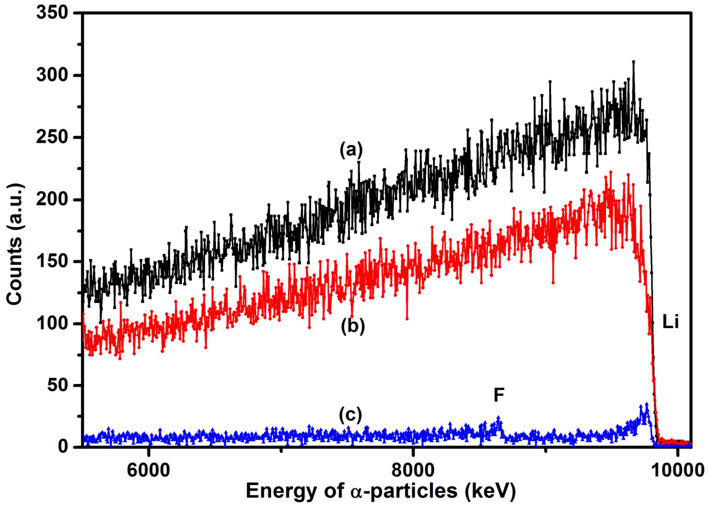

***Fig. 3.19**: α- spectra of (a) Li_2CO_3 (disc) and thick coatings of (b) $LiCoO_2$ and (c) graphite acquired with 3.0 MeV protons at 90° detection angle.*

Before concluding the section it is instructive to compare the analytical features of IBA with those of NDP. With a probing depth of about 30 μm and a depth resolution of 150-250 nm, IBA is as competent as NDP in depth profiling lithium. However, the latter possesses better detection sensitivity. But IBA is selective to ^{7}Li, the isotope having higher natural abundance (92.5 %) unlike NDP which is selective to ^{6}Li. The methodology based on $^{7}Li(p,\alpha)^{4}He$ reaction for depth profiling Li is similar to NDP in several ways and can be utilized for real time in-situ estimation of Li transport in a battery. High probing depth, good depth resolution, ability to discriminate interfaces and a broad maximum in cross-section at a proton energy of about 3 MeV are some of the features of ^{7}Li(p,α)^{4}He reaction that make it potentially applicable for in-situ studies of Li transport.

3.4. Conclusions

Two ion beam analysis methods- one based on ^{7}Li(p,γ)^{8}Be resonance reaction at 441 keV and another involving ^{7}Li(p,α)^{4}He reaction- are described for non-invasive depth profiling of Li in the electrode materials of a Li-ion battery. The methods differ significantly in terms of underlying principles, experimental arrangements, the mode of data acquisition and treatment, and speed of analysis.

The method based on ^{7}Li(p,γ)^{8}Be resonance reaction involves the measurement of 14.6 and 17.6 MeV γ-rays at several beam energies above 441 keV to obtain the depth profiles. The detection sensitivity, depth resolution and probing depth of the method are ~0.2 at.%, ≥150 nm and >20 µm respectively. The depth profile of Li by ^{7}Li(p,α)^{4}He reaction, on the other hand, is obtained from the α-spectrum recorded by inducing the reaction with 2.0/3.0 MeV protons. The analytical features of the method are comparable to those of the ^{7}Li(p,γ)^{8}Be resonance reaction. Both methods are interferred by fluorine. The interference, however, it is more severe for ^{7}Li(p,α)^{4}He reaction but is alleviated to a large extent by making measurements at 90° detection angle. The analytical features of the methods (probing depth in particular) are closely related to two major findings; one pertains to the non-occurrence of the resonance at 1031 keV in ^{7}Li(p,γ)^{8}Be reaction while the other, to the transition in the kinematics of ^{7}Li(p,α)^{4}He reaction from normal to inverse one above 120° detection angle. In summary, both methods are simple and precise, and can be conveniently adopted for depth profile measurements of Li in the electrodes of a Li-ion battery and in other materials as well.

Chapter 4

Analysis of Boron Carbide: Determination of Atomic and Isotopic Ratio

4.1 Introduction

Boron carbide, a non-metallic material, is characterized by several unique physical and chemical properties such as high hardness (~30 GPa), low density (~2.52 g cm-3), excellent chemical and thermal stability and high neutron absorption capability **[35,36].** High hardness and low density make it a premier material for armor and ballistic applications while the pronounced thermal and chemical stability render it eminently suitable for refractory applications **[37,38]**. Its widespread usage in abrasive powders and coatings results from its excellent abrasion resistance **[35].** It is a p-type semiconductor characterized by a band gap of ~ 2.09 eV and displays good thermoelectrical properties as well **[39,40]**. Due to the high cross section of the $^{10}B(n,\alpha)^{7}Li$ nuclear reaction, about 3800 barns for thermal neutrons, boron carbide enriched in ^{10}B isotope is used in control rods in nuclear reactors **[41]**. The rods are manufactured using sintered cylindrical pellets which, in turn, are prepared by hot pressing boron carbide powders at temperatures ≥ 2000 K and pressures ≥ 20 MPa.

Boron carbide is a non-stoichiometric compound and exists over a large homogeneity range extending from about B_4C, or according to some researchers, $B_{4.3}C$ at the carbon-rich to $B_{12}C$ at the boron-rich limit **[43-45]**. Remarkably, the material maintains phase singularity throughout this compositional range but experiences a change in properties with composition. It is reported that most of the mechanical properties are best realized for carbon-rich compositions **[35]**. However, at carbon concentrations in excess of 20 at.%, these properties undergo a sharp decline due to the precipitation of the carbon phase from the B_4C solid solution **[46]**. Similar to mechanical properties, Seebeck coefficient and electrical conductivity, the two thermoelectric properties, are also influenced by the carbon content of the ceramic with the former registering an increase and the latter, a decrease with increase in carbon concentration **[35]**. Therefore, a determination of the B/C ratio of the ceramic is required for the optimization of the synthetic conditions for preparing ceramics with tailor-made properties. Apart from the B/C ratio, the determination of free carbon and the isotopic analysis of boron are the two other important analytical requisites for a comprehensive evaluation of the properties and performance of the material. Free carbon has a pronounced influence on the densification kinetics of the carbide and affects its properties in multiple ways **[47,48]**. The isotopic analysis of boron in the powder or sintered product, on the other hand, is important from the point of view of ascertaining its efficacy as a neutron absorber.

Due to its high thermal and chemical stability and low Z non-metallic constituents, boron carbide is analytically intractable. The difficulties in analysis are more pronounced in sintered products. The determination of boron (total) is usually accomplished by wet-chemical methods which entail carbonate fusion of the powders (obtained by crushing/grinding in the case of sintered pellets) followed by titrimetry or spectroscopic measurements of the resulting solutions **[130]**. Similarly, the isotopic analysis is performed by inductively coupled mass spectrometry measurements of the solutions of the materials. The determination of carbon, on the other hand, involves the combustion of the ceramic in oxygen and the detection of the evolved carbon-dioxide gas with an infra-red detector **[130]**. Apparently, the determination of B/C and $^{10}B/^{11}B$ ratios by the chemical method is tedious and time consuming. So far as non-destructive methods of analysis are concerned, X-ray based techniques such as X-ray fluorescence (XRF) and particle induced X-ray emission (PIXE) are not suitable due to the difficulty in the detection of very low energy B K_{α} (183 eV) and C K_{α} (277 eV) X-rays. Neutron activation analysis too is not applicable in view of the rather unfavorable nuclear properties of the isotopes of B and C for activation with thermal neutrons.

The difficulties described above warrant the development of a simple methodology for the analysis of boron carbide. In this context we have examined the applicability of particle induced γ-ray emission technique (PIGE), a prominent ion beam analysis (IBA) method, with particular emphasis on the analysis of sintered specimens. It is a non-destructive technique and is widely used for the determination of light elements through the measurement of prompt γ-rays emitted from nuclear reactions **[82,131,132]**. Presently, the $^{10}B(p,\alpha\gamma)^{7}Be$, $^{10}B(p,p'\gamma)^{10}B$ and $^{11}B(p,p'\gamma)^{11}B$ nuclear reactions that emit 429, 718 and 2124 keV γ-rays respectively are used for the determination of B and the $^{13}C(p,p'\gamma)^{13}C$ nuclear reaction (E_γ = 3089 keV), for the determination of carbon **[81,133-135]**. The reactions are induced simultaneously in the material at the 3.8 to 4.2 MeV proton energy range. The method, therefore, not only provides the B/C ratio but facilitates the isotopic analysis of boron as well, addressing in the process two of the three analytical requisites necessary for the development of this important engineering material. In addition to PIGE, the efficacy of elastic backscattering spectrometry (EBS) with protons, yet another important IBA technique, in analyzing the two compositional aspects of boron carbide has been probed.

***Table 4.1**: Nuclear reactions and the energy of γ-rays utilized in the analysis of boron carbide*

Nuclear reaction	E_γ (keV)
$^{10}B(p,\alpha\gamma)^{7}Be$	429
$^{11}B(p,p'\gamma)^{11}B$	718
$^{11}B(p,p'\gamma)^{11}B$	2124
$^{13}C(p,p'\gamma)^{13}C$	3089

4.2 PIGE measurements

The PIGE experiments were conducted for two different kinds of measurements. The first involved the determination of thick target yields of the 429, 718 and 2124 keV γ-rays emanating from the $^{10}B(p,\alpha\gamma)^{7}Be$, $^{10}B(p,p'\gamma)^{10}B$ and $^{11}B(p,p'\gamma)^{11}B$ nuclear reactions respectively and the 3089 keV γ-rays produced from the $^{13}C(p,p'\gamma)^{13}C$ nuclear reaction in the 3.0 to 4.2 MeV proton energy range. These reactions are presented in **Table 4.1** for ready reference. The measurements were conducted to determine the optimum conditions of irradiation for the second set of measurements that involved the analysis of the boron carbide specimens.

4.2.1 Experimental details

4.2.1.1 Materials

A large number of samples were analysed for standardizing the methodology and its validation. The description of the samples is given in **Chapter2, Section 2.2**. The list of the synthetic samples (composition known *a priori*) and sintered discs (unknown composition) are listed in **Table 4.2** along with their abbreviated names for the purpose of better clarity and brevity. Elemental boron and graphite are used as standards.

Table. 4.2: *List of samples and their nomenclature*

Sl.No.	Nature	Composition		Nomenclature
		B (wt.%)	C (wt.%)	
1.	Powder	100	-	B
2.		-	100	C
3.		80	20	BC-20
4.		70	30	BC-30
5.		50	50	BC-50
6.		-	-	BC-P1 and BC-P2
7.	Sintered	-	-	BC-S1 to BC- S8

4.2.1.2 Proton beam irradiation

The irradiation of the samples (targets) is described in detail in **Chapter 2, Section 2.6**. Briefly, the samples, discs made from the powders or sintered specimens, were fixed on the sample manipulator, which in turn was mounted on the scattering chamber. In order to maintain identical geometrical condition during the analysis of the sintered boron carbide specimens, the boron and graphite standards were placed on the top of two different sintered boron carbides. The beam was incident at normal to sample surface during the analysis. Therefore, except for beam current and total incident charge, the other experimental conditions were identical for the specimens and the standards.The scattering chamber was evacuated to 1×10^{-6} torr. The diameter of the proton beam was < 2mm while its current and energy ranged in 2 - 300 nA and 1- 4.2 MeV respectively.

4.2.1.3 Acquisition of γ-ray spectrum

The prompt γ-rays were detected by HPGe detector (**Chapter 2, Section 2.6**) placed in the direction of the beam. The detector subtended a solid angle of 0.46 sr for thick target yield measurements while, 0.12 sr during the analysis of boron carbide specimens. The dead time was kept below 8% during the course of the measurements. Since some of the boron carbide samples were significantly enriched in ^{10}B which, as described in the subsequent sections, has a high thick target yield, their analysis was carried out at a detector solid angle of 0.12 sr in order to maintain the dead time of counting within the stated level. Each specimen was irradiated for charges (usually 15-18 μC) sufficient to produce statistically significant spectra. As a result, each irradiation lasted for about 2.5 to 3h.

A pictorial representation of the experiment involving (a) irradiation of the target with proton beam and (b) the detection of the emanating prompt γ-rays is given in **Fig.4.1.** The details of the features of the detector and the electronics of the data acquisition system are described in detail in **Chapter 2, Section 2.6**.

Fig.4.1: *A schematic representing the irradiation and emission of γ-rays of boron and carbon simultaneously from a sintered pellet of boron carbide.*

4.2.2 Quantification

The quantification of an element by PIGE can be accomplished by the absolute method or the relative method. The absolute method is based on the fundamental principles and utilizes a number of parameters for calculation **[85]**. Apparently, the accuracy of quantification is influenced by the errors associated with the measurement of these parameters. In the relative method, on the other hand, several of the parameters are cancelled. These include the detector efficiency and the reaction cross-section whose accurate determination is often difficult. The relative method is therefore simpler and enables quantification with rather better accuracy. Taking cognizance of the fact, the relative method was preferred to the absolute method for quantification in the present studies. **(Chapter 2, Section 2.3.4)**

Boron carbide can be represented by the chemical formula B_xC_y or preferably by $^{10}B_m{}^{11}B_nC_y$ where m+n = x in view of the objectives of the investigations. The following equation meant to calculate the isotopic ratio i.e. m/n can be derived from the standard expression of thick target γ-rays yield

$$\left(\frac{m}{n}\right)_{BC} = \frac{\left(\frac{A_i}{A_j}\right)_{BC}}{\left(\frac{A_i}{A_j}\right)_{std}} \times \left(\frac{m}{n}\right)_{std} \qquad (4.1)$$

where BC and std represent boron carbide and standard namely elemental boron respectively, A_i is the area under the peak of 429 keV or 718 keV γ-ray from ^{10}B isotope, A_j is the area under the 2124 keV γ-ray from ^{11}B isotope while $(m/n)_{std}$ is the isotopic ratio of boron (i.e.$^{10}B/^{11}B$) in the standard which, in the present case, is 0.247 (i.e natural isotopic ratio). The area under a peak is obtained after the subtraction of a linear background from the gross area of the peak.

The isotopic percentage of ^{10}B i.e. $^{10}B_{BC}$ or that of ^{11}B i.e. $^{11}B_{BC}$ in the sample can be calculated from the following equations:

$$^{10}B_{BC} = \left(\frac{\left(\frac{m}{n}\right)}{1+\left(\frac{m}{n}\right)} \right)_{BC} \times 100 \ ; \ ^{11}B_{BC} = \left(\frac{1}{1+\left(\frac{m}{n}\right)} \right)_{BC} \times 100 \qquad (4.2)$$

Similarly the atomic ratio of B to C i.e. x/y can be calculated from the following expression

$$\left(\frac{x}{y}\right)_{BC} = \frac{\left(\frac{Y_{i(j)}}{Y_k}\right)_{BC}}{\left(\frac{Y_{i(j)}}{Y_k}\right)_{std}} \times \frac{\varepsilon_C}{\varepsilon_B} \times \frac{\left(^{10}B\left(^{11}B\right)\right)_{BC}}{\left(^{10}B\left(^{11}B\right)\right)_{std}} \qquad (4.3)$$

where Y_i or Y_j is the yield (charge and solid angle normalized peak area) of 429 keV (or 718 keV) γ-ray from ^{10}B isotope or 2124 keV γ-ray from ^{11}B isotope respectively. Y_k is the yield (charge and solid angle normalized peak area) of 3089 keV γ-ray from ^{13}C isotope and ε_C and ε_B are the stopping cross-sections of protons in carbon and boron respectively at the incident beam energy. Due corrections were made for the enrichment of ^{10}B or ^{11}B while determining the B/C ratio in samples with ^{10}B/ ^{11}B isotopic ratio different from 0.247. The stopping cross-sections were calculated using the Ziegler-Biersack- Littmark formulations **[102]**.

4.2.3 Experimental results (γ-ray spectra and thick target yields)

4.2.3.1 ^{natural}B: γ-ray spectra and features

Fig.4.2 (a) shows the prompt γ-ray spectrum acquired on irradiating the elemental boron (natural) disc with a 3 MeV proton beam. The spectrum consists of 429, 718 and 2124 keV γ-rays that originate from the ^{10}B(p,αγ)^{7}Be, ^{10}B(p,p′γ)^{10}B and ^{11}B(p,p′γ)^{11}B nuclear reactions respectively, induced simultaneously in the disc by the proton beam. The γ-rays are, in fact, emitted as a result of the transition from the first excited states to the corresponding ground states of ^{7}Be, ^{10}B and ^{11}B nuclei respectively **[125,136]**. The nuclear reactions occur at higher incident energies as well. Therefore, similar spectra, for example [**Fig.4.2(b)**], are obtained on irradiations with higher energy protons. These spectra, however, possess some additional peaks. The γ-ray peak at 415 keV, marked as 1 in **Fig.4.2(b)**, arises from the transition from the third excited to second excited state of ^{10}B, while those at 563 (peak 2) and 598 keV (peak 3) correspond to the ^{76}Ge(n,n′γ)^{76}Ge and ^{74}Ge(n,n′γ)^{74}Ge nuclear reactions respectively occurring in the Ge detector **[125,137]**. The peak at 693 keV (peak 4) has contributions from the ^{72}Ge(n,n′e^{-})^{72}Ge inelastic scattering and the γ-ray originating from the transition from the seventh to the sixth state of the ^{11}B nucleus **[136,137]**. The neutrons involved in nuclear reactions with Ge are produced from the ^{11}B(p,n)^{11}C (Q = –2.8 MeV) reaction at higher proton energies. It is also observed, on a careful examination of the spectra in **Fig.4.2**, that the 2124 keV γ- ray peak (13 keV) has the largest width while the 718 keV γ-ray peak (4 keV), the least. The width of the 429 keV γ-ray peak (10 keV) is marginally lower than that of the 2124 keV γ- ray peak. The comparatively larger widths of the 2124 and 429 keV γ-ray peaks are due to Doppler broadening caused by the shorter lifetimes of the first excited states of ^{11}B and ^{7}Be which measure 5.5 and 192 fs respectively **[136]**. Incidentally, the first excited state of ^{10}B has a much longer lifetime of 1.02 ns **[125]**.

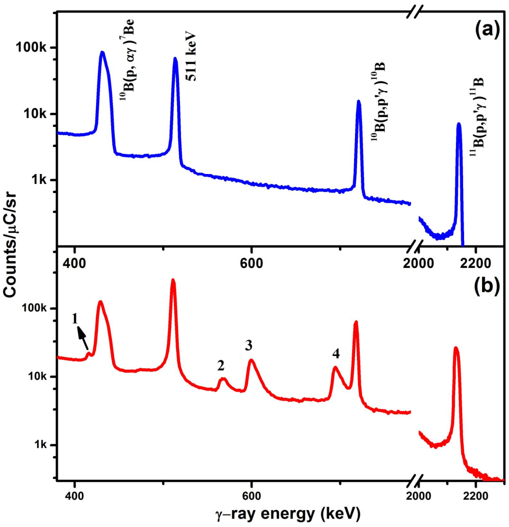

***Fig.4.2**: Prompt γ-ray emission spectra of elemental boron target recorded at (a) 3 MeV and (b) 4.2 MeV proton energies. The peaks numbered 1, 2, 3 and 4 are identified and discussed in text.*

4.2.3.2 Thick target yields of 429, 718 and 2124 keV γ-rays

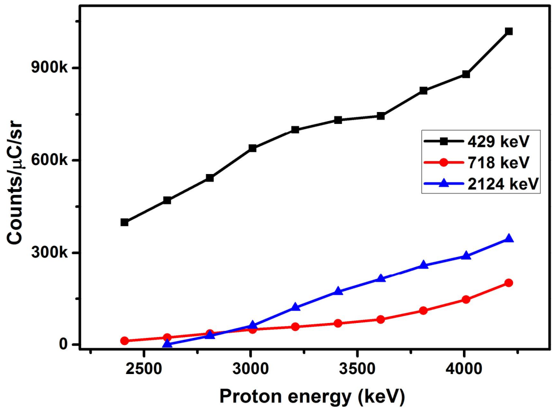

Fig.4.3: *Thick target yields of 429, 718 and 2124 keV γ-rays in 2.4 - 4.2 MeV proton energy region. The target is elemental boron.*

Fig.4.3 shows the charge and solid angle normalized yields of the 429, 718 and 2124 keV γ-rays in the 3-4.2 MeV proton energy range. The yields are not normalized to the absolute efficiency of the detector since its value for the γ-rays of different energies is not known precisely. Two important conclusions can be drawn from the yield curves. Firstly, the yields of γ-rays of all the three energies increase monotonically with incident energy and secondly, $^{10}B(p,\alpha\gamma)^{7}Be$ reaction remains predominant throughout the whole proton energy range. In terms of interferences, it is worthwhile mentioning that the 429 keV γ-rays are also emitted from the $^{7}Li(p,n\gamma)^{7}Be$ reaction while 2127 keV γ-rays are emitted from the $^{34}S(p,p'\gamma)^{34}S$ and $^{37}Cl(p,\alpha\gamma)^{34}S$ nuclear reactions as well. $^{10}B(p,\alpha\gamma)$ and $^{7}Li(p, n\gamma)^{7}Be$ reactions have comparable yields of 429 keV γ-rays. Therefore, the presence of lithium in boron carbide even at low concentration levels (e.g. 1 at.%) can impair the determination of boron through 429 keV γ -rays from the $^{10}B(p,\alpha\gamma)^{7}Be$ nuclear reaction. However, the 718 keV γ-rays from $^{10}B(p,p'\gamma)^{10}B$ nuclear reaction do not suffer from any interference and thus can be utilized for analysis in the case of any perceptible interference from lithium. Meanwhile, the interferences from the $^{34}S(p,p'\gamma)^{34}S$ and $^{37}Cl(p,\alpha\gamma)^{34}S$ nuclear reactions are less significant since the yields of the 2127 keV γ-rays from the two reactions are 1-2 orders of magnitude lower in comparison to 2124 keV γ-rays from the $^{11}B(p,p'\gamma)^{11}B$ nuclear reaction.

4.2.3.3 $^{natural}C$: γ-ray spectra and thick target yields of 3089 keV γ-rays

Fig.4.4 shows the prompt γ-ray spectra recorded on irradiating the graphite disc with the 3.5-4.2 MeV proton beam. The broad peaks at about 3110 keV in the spectra are due to the γ-ray emitted from the $^{13}C(p,p'\gamma)^{13}C$ nuclear reaction. The shift in peak energy from 3089 keV to about 3110 keV is probably due to the Doppler effect. No other γ-ray from nuclear reactions involving the ^{12}C or ^{13}C isotope is discernible in the spectrum. The larger width of the peak is, as witnessed for the $^{11}B(p,p'\gamma)^{11}B$ reaction, due to Doppler broadening brought about by the shorter lifetime (1fs) of the first excited of the ^{13}C nucleus **[135]**. The spectra possess peaks (not shown) at 563, 598 and 962 keV originating from the neutron induced reactions mentioned earlier. The neutrons in this case are produced from the $^{13}C(p,n)^{13}N$ reaction (Q= –3.0 MeV) reaction. **Fig.4.5** displays the charge and solid angle normalized yields of the 3089 keV γ-rays in the 3.6-4.2 MeV proton energy range. The yields, evidently, increase linearly with the incident beam energy. However, it is also observed that: (i) the reaction commences at $E_p \sim 3.6$ MeV, a fact more emphatically buttressed by the absence of any noticeable 3089 keV γ-ray peak in the spectrum recorded with $E_p = 3.5$ MeV shown in **Fig.4.4** (d) and (ii) the yields are statistically significant at $E_p \geq 3.8$ MeV. It is important to note that the reaction does not suffer from any interference.

4.2.3.4 Selection of irradiation parameters

A consideration of the yield curves of boron and carbon is useful in selecting the irradiation parameters, namely the beam energy and current, for the analysis of boron carbide. Apparently, 4.0-4.2 MeV is the beam energy of choice, while a beam current of about 2nA is desirable in order to keep the dead time below 8%. The onset of higher dead time (>10%) on irradiation even with a 1 nA beam current limits the proton beam energy to 4.2 MeV. A similar situation arises on irradiation with 4.0-4.2 MeV beams of > 3nA current. The rather large dead time, even under the experimental irradiation conditions employed, arises from the phenomenal yields of the (a) 429, 718 and 2124 keV γ-rays and (b) the 511 keV annihilation radiation produced from the $^{10}B(p,\gamma)^{11}C$ (Q= 8.7 MeV), $^{11}B(p,n)^{11}C$, $^{12}C(p,\gamma)^{13}N$ (Q= 1.9 MeV) and $^{13}C(p,n)^{13}N$ nuclear reactions. ^{11}C and ^{13}N are positron emitters with half lives of 20 min and 10 min respectively.

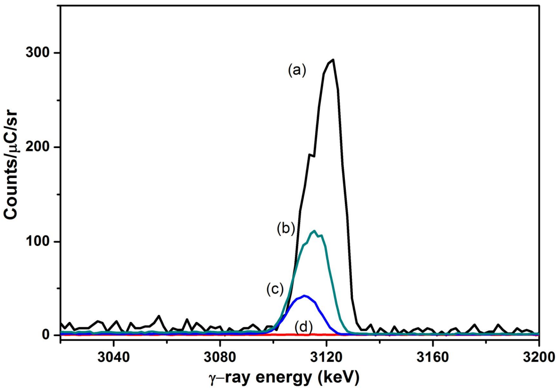

Fig.4.4*: Prompt γ-ray emission spectra of elemental graphite target recorded at (a) 4.2 MeV, (b) 4.0 MeV, (c) 3.8 MeV and (d) 3.5 MeV proton energies.*

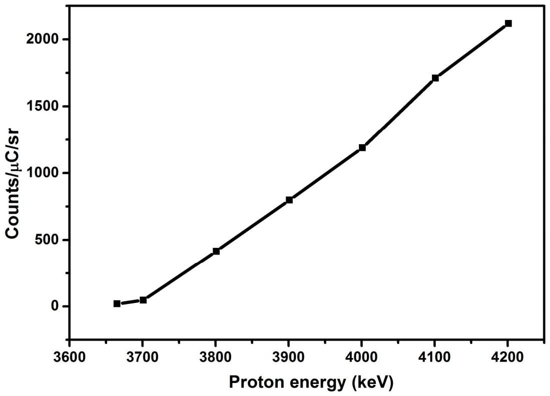

Fig.4.5*: Thick target yield of 3089 keV γ-ray in 3.6- 4.2 MeV proton energy region. The target is elemental graphite.*

4.2.4 Analysis of boron carbide samples: Results and Discussion

Fig.4.6 shows the prompt γ-ray spectra of powder and sintered boron carbide specimens registered with 4.2 MeV protons. The peaks corresponding to the 429 and 718 keV γ-rays from ^{10}B and the 2124 keV γ-rays from ^{11}B are conspicuously seen in the spectra. Also distinctly visible are the peaks due to the 3089 keV γ-rays from ^{13}C in spite of their comparatively much lower intensity. The specimens did not contain Li, Cl and S, the interfering elements, in detectable levels. It was concluded on the basis of the absence of any perceptible γ-rays of 478, 1220 and 2230 keV in energy from the $^{7}Li(p,p'\gamma)^{7}Li$, $^{35}Cl(p,p'\gamma)^{35}Cl$ and $^{32}S(p,p'\gamma)^{32}S$ reactions respectively that have thick target yields several times higher than those of the interfering γ-rays **[82]**. It is nevertheless instructive to mention that the 478 keV γ-rays are also emitted from the decay of the ^{7}Be isotope ($t_{1/2}$ = 1253.6 days) produced through the ^{10}B(p,αγ)^{7}Be nuclear reaction. However, sufficient activity is not generated under the present irradiation conditions. As a result, the γ-ray peak remains obscured under the higher background of 511 keV γ-rays in the prompt γ-ray spectra but is observed in the delayed γ-ray spectra acquired after the completion of the irradiation. In terms of impurities, the ceramics contained Al and Fe in low levels. Since the presence of these elements in low concentrations is not likely to influence the present measurements, no concerted efforts were made to determine them.

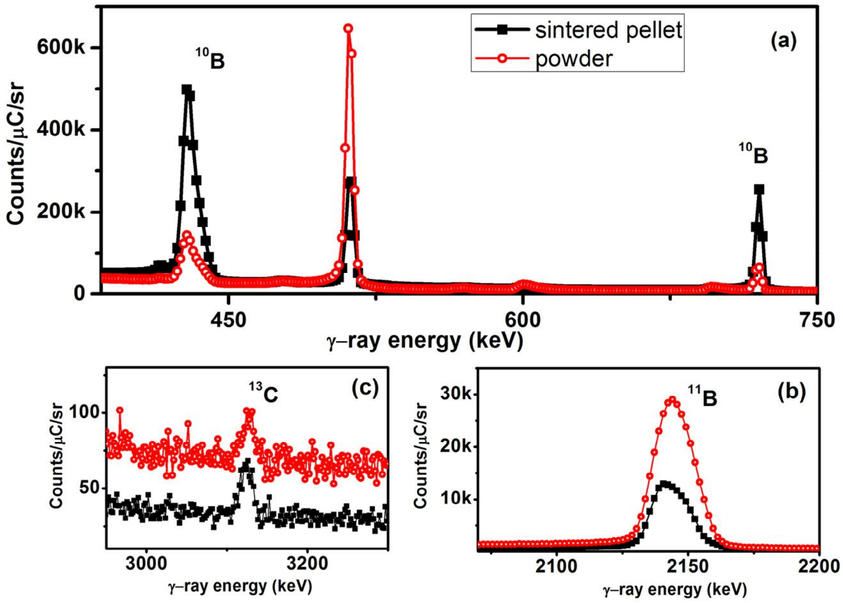

***Fig.4.6**: Prompt γ-ray emission spectra of powder (BC-P2) (open circle) and sintered pellet (BC-S1) (solid squares) boron carbide targets recorded with 4.2 MeV proton beams. (a), (b) and (c) represent the different regions of the same spectra.*

The isotopic ratio of ^{10}B to ^{11}B and the contents of B and C determined using **equations (4.1)** and **(4.3)** in the synthetic mixtures, and in the powder and sintered specimens of boron carbide are listed in **Tables 4.3** and **4.4** respectively. The measurements have been performed using 4.2 MeV protons while the 429 keV γ-rays from ^{10}B(p,αγ)^{7}Be nuclear reaction are employed for the quantification of ^{10}B isotope. The choice of 429 keV γ-rays (instead of 718 keV γ-rays from $^{10}B(p,p'\gamma)^{10}B$ scattering) is based on the fact that the boron carbide specimens did not contain any interfering elements in detectable levels. Another factor governing this selection is the difficulty in defining a proper background under the peak of 718 keV γ-rays due to the presence of a peak at 693 keV in the γ-ray spectrum (**Fig.4.2**). As discussed earlier, the peak at 429 keV, too, is preceded by a peak at 415 keV. However unlike the peak at 693 keV, its origin is entirely due to ^{10}B and therefore, was included in yield calculations. It dispels any ambiguity that can arise in the assertion of the background under the 429 keV γ-ray peak. However, it is important to mention that in view of any discernible peak at 693 keV, the 718 keV γ-rays in a spectrum recorded at E_p= 3.0 MeV can be utilized for the quantification of ^{10}B isotope.

Table.4.3: *$^{10}B/^{11}B$ isotopic ratio and atomic composition of synthetic mixtures determined by PIGE (E_p = 4.2 MeV).*

S.No.	Specimen	B (at.%)		C (at.%)		$^{10}B : ^{11}B$
		Theoretical	Determined	Theoretical	Determined	
1	BC-20	81.62	82.4	18.38	17.6	20 : 80
2	BC-30	72.15	71.8	27.85	28.2	19.9 : 80.1
4	BC-50	52.61	53.1	47.39	46.9	19.8 : 80.2

A perusal of the yield curves in **Figs. 4.3** and **4.4** show that the probing depths of nuclear reactions involving boron and carbon are significantly different. At E_p=4.2 MeV, these are ≥ 50 μm for the $^{10}B(p,\alpha\gamma)^{7}Be$ or $^{11}B(p,p'\gamma)^{11}B$ reactions and ~25 μm for the $^{13}C(p,p'\gamma)^{13}C$ reaction. The $^{10}B/^{11}B$ ratio, therefore, represents the average isotopic ratio over a depth of about 50 μm, while the B/C ratio, the average composition over a depth of about 25 μm. The $^{10}B/^{11}B$ ratio in all the powder samples is in fair agreement with the natural isotopic abundance of the element. Good conformity is also observed between the determined and the theoretical B/C ratios of the synthetic mixtures. It is pertinent to mention that the limit of detection of carbon in BC-20, calculated on the basis of three times of the standard deviation of the baseline, is about 5 wt.%. Notably the contents of boron in powder boron carbide samples are consistent with those determined chemically (**Table 4.3**). The results suggest the suitability of PIGE in determining the ^{10}B/^{11}B isotopic ratio of boron and B/C ratio in boron carbide.

An examination of data in **Table 4.4** shows that sintered discs are enriched in ^{10}B isotope. Due corrections were made for the attenuation of γ-rays of all the four energies in the sintered discs, along while calculating the boron isotopic ratio and the B/C ratio. Since the attenuation of γ-rays in a given thickness of a material decreases with their energy, the extent of attenuation in preliminary experiments was found to be maximum for 429 keV γ-rays and, following the trend, minimum for 3089 keV γ-rays. The attenuation of γ-rays of such a broad energy range in boron carbide, to the best of our knowledge, is not reported in literature though there is a recent study for 661.2 keV (^{137}Cs) and 1.25 MeV (mean energy of ^{60}Co radiations) γ-rays **[138]**. Apparently, any failure to take the cognizance of the attenuation of γ-rays in the sintered specimens would result into an underestimation of the ^{10}B isotope and as well as the B/C ratio. Since the attenuation of the γ-rays was not explicitly determined presently, the experiments (irradiation, as well as counting) were conducted by fixing the standards atop two different sintered pellets in order to minimize errors. Importantly, the attenuation in the standards was assumed to be negligible due to their low thicknesses. It is to be noted that the sintered specimens could not be analyzed by chemical methods due to difficulties in pulverizing them to fine powders for carbonate fusion.

So far as the uncertainty of measurements is concerned, it is ~3% for thick target yields and it has contributions from peak area (1%), charge integration (2%) and solid angle (2%) measurements. The combined uncertainty in the determination of isotopic analysis is about 2% with contributions from uncertainties associated with peaks areas of 429 or 718 keV and 2124 keV γ-rays for the sample as well as the standard. Since the analysis is based on a comparative technique and the γ-rays are measured simultaneously, uncertainties associated with charge integration, detector efficiency and solid angle are not considered in the calculations. Meanwhile, the combined uncertainty of B/C ratio is about 5%, which is calculated by propagating the standard uncertainties of peak area and integrated charge for the specimen and the standard as well, and those (3 % each) pertaining to the stopping cross sections for boron and carbon.

Finally, before concluding, it is important to compare the present methodology with that described in reference **[139]** which, to the best of our knowledge, is the only method reported hitherto for the determination of B/C ratio in boron carbide by PIGE. The method, among other reactions, utilizes the $^{11}B(p,\gamma)^{12}C$ and $^{12}C(p,\gamma)^{13}N$ nuclear reactions and with the maximum E_p being ~ 1 MeV, has comparatively much lower probing depths. Secondly, in sharp contrast to the present approach, the beam current employed is as high as 2.75 µA which necessitates the utilization of lead shields of thickness up to 5 cm, presumably to attenuate the 429 keV γ-rays emanating from the $^{10}B(p,\alpha\gamma)^{7}Be$ nuclear reaction as the measurements are performed for a total charge of 3000 µC. However, as one of the advantages, the method enables the determination of the $^{12}C/^{13}C$ isotopic ratio (in addition to the $^{10}B/\,^{11}B$ one) as well unlike the present methodology wherein the analysis is based on the ^{13}C isotope with the assumption that the natural isotopic abundance of carbon is preserved in the boron carbide specimens. The 2360 keV γ-rays from the $^{12}C(p,\gamma)^{13}N$ reaction are not observed under the present experimental conditions due to the very low proton current and elevated levels of background.) PIGE with 4 MeV protons has been used for the determination of boron and or $^{10}B/^{11}B$ ratio in boron carbide in previous studies **[140,141]**. However, as compared to the present one, these differ significantly in terms of sample (target) preparation and do not discuss spectral features as well which is very important to get an insight of the processes taking place during irradiation. Lastly, the analysis in these studies is confined to boron carbide powders.

Table.4.4: *$^{10}B/^{11}B$ isotopic ratio and atomic composition of boron carbide powders and sintered discs determined by PIGE (E_p =4.2 MeV).*

S.No.	Specimen	Physical state	B (at.%)	C (at.%)	$^{10}B : ^{11}B$
1	BC-P1	Powder	84.3 (80.7)	15.7	19 : 81
2	BC-P2		81 (80.7)	19.0	16.8 : 83.2
3	BC-S1	Sintered	83.6	16.4	68.2 : 31.8
4	BC-S2		81.9	18.1	68.4 : 31.6
5	BC-S3		81.6	18.4	68.5 : 31.5
6	BC-S4		80.5	19.4	19.4 : 80.6
7	BC-S5		81.3	18.6	19.5 : 80.5
8	BC-S6		81.7	18.2	18.6 : 81.4
9	BC-S7		80.5	19.4	19.5 : 80.5
10	BC-S8		75.0	24.9	19.8 : 80.2

4.3 EBS measurements

4.3.1 Experimental details

4.3.1.1 Materials

Some of the materials examined by PIGE were also investigated by EBS. The details of materials are described in detail in **Section 4.2.1**.1.

4.3.1.2 Proton beam irradiation

The EBS experiments were performed with 2.0 MeV protons. The beam diameter was about 1.5 mm while the beam current was about 5 nA. The beam was incident normally on the samples and the backscattered protons were collected by a passivated implanted planar silicon (PIPS) detector (**Chapter 2, Section 2.6.2.2**) positioned at a backward angle of 170°

at a distance of 100 mm from the targets. The entrance aperture of the detector was rectangular and measured 1.5 mm in width and 8 mm in length.

4.3.2 EBS: Results and Discussion

In addition to PIGE, the applicability of other ion beam analysis techniques using protons as projectiles was also explored in addressing the two analytical requirements. Nuclear reaction analysis (NRA) involving the $^{11}B(p,\alpha)2\alpha$ nuclear reaction that exhibits a strong but broad resonance at 660 keV is widely used for the determination of boron in a wide concentration range in several materials **[142].** However, the method is not applicable to the present analysis since it is specific to ^{11}B and hence does not provide any information on ^{10}B and the isotopes of carbon. In fact, care must be exercised while utilizing this method for the determination of total boron in materials since serious errors can creep in the analysis in case of enrichment in ^{10}B or ^{11}B isotope. In contrast to NRA, EBS is potentially more useful by virtue of its simultaneous multi-element (isotope) detection capability, higher sensitivity for light elements including boron and carbon and larger probing depths. **Fig.4.7** displaying the typical 2.0 MeV proton backscattered spectra of BC-P2 and BC-S1 specimens wherein the steps due to ^{10}B, ^{11}B and ^{12}C are distinctly distinguishable is a case in the point. The spectra also possess strong but broad peaks around 700 keV energy which, interestingly, differ significantly in terms of their widths for the powder and the sintered specimens. The steps are manifestations of $^{10}B(p,p)^{10}B$, $^{11}B(p,p)^{11}B$ and $^{12}C(p,p)^{12}C$ scatterings that exhibit enhanced cross-sections in comparison to the corresponding Rutherford cross-sections. The peaks, on the other hand, are due to the resonance at 1.734 MeV of the $^{12}C(p,p)^{12}C$ elastic scattering **[77]** . At the used proton beam energy the cross-section of $^{11}B(p,p)^{11}B$ elastic scattering is about 1.2-1.3 times higher than that of the $^{10}B(p,p)^{10}B$ one **[143,144]**. Therefore, the comparatively larger height of the step due to ^{10}B in **Fig.4.7** (d) points to, in consistency with PIGE results, the ^{10}B enriched composition of the specimen.

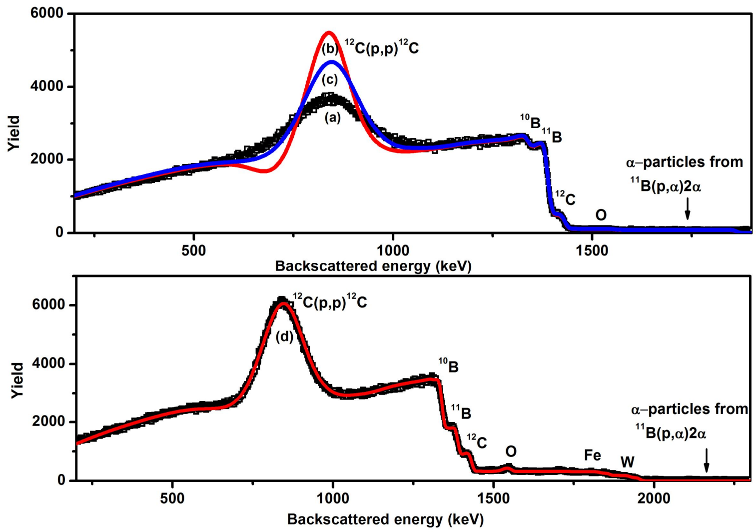

Fig.4.7: *(a) 2.0 MeV proton- elastic backscattered spectrum of boron carbide powder (BC-P2). Curves (b) and (c) are corresponding simulated spectra with roughness values of 100° and 400° respectively. Curve (d) displays the 2.0 MeV proton- elastic backscattered spectrum of sintered boron carbide (BC-S1). The solid curve overlapped on (d) is the corresponding simulated spectrum with a roughness value of 150°.*

The EBS spectra were simulated using SIMNRA (version 6.0) code **[103]** for determining the atomic composition of the specimen. The stopping cross-sections obtained by means of the Ziegler-Biersack- Littmark formulations were used in the simulations **[102]**. The simulation of EBS spectra, however, is non-trivial. Complications can arise due to inconsistency in data for the cross-sections of ^{10}B(p,p)^{10}B and ^{11}B(p,p)^{11}B elastic scatterings reported in literature **[77]**. The broad but strong peak due to the ^{12}C(p,p)^{12}C resonant elastic scattering is also a source of complexity. The difficulty in reproducing the experimental resonant peak of carbon has been articulated by several authors, for example, in reference **[132]** and is usually attributed to the limitations of SIMNRA in dealing with deeply buried resonances. Presently, we have utilized the scattering cross-sections of boron and carbon reported recently by Chiari et al. and Abriola et.al **[132,145]** respectively for simulating the spectra. The simulated curves are overlapped on the respective experimental data in **Fig.4.7**. A good agreement between the experimental and simulated spectra is witnessed for the sintered specimen, however, it is rather poor for the powder specimen with discrepancies being galore in the energy region of $^{12}C(p,p)^{12}C$ resonant scattering.

The simulation of the spectra requires some additional discussion vis a vis (a) alpha producing nuclear reactions involving ^{10}B and ^{11}B isotopes, and (b) the shape and width of the resonant peak of carbon. ^{10}B and ^{11}B isotopes undergo $^{10}B(p,\alpha)^{7}Be$ and $^{11}B(p,\alpha)2\alpha$ nuclear reactions simultaneously with the backscattering events with α-particles thus produced getting counted along with backscattered protons. For example, the counts in the energy region above ~1600 keV in **Fig 4.7 (a)** and above ~2000 keV in **Fig 4.7 (d)** are due to α-particles produced from the $^{11}B(p,\alpha)2\alpha$ nuclear reaction. These α-particles together with those produced from the $^{10}B(p,\alpha)^{7}Be$ reaction are present throughout the backscattered spectra. An apportioning of backscattered protons and α-particles is difficult due to the lack of data on the cross-sections of the reactions under the present experimental conditions of beam energy and detection geometry. However, as seen from the spectra, the counts per channel ascribable to α-particles are rather low which can be assumed to result in the formation of an ‘elevated baseline’. The absence of any extraneous feature attributable to events other than backscattering in the recorded spectra further points to the absence of any gross interference from α-particles. The difficulty in simulating the spectra arising from the α-particles was therefore circumvented by assuming the concentrations of impurities like oxygen, iron and or tungsten to be marginally higher than otherwise prevailing in the specimens. This approach, as can be seen from **Fig.4.7** led to a satisfactory simulation of the spectra.

So far as the $^{12}C(p,p)^{12}C$ resonant scattering is concerned, for a 2.0 MeV proton beam, the resonance occurs at a depth of about 8 μm in boron carbide. The large width of the peaks can result from the straggling of the incident beam in the underlying and that of the backscattered particles, in the overlying layers. However, straggling alone cannot explain the difference in the widths of the peaks belonging to the powder and the sintered specimens. In our opinion, the width of a resonant peak has contributions from (a) multiple scattering which result from roughness and (b) the density of the material with contributions from voids and or inclusions as well **[146-148]**. The compressed disc of powder boron carbide has pronounced roughness and low density which give rise to a significantly broadened resonant peak in **Fig.4.7 (a).** The sintered disc, on the other hand, has smoother morphology and is endowed with higher density as well. These lead to the formation of a resonant peak of relatively lower width in **Fig.4.7(d)**. Under this consideration, the width of the resonance peak can presumably serve as a qualitative measure of the roughness and density of the material. Following this supposition, a comparison of the resonant spectra (**Fig. 4.8**) suggests that the sample BC-S2 has the least roughness and/-or the highest density followed by BC-S1 and BC-S3. This deduction is in good agreement with the trend in the density of the materials (BC-S2: 2.37; BC-S1: 2.30; BC-S3: 2.26 gm cm^{-3}) measured geometrically. However, unfortunately, the influence of roughness and that of density cannot be differentiated. Thus, only roughness, an aspect comprehensively treated by SIMNRA, has been considered for spectral and quantitative analysis **[103]**.

The prevalence of roughness in the sintered specimens is substantiated by the larger widths of the resonance peaks of carbon in comparison to that of the peak obtained by simulating a smooth graphite target. The simulated curve in **Fig. 4.7(d)** is, in fact, obtained by invoking roughness during simulation. It must be emphasized that simulations performed without taking the cognizance of roughness did not describe the experimental data adequately. Interestingly, in conformation with our proposition, the roughness ascribed for realizing good simulation was the least for BC-S2 and the highest for BC-S3. So far as the powder specimen is concerned, reasonable fit could not be obtained notwithstanding the extent of roughness assumed for the target. These simulated curves for two significant roughness values are shown in **Fig. 4.7 (b)** and **(c)** for illustration.

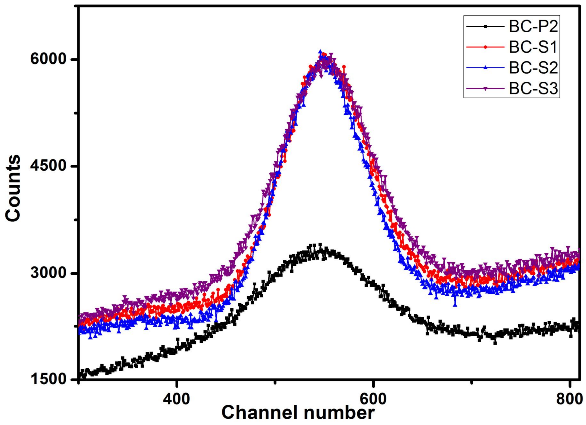

Fig.4.8: *$^{12}C(p, p)^{12}C$ resonant spectra for BC-P2 and BC-S1, BC-S2 and BC-S3 specimens acquired with 2.0 MeV proton.*

Table.4.5: *$^{10}B/^{11}B$ isotopic ratio and atomic composition of different boron carbide specimens and BC-20 determined by 2.0 MeV p-EBS.*

S.No.	Specimen	Boron (at.%)		Carbon (at.%)		$^{10}B : ^{11}B$
		Surface	Interior	Surface	Interior	
1	BC-S1	74.0	80.7	22.2	17.9	68 : 32
2	BC-S2	75.6	80.3	21.8	18.4	68 : 32
3	BC-S3	68.2	80.7	27.4	17.9	70 : 30
4	BC-P2	79.7		18.5		19.8 : 80.2
5	BC-20	81.7		17.0		19.8 : 80.2

The $^{10}B/^{11}B$ isotopic ratio and the concentrations of boron and carbon in BC-P2 , BC-20 and the three sintered boron carbide specimens determined using 2.0 MeV EBS are presented in Table 3. For BC-P2 and BC-20 in view of the rather poor agreement, the region of spectrum in the vicinity of the $^{12}C(p,p)^{12}C$ resonant scattering was excluded in the simulation. Importantly, in this condition simulation with and without any roughness yielded results well within the statistical uncertainty. However, for the sake of uniformity, the results in **Table 4.5** pertain to analysis performed by taking the roughness of the specimens into consideration.

4.4 Uncertainty in measurements

The combined uncertainty in the determination of the $^{10}B/^{11}B$ isotopic ratio is about 4% which has contributions from the cross-sections of $^{10}B(p,p)^{10}B$ and $^{11}B(p,p)^{11}B$ elastic scatterings. It is worth pointing out that unlike composition, the isotopic analysis by SIMNRA is not performed through an automatic iteration sub-routine and thus the method has a limited precision. Nevertheless, the isotopic ratios determined by EBS are in fair agreement with those determined by PIGE. Meanwhile, the combined uncertainty in the determination of the atomic composition is about 10% with contributions from the relevant scattering cross-sections and the stopping cross-sections of the elements. It can be observed that the atomic compositions of the powder ceramic determined by 2.0 MeV EBS are in good agreement with that obtained by PIGE.

The EBS measurements also show the presence of oxygen, iron and or tungsten (impurity elements) in the ceramic. But the most distinguishing aspect of the EBS measurements is the revelation of the prevalence of carbon-rich composition in the surface regions of the sintered discs. Such a region spans over a depth of about 500 nm for BC-S1 and BC-S2 and about 2 μm for the BC-S3 disc. These results are consistent with a previous report showing surface segregation of carbon in sintered boron carbide specimens **[149]**. Incidentally, as can be seen from the spectra in **Fig.4.7**, oxygen is also present in the top 500 nm region of the samples. The prevalence of carbon-rich composition (carbon content > 20 at.%) to a depth of about 2 μm in the BC-S3 disc can cause lower densification in the region which manifests in rather higher broadening of the carbon resonant peak in 2.0 MeV EBS spectrum of the ceramic. Thus the good agreement between data in **Table 4.4** and **Table 4.5** (interior) shows the utility of both PIGE and EBS in determining the composition of boron carbide, surface segregation of carbon in conjunction with the width of the resonance peak that can serve as a mean of providing information on roughness and or density of the material. Such information on sintered bodies is of high relevance in view of their widespread use as neutron absorbers in nuclear reactors.

The $^{13}C(p,p'\gamma)^{13}C$ nuclear reaction was also employed for the determination of Si/C ratio in thick SiC specimens. As can be seen from **Table 1.7**, Si emits 1778 keV prompt γ-rays through $^{28}Si(p,p'\gamma)^{28}Si$ nuclear reaction. The elemental composition of the SiC specimens was determined by making use of these two γ-rays at 4 MeV proton energy. The results are presented in **Table 4.6.**

***Table.4.6:** Composition of silicon carbide samples obtained by PIGE*

Sample	Si (at.%)	C (at.%)
Sample A	51.4	48.6
Sample B	46.5	53.5

1.5 Conclusions

The isotopic ratio of boron and the elemental composition of boron carbide can be determined by PIGE by means of the $^{10}B(p, \alpha\gamma)^{7}Be$, $^{10}B(p, p'\gamma)^{10}B$ and $^{11}B(p, p'\gamma)^{11}B$ and $^{13}C(p,p'\gamma)^{13}C$ nuclear reactions with an uncertainty of about 2% and 5% respectively. The analysis is best accomplished with 4.0-4.2 MeV protons in irradiations lasting for about 3h at 2-3 nA beam current. Strong but easily identifiable interferences can arise from Li in the measurements. The analysis can also be performed by 2.0 MeV EBS with an uncertainty of <10%. The methods are non-destructive and applicable to both powders and sintered specimens. EBS can also be useful in predicting roughness and density of the sintered ceramics. The non-destructive nature and analytical potential make the methods suitable alternatives to chemical methods wherein the dissolution of the ceramic is difficult due to its pronounced chemical stability and high hardness.

Chapter 5

Determination of Bulk Oxygen in Binary, Ternary and Multinary Oxides

5.1 Introduction

The determination of oxygen has long been a subject of interest due to the profound influence of the element on the properties of materials **[150,151]**. The materials can be thin films or bulk compounds wherein oxygen prevails either as a major constituent or as an impurity element. Amongst the several different methods of oxygen determination, ion beam analysis (IBA) holds an important position by virtue of its non-destructive nature and versatility. An account of the capabilities of IBA for oxygen determination is exquisitely presented in a review article published by Cohen and Rose in early nineties **[152]**. The IBA methods, by taking cognizance of their probing depths, can be subsumed into two broad categories: those suitable for the determination of surface oxygen and those applicable for 'bulk' oxygen determination. Techniques such as nuclear reaction analysis (NRA), Rutherford backscattering spectrometry (RBS) and 3.05 MeV $^{16}O(\alpha,\alpha)^{16}O$ resonant scattering have a probing depth of a few microns and, therefore, have been extensively used for the determination of oxygen in films and in the surface regions of bulk materials **[153-155]**. In fact, $^{16}O(\alpha,\alpha)^{16}O$ resonant scattering with a detection sensitivity of ~ 1 at% and a depth resolution of ~ 30 nm, is the most popular method of depth profiling oxygen in materials **[156]**. So far as nuclear reaction analysis (NRA) is concerned, $^{16}O(d,p)^{17}O$, $^{16}O(^{3}He,p)^{18}F$ and $^{18}O(p,\alpha)^{15}N$ are some of the prominent reactions that are often employed for the determination of oxygen **[152].** These reactions are, in fact, useful for probing only thin films or, at the best, the top few microns of thick targets since the measurements entail the detection of particle ejectiles.

Methods based on particle induced γ-ray emission (PIGE), on the other hand, have probing depths up to several tens of μm and therefore provide the determination of 'bulk oxygen' in materials. But the instances of the applications of these methods are far and few. In probably one of the most exemplary applications, Vickridge et al. used PIGE for the precise determination of oxygen in high temperature superconductors. In fact, the measurement was accomplished by the $^{16}O(d,p\gamma)^{17}O$ nuclear reaction (E_{γ}= 871 keV) and therefore, the authors referred to the method as the deuteron induced gamma emission (DIGME) technique **[157,158].** Oxygen can also be determined by PIGE by means of $^{16}O(p,\gamma)^{17}F$, $^{17}O(p,p\gamma)^{17}O$ or $^{18}O(p,p\gamma)^{18}O$ nuclear reactions that emit 495, 871 and 1982 keV characteristic γ-rays respectively **[81]**. Use can also be made of $^{16}O(p,p\gamma)^{16}O$ nuclear reaction wherein the measurement is based on the detection of 6-7 MeV γ-rays.

This chapter dwells on the methodologies developed for the routine determination of bulk oxygen in materials which, as stated earlier, has not received much attention despite its immense importance. The $^{16}O(d,p\gamma)^{17}O$ nuclear reaction, though possessing excellent analytical attributes, has limited applicability in view of the fact that deuterons are prolific neutron producers and laboratories operating deuteron beams must have adequate shielding against neutrons. The $^{16}O(p,p'\gamma)^{16}O$ nuclear reaction, on the other hand, has several limitations. For example, (a) it occurs only above 6.8 MeV proton energy which precludes the use of low energy accelerators and (b) it suffers nuclear interference from $^{19}F(p,\alpha\gamma)^{16}O$, one of the most sensitive nuclear reactions for fluorine **[159]**. The likelihood of a significant neutron production at 6.8 MeV or higher proton energy from nuclear reactions involving the other constituents of the target is yet another drawback of the method. Therefore, the $^{16}O(p,p'\gamma)^{16}O$ nuclear reaction is not a favourable choice for routine applications.

Presently two methodologies have been developed and standardized for the determination of bulk oxygen in materials. The first method is based on $^{18}O(p,\alpha\gamma)^{15}N$ nuclear reaction at 3.2 MeV or higher proton energies and involves the measurement of 5.27 MeV γ-rays, characteristic of the reaction. It is important to note that while $^{18}O(p,\alpha)^{15}N$ nuclear reaction, as stated earlier, is often employed for the analysis, depth profiling in particular, of oxygen by way of α-detection, there is no previous report, to the best of our knowledge, on the application of $^{18}O(p,\alpha\gamma)^{15}N$ nuclear reaction for oxygen determination **[160,161]**.

The second approach is based on $^{18}O(p,p'\gamma)^{18}O$ nuclear reaction that emits 1982 keV γ-rays. Although the thick target yields of the γ-rays have been measured on a few occasions, the analytical capability of the reaction has not been comprehensively probed **[159,81]**. Presently, continuing our endeavor to devise simple yet effective methodologies for oxygen determination, we have carried out a systematic investigation on the analytical potential of the $^{18}O(p,p'\gamma)^{18}O$ nuclear reaction which involved (a) the measurement of thick target yields of 1982 keV γ-rays in the 3.0-4.2 MeV proton energy range, (b) an assessment of analytical features such as limit of detection and probing depth and (c) the identification of sources of interferences. The applicability of the method was evaluated by analyzing several binary, ternary and multinary oxides. The compounds examined included lithium titanate and lithium iron phosphate which are important energy materials. It is shown that with the feasibility of oxygen determination, PIGE, by virtue of its simultaneous multi-element detection capability can enable the determination of the overall atomic composition of these compounds in a single measurement.

5.2 Experimental details

5.2.1 PIGE Measurements

5.2.1.1 Materials

The oxide powders (described in **Chapter 2, section 2.2.)** were homogeneously mixed with 25 wt.% high purity graphite powder and the resulting mixtures were pressed into 20 mm diameter discs which served as targets. A similarly made disc containing calcium carbonate (75 wt.%) and high purity graphite (25 wt.%) was used for the determination of thick-target yields and also as a standard for quantification. All compounds were of analytical grade and contained oxygen in natural isotopic proportions. The homogeneity of the mixtures was ascertained by measuring the yields of 1982 keV γ-rays at a particular proton beam energy at different locations on the targets.

5.2.1.2 Proton beam irradiation

The PIGE experiments were conducted with a 3.0-4.2 MeV proton beam (Φ ~ 3 mm). Depending on the nature of the matrix, the proton beam current during irradiation ranged from 3 to 50 nA; the lighter matrices were irradiated with lower beam currents while the heavier matrices, with higher beam currents. The duration of the measurements varied accordingly; it ranged from ~45 minutes (heavier matrices) to ~90 minutes (light matrices).

5.2.1.3 Acquisition of γ-ray spectrum

The prompt γ-rays emitted from the nuclear reactions were measured with a HPGe and also with a BGO detector placed in air outside the scattering chamber in a 2.5 cm thick cylindrical lead shield. The measurements were carried out at 0° and 90° angles with respect to the direction of the beam. The experimental conditions were identical for the samples and the standard. The spectra were acquired in 4K channels using a 8K MCA and were calibrated using 356 keV ^{133}Ba, 661.7 keV ^{137}Cs, 1332.5 keV ^{60}Co and 2614.5 keV ^{208}Tl γ-rays, and 4.44 MeV and 6.13 MeV γ-rays from ^{15}N(p,αγ)^{12}C and ^{19}F(p,αγ)^{16}O nuclear reactions respectively. The data were acquired for integrated beam charges sufficient to produce statistically significant counts-per-channel.

5.2.2 Proton elastic backscattering spectrometry (p-EBS) Measurements

In addition to PIGE, the specimens of lithium titanate and lithium iron phosphate were also analysed by p-EBS. The experiments were performed with 1.5 or 2.0 MeV protons in another scattering chamber maintained at ~ 5×10^{-6} torr pressure. The samples were in the form of 10 mm diameter discs prepared by pressing the compounds without any additive i.e.

graphite. The beam diameter was about 1.5 mm while the beam current was about 5 nA. The beam was incident normally on the samples and the backscattered protons were collected by a Si surface barrier detector positioned at a backward angle of 165(±0.3)°. The atomic composition of the compounds was determined by simulating the experimental data using SIMNRA **[103].** Since the scattering of 1.5-2.0 MeV protons from lithium, carbon or oxygen is non-Rutherford, the experimentally determined differential cross-sections of ^{6}Li(p,p)^{6}Li, ^{7}Li(p,p)^{7}Li, C(p,p)C and O(p,p)O scatterings were used in the simulations **[162-165]**. In fact, the cross-sections for the ^{6}Li(p,p)^{6}Li scattering reported in reference **[162]** are for 164° angle but were used for simulations due to the absence of the data for the scattering at 165° angle under the premise that the cross-sections at the two angles are not significantly different. Furthermore, any discrepancy in the overall atomic composition arising from the application of the data at 164° angle is expected to be marginal since the compounds contain Li in natural isotopic abundance. Incidentally, Rutherford scattering cross-sections at relevant energies were used for P, Ti and Fe for simulations.

5.3 Oxygen determination in materials by ^{18}O(p,αγ)^{15}N nuclear reaction

5.3.1 Origin of 5.27 MeV γ-rays

A high energy segment of the prompt γ-ray spectrum recorded by HPGe detector while bombarding the $CaCO_3$ target (standard) with 4.0 MeV proton beam is shown in **Fig.5.1**(a). It consists of a prominent peak at 5.27 MeV which is a full energy peak and two other strong peaks at about 4.7 and 4.2 MeV which are the single and double escape peaks respectively. Similar spectra were recorded on irradiating the target with 3.0-4.2 MeV proton beam but the one obtained using 2.5 MeV proton was devoid of these peaks. The peak at 5.27 MeV is attributed to the γ-rays emitted from ^{18}O(p,αγ)^{15}N nuclear reaction and as is evident from the energy level scheme of ^{15}N nucleus depicted in **Fig.5.2**, it corresponds to the transition from the first excited state (J= $5/2^{+}$) to the ground state (J= $1/2^{-}$) of the nucleus

[126]. The excitation to various energy levels, in general, depends on the excitation energy of the products which is determined largely by the Q-value of the reaction and incident beam energy. The diagram in **Fig.5.3** summaries the energetics of the present reaction that proceeds with the formation of ^{19}F compound nucleus. It clearly shows that at 4.0 MeV proton energy, the energetics of the reaction is favourable for populating the first excited state of ^{15}N nucleus.

Expressing more explicitly, $^{18}O(p,\alpha\gamma)^{15}N$ reaction that is characterized by a Q value of +3.98 MeV and Coulomb barrier of 3.18 MeV for the entry channel, can be assumed to take place in two successive steps i.e. (i) the formation the compound nucleus (^{19}F) via ^{1}H + $^{18}O\rightarrow$ ^{19}F reaction and (ii) the decay of the compound nucleus into products via $^{19}F\rightarrow$ ^{4}He + ^{15}N reaction. The excitation energy (E_x) of a compound nucleus formed in a nuclear reaction is given by the expression

$$E_x = \frac{M_2}{M_1 + M_2} E_0 + Q \qquad (5.1)$$

where E_0 is the incident beam energy and M_1 and M_2 are the masses of the projectile and target nuclei respectively. Accordingly, the E_x of ^{19}F nucleus at E_0= 4.0 MeV is 11.7835 MeV with the Q value of the first step being +7.994 MeV. Meanwhile the Q value of the second step is –4.0138 MeV. Hence the total excitation energy of the products (^{4}He + ^{15}N) is 7.7697 MeV. The emission of α-particles from the compound nucleus may leave the residual ^{15}N nucleus in the ground state or in the first/ second excited states. In the former condition, α-particles with about 7.2 MeV will be emitted in the direction of the beam, while the later will cause the emission of 5.27 MeV or higher energy γ-rays accompanied with about 2.0 MeV α-particles. These considerations suggest that the total excitation energy of the products should at least be about 5.27 MeV for populating the first excited state of the ^{15}N nucleus.

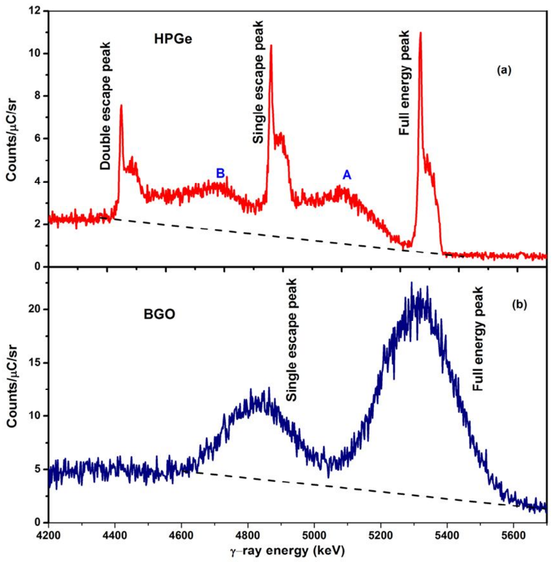

Fig. 5.1: *Prompt γ-ray spectrum of a target consisting of 75 wt.% $CaCO_3$ and 25 wt.% high purity graphite recorded at 90° with (a) HPGe and (b) BGO detectors. The incident beam energy is 4 MeV. The dashed lines represent the linear background while the labels 'A' and 'B' in* ***Fig.5.1*** *(a) represent the Compton edges of 5.27 MeV γ-rays and the single escape peak respectively.*

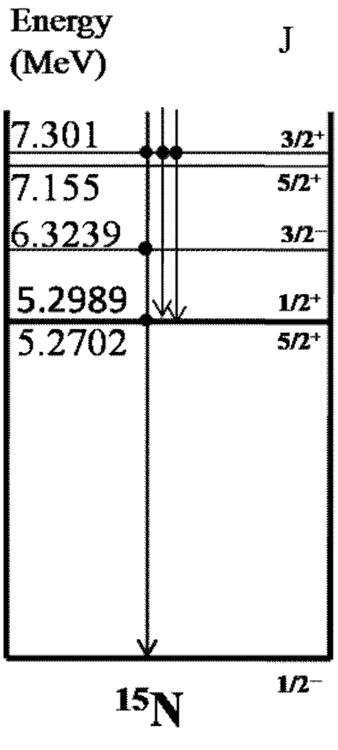

Fig. 5.2*: Energy level scheme of ^{15}N nucleus*

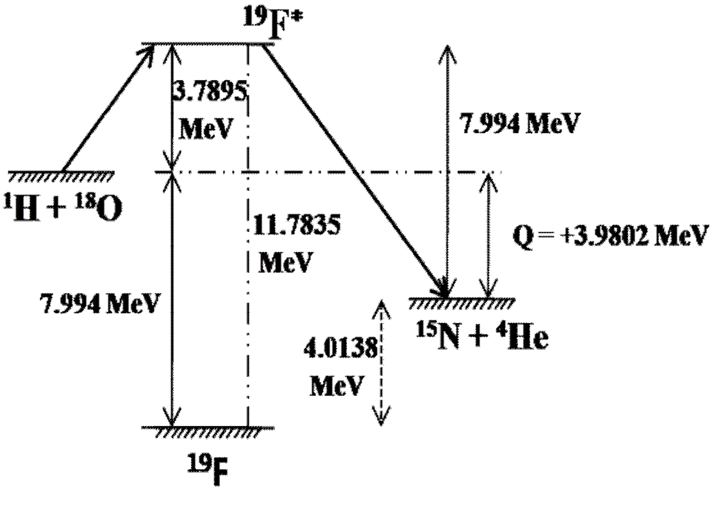

Fig.5.3: *A schematic representation of energetics involved in $^{18}O(p,\alpha\gamma)^{15}N$ nuclear reaction. The proton beam energy is 4 MeV*

In other words, the emission of 5.27 MeV γ-ray is possible only above about 1.5 MeV proton energy. But it should not be construed as the minimum proton energy required for initiating $^{18}O(p,\alpha\gamma)^{15}N$ nuclear reaction since the emitted α-particles must have sufficient energy to cross the Coulomb barrier for the exit channel that measures about 5.0 MeV. Simple calculations show that for cases wherein (a) the incident energy is about 1.0 MeV or higher and (b) the residual ^{15}N nucleus is left directly in the ground state, the emitted α-particles have sufficient energies (i.e. $\geq$ 5.0 MeV) to surmount the Coulomb barrier. But for proton energies used presently, the α-particles have $\leq$2.5 MeV energy if the residual ^{15}N nucleus is left in the first excited state which is rather inadequate for surmounting the Coulomb barrier of 5 MeV height. Therefore it can be surmised that α-particles accompanying the 5.27 MeV γ-rays penetrate the Coulomb barrier and not surmount it during emission. Similar situation prevails while depth profiling oxygen by the resonance at 163 or 629 keV in $^{18}O(p,\alpha)^{15}N$ reaction.

It is worthwhile mentioning that ^{15}N nucleus can also be formed as a result of $^{16}O(p,2p)^{15}N$ nuclear reaction. The Q value of the recation is –12.12 MeV and thus it cannot be initiated by the proton beam energies (2.5–4.2 MeV) presently employed. It is equally important to note that 5.27 MeV γ-rays are emitted from the de-excitation of ^{15}O nucleus as well. However, the reaction $^{16}O(p,pn)^{15}O$ that can lead to its formation too has a large negative Q (–15.663 MeV) value. Meanwhile $^{19}F^{*}$ nucleus, formed as result of $^{18}O(p,\gamma)^{19}F$ reaction, represents yet another possible source of γ-rays of about 5.3 MeV energy and therefore it is instructive to examine its likely contribution within the framework of present experimental conditions. A perusal of the energy level scheme of ^{19}F shows that $^{19}F^{*}$ nuclei de-excite to ground state through the emission of 2.58, 5.210, 5.28 and 6.3 MeV γ-rays **[126]**. However, except 5.27 MeV γ-rays, none of these were observed in the spectra recorded using

2.5-4.2 MeV protons. Thus it can be inferred that the 5.27 MeV γ-rays observed presently do not have their origin in $^{18}O(p,\gamma)^{19}F$ reaction. This inference gets credence from the fact that there is no perceptible signal of 5.27 MeV γ-rays in spectra recorded at E_p = 2.5 MeV which is unlikely had $^{18}O(p,\gamma)^{19}F$ reaction been contributing considering the fact that its Q value is as high as +7.964 MeV. The absence of 5.27 MeV γ-rays at E_p = 2.5 MeV, in fact, points to the non-occurrence of $^{18}O(p,\alpha\gamma)^{15}N$ reaction. This is apparently due to the reason that the α-particles have too less (~1 MeV) energy to penetrate the Coulomb barrier with the simultaneous emission of 5.27 MeV γ-rays.

5.3.2 Analytical capabilities of the $^{18}O(p,\alpha\gamma)^{15}N$ reaction

5.3.2.1 Thick target yields and limits of detection

In order to ascertain the efficacy of this reaction in the determination of oxygen, yields of 5.27 MeV γ-rays were measured in 3.0-4.2 MeV proton energy region using $CaCO_3$-graphite discs containing 38.57 at. % oxygen as thick targets. The measurements were made with HPGe and BGO detectors at 0° as well as 90° angles (with respect to the direction of the beam) in 100 or 200 keV proton energy intervals.

An important feature of the high resolution γ-ray spectrum in **Fig.5.1**(a) not discussed previously, is the presence of a broad structure at about 5.30 MeV that has its single and double escape components as well that precede the peaks at 4.7 and 4.2 MeV respectively. The ^{15}N nucleus, as shown in the energy level scheme in **Fig.5.2**, has second excited state with E_x = 5.3 MeV. The 5.3 MeV γ-rays are emitted as a result of transitions involving the second excited state and the ground state of the ^{15}N nucleus. Warburton et al. have also observed both 5.27 and 5.30 MeV γ-rays from $^{18}O(p,\alpha\gamma)^{15}N$ reaction in experiments conducted at E_p=8.925 MeV **[166]**. The broader structure of the 5.30 MeV γ-ray peak is due to Doppler broadening caused by the shorter lifetime (25 fs) of the second excited state **[135]**.

Since the effect is a function of the cosine of emission angle, comparatively lower broadening of peaks is observed in the spectra acquired at 90° angle. For example, at E_p = 4.0 MeV, the width of the peak in the spectrum recorded at 90° angle is ~ 25 keV less in comparison to the width of the peak in the spectrum collected at 0° angle. Meanwhile, it is important to note that while the axes of the detectors lie at 0° or 90° angle with respect to the direction of the beam, the point of interaction (i.e. beam spot) subtends, due to the finite size of the detectors, about ±20° or 70°/110° respectively at their extremities. As a result, substantial broadening is observed in spectra recorded even at 90° angle. Incidentally, there is no perceptible Doppler broadening of 5.27 MeV γ-rays which can be ascribed to the fact that the first excited state has much longer lifetime, ~ 2.58 ps, and the nucleus keeps on emitting 5.27 MeV γ-rays even after coming to rest **[135]**.

Fig.5.1(b) shows a typical prompt γ-ray spectrum, in the relevant energy region, recorded with BGO at E_p= 4.0 MeV. Two important differences between the features of HPGe and BGO spectra can be immediately discerned: (1) the peaks in the BGO spectrum are broader and (2) the BGO spectrum is bereft of the double escape peak present conspicuously in the HPGe spectrum. The former is a manifestation of the poor energy resolution of the BGO detector while the later is the result of the larger size and higher density (7.13 gcm^{-3}) of the bismuth germanate crystal. In fact, due to poor energy resolution, the Doppler broadened 5.30 MeV γ-ray peak prevailing in the HPGe spectrum is not observed in the BGO spectrum. In view of the spectral differences, the energy window (4.20-5.85 MeV or 4.20-5.35 MeV for measurements at 0° and 90° angles respectively) encompassing the high energy component, the full energy peak and the two escape peaks was taken into consideration for yield calculations for HPGe spectra while for BGO spectra the energy window (4.5-5.65 MeV) spanning over the full energy peak and the first escape peak served the purpose. The nature of the background is an important consideration in yield calculations.

The peaks in spectra in **Fig.5.1** are situated on a background significantly different from that prevailing in low γ-ray energy region. Similar elevated baseline is observed in the spectra of 4.43 MeV or 6.12 MeV γ-rays from $^{15}N(p,\alpha\gamma)^{12}C$ and $^{19}F\ (p,\alpha\gamma)^{16}O$ reactions respectively **[167].** The background in **Fig. 5.1**(a) arises primarily due to Compton scattering. The structure, marked 'A' in the figure corresponds to the Compton edge of the 5.27 MeV γ-rays while another, marked 'B' (between the single and double escape peaks) is the Compton edge of the single escape peak. Moreover, the baseline has contributions from multiple scatterings of the 5.27 MeV and 511 keV γ-rays as well. The prevalence of such Compton edges is reported in the HPGe spectrum of 6.13 MeV γ-rays emitting from ^{16}N isotope **[168]**. Some other factors such as the structure of the nucleus involved in the emission (i.e. ^{15}N), the kinematics of the reaction, the characteristics of the detector and the nuclear reactions involving other elements constituting the matrix may also contribute to the baseline. The response function of a detector describing the shape (including the baseline) of the γ-ray spectrum can be simulated using computer codes **[167,168]**. In view of the absence of such a code at the moment, for the sake of simplicity, the peak areas were calculated after subtracting linear background (shown as dashed lines in **Fig.5.1**) from the integrated counts in the energy window of interest. However it is worthwhile mentioning that certain ambiguity prevails in literature on the peak area calculation of high energy γ-rays, for example, 6-7 MeV γ-rays from $^{19}F(p,\alpha\gamma)^{16}O$ nuclear reaction. There are several instances wherein the method of peak area determination is not mentioned explicitly leading one to assume that the natural radiations are the only or predominant source of background. Incidentally, the natural background count rates for HPGe and BGO detectors were 0.026 and 0.068 counts /s respectively during the present study and are significantly lower than the prevailing background.

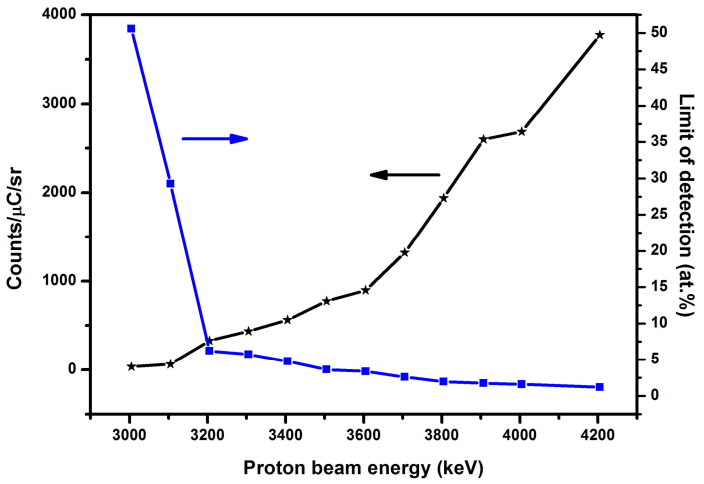

***Fig. 5.4**: Thick target yields of 5.27 MeV γ-rays emitted from $^{18}O(p,\alpha\gamma)^{15}N$ nuclear reaction induced in a target consisting of 75 wt.% $CaCO_3$ and 25 wt.% high purity graphite by 3 – 4.2 MeV protons. The yields are measured at 0° angle with BGO. The figure also shows the limits of detection calculated at different beam energies.*

Fig.5.4 shows the γ-ray yields extracted from the relevant BGO spectra recorded at 0° angle for the target under consideration for E_p = 3.0-4.2 MeV. The yields refer to peak areas normalized to the integrated charge and the solid angle. It is important to note that peak areas were not normalised to the absolute efficiencies of the detectors since their values for high energy γ-rays are not known precisely. The figure shows a monotonous increase in yield with proton beam energy. Notably, the yields for measurements performed at different locations were constant within 5% indicating the uniformity of the target as well as its stability under beam irradiation. The combined uncertainty in thick target yields for measurements on a particular location of the target at a beam energy, for example, 3.8 MeV is about 3%. It is calculated by adding in quadrature the uncertainties associated with peak area (2%), integrated charge (2%) and solid angle (1%). A comparison of γ-ray yields (charge and solid angle normalized) obtained under different experimental conditions showed that the yields with BGO, in consistency with its higher efficiency, are higher as compared to those obtained with HPGe detector. It is very well illustrated by **Table 5.1** that lists the thick target yields for

BGO and HPGe at 3.8-4.2 MeV proton energies. It is seen that the γ-ray yields at 90° are less, more noticeably for HPGe, as compared to those at 0° angle.

***Table 5.1**: Normalised 5.27 MeV γ-ray yields and limits of detection(LOD) for HPGe and BGO detectors at 0° and 90° detection angles∗*

Energy (MeV)	Angle	Detector			
		HPGe		BGO	
		Normalised yield (counts/μC /sr)	LOD (at.%)	Normalised yield (counts/μC /sr)	LOD (at.%)
3.8	0°	874	3.1	1937	1.9
	90°	786	3.8	1928	1.9
4.0	0°	1235	2.6	2688	1.7
	90°	1128	3.3	2683	1.7
4.2	0°	1648	2.4	3772	1.3
	90°	1616	2.5	3763	1.3

Target--- Disc composed of 75 wt.% $CaCO_3$ and 25 wt.% high purity graphite

5.3.2.2 Limits of detection

Fig.5.4 also shows the limit of detection (LOD) of the method for the measurements at several proton energies with BGO at 0° angle. The LOD was calculated on the basis of three times the standard deviation of background in the energy region of interest. LODs were also calculated for measurements conducted with BGO at 90° angle and with HPGe at both 0° and 90° angles but are not included in the figure for the sake of clarity and brevity. Nevertheless, their values at some selected beam energies are presented in **Table 5.1** for illustration. In terms of comparison, the best LOD of ~ 1.3 at.% realized with BGO (and ~ 2.5 at.% with HPGe) at 0°/90° angles at E_p=4.2 MeV, is superior to that achieved by backscattering spectrometry. In fact, the detection capabilities of the two techniques are very sensitive to the nature of matrix. For example, the detection sensitivity of α-RBS to oxygen worsens to about 20 at.% from about 5 at.% with a mere increase in atomic number of the matrix from 10 to 20. It becomes still poorer in high Z matrices. On the other hand, unlike RBS the sensitivity of the present method does not vary systematically with the atomic number of the matrix. The LOD for matrices containing U, W or La as major elements was found to be nearly similar to that (i.e. ~1.3 at. %) as estimated using calcium carbonate as a target. However, it was estimated to be 5.9, 3.7, 3.5 and 3 at.% for Ti, Fe, Zr and Nb respectively. These were determined by irradiating the respective metal foils with 4.2 MeV proton. Though no measurements were performed, LOD is expected to be still higher in matrices composed of light elements such as Li, B, F and Na that are sensitive to PIGE and or produce high energy prompt γ-rays on proton irradiation. So far as other PIGE methods are concerned, the $^{16}O(p,p\gamma)^{16}O$ reaction has comparable LOD, while $^{16}O(d,p\gamma)^{17}O$ reaction has better limits of detection **[159,157]**. However, as mentioned earlier the former reaction requires medium or high energy accelerators, while the latter requires adequate shielding against neutrons since deuterons are prolific neutron producers.

5.3.2.3 Probing depths and interferences

Probing depth is an important aspect of an IBA method. $^{18}O(p,\alpha\gamma)^{15}N$ reaction has a probing depth of about 60 µm in SiO_2 and about 30 µm in UO_2 at E_p= 4.2 MeV considering that the reaction commences at E_p = 3.0 MeV. Although the probing depth of the reaction is lower than that of $^{16}O(p,p\gamma)^{16}O$ reaction (~ 50 µm in UO_2), but is significantly higher than that of backscattering spectrometry which, at best, is only a few microns. Therefore this method can be conveniently employed for the determination of bulk oxygen in materials.

Interferences have an important bearing on the quality of an analytical result and thus need to be carefully assessed. $^{19}F(p,\alpha\gamma)^{16}O$ reaction that emits 7.1, 6.9 and 6.1 MeV γ-rays can be a major source of interference in the present method. It is abundantly clear from **Fig.5.5** (a) that shows the high resolution γ-ray spectrum of a tungsten oxide powder which contains fluorine (precise concentration not known) as an impurity. The main interference herein arises from the double escape peak (at about 5.1 MeV) of 6.1 MeV γ-rays. Though its contribution can be ascertained in a high resolution spectrum, the same is not possible in a spectrum recorded with BGO and thus an overestimation of oxygen is expected. It is important to note that since $^{19}F(p,\alpha\gamma)^{16}O$ reaction has high cross-section, the presence of fluorine even at 0.1 wt.% level in a specimen may cause high background in the vicinity of 5 MeV γ-ray region which would seriously impair the detection capability of the $^{18}O(p,\alpha\gamma)^{15}N$ reaction. Though of not direct relevance to the present study, these considerations suggest that $^{18}O(p,\alpha\gamma)^{15}N$ reaction can interfere in the determination of fluorine impurity by $^{19}F(p,\alpha\gamma)^{16}O$ reaction in oxides. However, it can be minimized by considering only the full energy peak at 6.1 MeV and or the single escape peak. Similar interference is anticipated in the determination of oxygen by $^{16}O(p,p\gamma)^{16}O$ reactions. In addition to $^{19}F(p,\alpha\gamma)^{16}O$ reaction, interferences can also arise from $^{15}N(p,\alpha\gamma)^{12}C$ reaction that emits 4.4 MeV γ-rays. However, the extent of interference is significantly less as ^{15}N has very low (0.37%) natural isotopic abundance. It is amply demonstrated by the high-resolution γ-ray spectrum in **Fig. 5.5 (b)** of a nitrogen salt containing about 30% enriched ^{15}N isotope. It is instructive to mention at this juncture that the broader structure of the full energy, single and double escape peaks of the 7.1 and 6.9 MeV γ-rays in **Fig. 5.5(a)**, and 4.4 MeV γ-rays in **Fig.5.5(b)** is, as witnessed for 5.30 MeV γ- ray peak in **Fig. 5.1(a)**, due to Doppler broadening induced by the shorter lifetimes of the levels involved. For example, the lifetimes of the third and second excited states of the ^{16}O nucleus involved in the emission of 7.1 MeV and 6.9 MeV γ-rays are 7 and 8 fs respectively **[76]**. Similarly, the lifetime of the first excited state of the ^{12}C nucleus measures 40 fs.

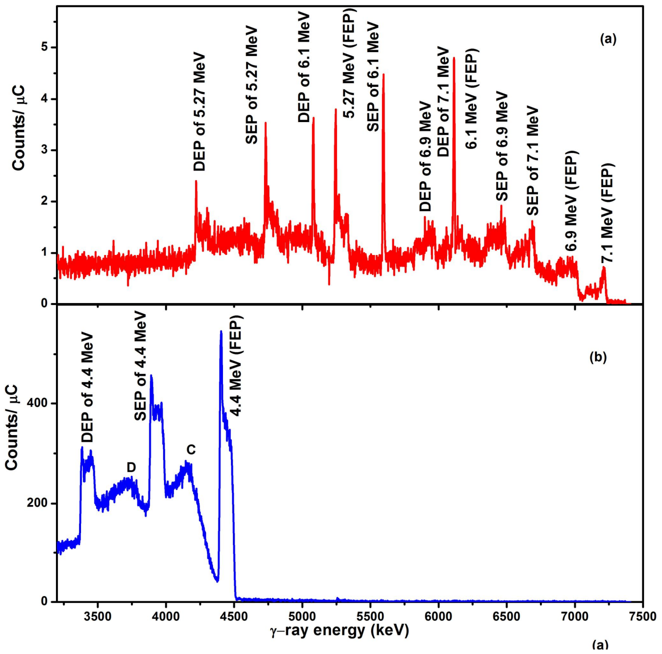

***Fig. 5.5**: (a) γ-ray spectrum of a tungsten oxide powder sample recorded with HPGe at 4.0 MeV proton energy. The 5.27 MeV γ -rays are emitted from $^{18}O(p,\alpha\gamma)^{15}N$ nuclear reaction. The single escape peak (SEP) and double escape peak (DEP) of the full energy peak (FEP) of 5.27 MeV γ -rays are also indicated. The 6.1, 6.9 and 7.1 MeV γ -rays are emitted from $^{19}F(p,\alpha\gamma)^{16}O$ nuclear reaction. The respective SEP and DEP of these γ-rays are also indicated. The FEP of 6.1 MeV γ-rays and the DEP of 7.1 MeV γ-rays have nearly identical energies. (b) γ-ray spectrum of a NH_4Cl target enriched with 30% ^{15}N isotope recorded with HPGe at 4.0 MeV proton energy. The 4.4 MeV γ-rays are emitted from $^{15}N(p,\alpha\gamma)^{12}C$ nuclear reaction. The SEP and DEP of 4.4 MeV γ-rays are also indicated. The labels 'C' and 'D' represent the Compton edges of 4.4 MeV γ-rays and the single escape peak respectively.*

5.3.3 Quantification and analysis of samples

The analytical proficiency of this method was ascertained by analysing several materials that included oxides of well-established composition. The content of oxygen (C, at.%) was calculated using the equation

$$C_{samp} = \frac{Y_{samp} \times C_{std} \times \varepsilon_{samp}}{Y_{std} \times \varepsilon_{std}} \qquad (5.2)$$

where *samp* and *std* refer to sample and the standard respectively, Y is the yield (counts/μC/sr) of γ -rays and ε is the stopping cross-section (eV/10^{15} at. /cm^2) of a specimen at the incident beam energy. The values of ε were obtained using SRIM-2013 **[102]**. Two different approaches were employed to calculate the yields of the γ-rays from the recorded spectra. In the first approach, the yield was obtained after the subtraction of appropriate natural background from the integrated counts in the energy window of interest while in the second, after the subtraction of linear background. The contents of oxygen in compounds determined using yields calculated by the two approaches are compared in **Table 5.2**. Notably the second approach of yield calculation gives comparatively higher values for all compounds except zirconium oxide. The overestimation is caused by comparatively higher background for the standard which results in larger reduction in its integrated counts in comparison to the samples on the subtraction of the linear background. As a consequence, the ratio of yields of sample to standard is more for the second approach and hence higher (ca. **equation(5.2)**) values. On the other hand, the significant overestimation of oxygen in zirconium oxide when the first approach is used for yield calculation can be due to a rather larger production of high energy prompt γ-rays from Zr (which is also indicated by poor LOD) on irradiation with proton.

There is a close agreement between the measured and the reference concentrations of oxides (**Table 5.2**). Except zirconium oxide, the agreement is better for concentrations determined using integrated counts as yields (i.e. first approach). The agreement between the values is within 5%. In fact, better agreement is achieved for matrices that have background comparable with that of the standard. However, serious errors can creep in, as observed for zirconium oxide, in the case of an extraneous background. The second approach is very useful under such circumstances: it not only furnishes reliable data but also helps to ascertain interferences which otherwise are difficult to discern. In order to cross-validate the data, the concentrations of oxygen in the compounds were also determined by $^{18}O(p,p\gamma)^{18}O$ (E_γ = 1982 keV) nuclear reaction and are listed in Table 5.2. A fair agreement is observed between the values that further lends credence to the accuracy of present methods of analysis.

***Table 5.2**: Concentration of oxygen in oxides determined by $^{18}O(p,\alpha\gamma)^{15}N$ nuclear reaction*

Oxide	Reference (at.%)	Determined (at.%)		Determined (at.%) $^{18}O(p,p\gamma)^{18}O$
		Integrated	Background subtracted	
Silicon dioxide	66.7	68.5[a]	70.1[a]	64.0
Dysprosium oxide	60.0	62.0[b]	63.0[b]	62.1
Lanthanum oxide	60.0	60.3[b]	64.0[b]	64.3
Zirconium oxide	66.7	79.8[c]	70.6[c]	63.3
Tungsten oxide	-	65.0[c]	65.1[c]	68.3
Uranium oxide	-	64.4[a]	65.7[a]	-

a → 3.8 MeV/BGO/0°; b → 4.2 MeV/HPGe/0° and c → 4.0 MeV/HPGe/0°

To further explore the scope of application, the method was employed to determine oxygen present in materials at low levels or as an impurity. In this context, the analysis of metal sulphide powders needs particular mention. The content of oxygen in such materials which included tin sulphide, indium sulphide and copper sulphide, ranged from 5 to 20 at.%. These materials were synthesized by wet-chemical methods and were left exposed to laboratory atmosphere for different durations. In general, sulphides are not amenable to oxygen analysis by $^{18}O(p,p\gamma)^{18}O$ nuclear reaction due to the fact that 1982 keV γ-rays are interfered by the Compton edge of 2230 keV γ-rays emitted from $^{32}S(p,p\gamma)^{32}S$ nuclear reaction. The present method is therefore superior to $^{18}O(p,p\gamma)^{18}O$ nuclear reaction in the analysis of sulphides. These applications underline the suitability of the method in the determination of bulk oxygen in materials.

5.3.4 Uncertainty in measurements

Uncertainty is one of the most important characteristics of a result obtained from a measurement. It defines the reliability and hence the quality of results. The evaluation of uncertainty therefore constitutes an essential part of quantitative analysis. Combined uncertainty is a useful approach of representing the uncertainty of a multi-parameter analysis. Presently, the combined uncertainty of oxygen determination is 6%. It was calculated by propagating standard uncertainty of the parameters (3% each for yields and stopping cross sections of the standard as well as the sample) in **equation (5.2)** by invoking the concept outlined in reference **[169]** for a quotient formula. Importantly, the combined uncertainty increases to about 8% on taking the cognizance of homogeneity of the standard that is represented by an uncertainty of about 5% in yield measurements at different locations of the target.

5.4 Oxygen determination in materials by $^{18}O(p,p'\gamma)^{18}O$ nuclear reaction

5.4.1 Spectral features

Fig. 5.6 shows a typical prompt γ-ray spectrum recorded with the HPGe detector on irradiating the $CaCO_3$ disc with 3.0 MeV proton beam. The 1982 keV γ-rays emitted from the $^{18}O(p,p'\gamma)^{18}O$ nuclear reaction are prominently present in the spectrum. The spectrum also contains 495 and 871 keV γ-rays, attributable to the $^{16}O(p,\gamma)^{17}F$ (Q= 0.596 MeV) and $^{17}O(p,p'\gamma)^{17}O$ nuclear reactions respectively. These reactions occur simultaneously with the $^{18}O(p,p'\gamma)^{18}O$ reaction during irradiation. It is important to note that the relative natural abundance of the ^{16}O, ^{17}O and ^{18}O isotopes is 99.758, 0.037 and 0.204% respectively. A perusal of energy level schemes reported in references **[170,171]** shows that the 495 keV γ-ray results from the transition from the first excited state with $J = 1/2^+$ to the ground state with $J= 5/2^+$ of the ^{17}F nucleus; the 871 keV γ-ray, from the first excited state with $J = 1/2^+$ to the ground state with J= $5/2^+$ of the ^{17}O nucleus while the 1982 keV γ-ray emanates following the transition from the first excited state with J = 2^+ to the ground state with J= 0^+ of the ^{18}O nucleus.

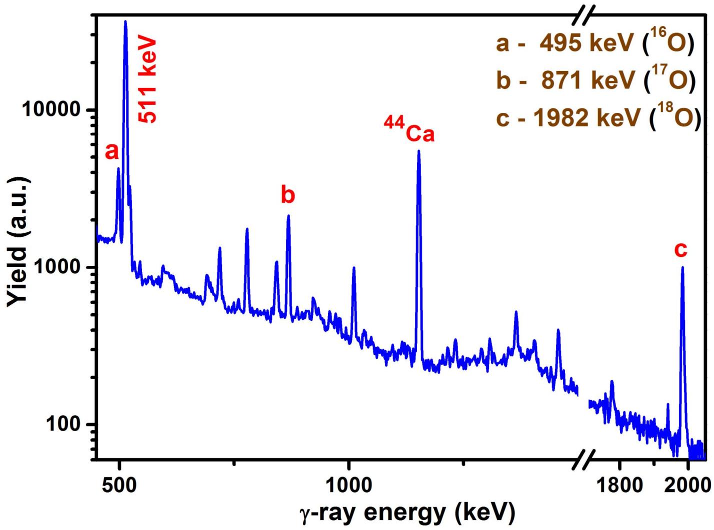

***Fig. 5.6**: Prompt γ-ray spectrum of a target consisting of 75 wt% $CaCO_3$ and 25 wt% high purity graphite recorded at 0° with HPGe using a 3 MeV proton beam.*

5.4.2 Analytical capabilities

5.4.2.1 Thick target γ-ray yields

In order to ascertain the analytical proficiency of these reactions, the thick-target yields of the 495, 871 and 1982 keV γ-rays were measured at 0° as well as 90° angles (with respect to the direction of the beam) in the 3.0 to 4.2 MeV proton energy range at 200 keV energy intervals. The counts under a γ-ray peak obtained after the subtraction of a linear background were normalized to the total charge and the solid angle of the measurement which served as the yield of the corresponding γ-ray. The yields of the γ-rays measured as a function of beam energy at 0° and 90° angles are shown in **Fig.5.7** for illustration. The important inferences drawn from the yield measurements are: (a) the yield of the γ-rays, more pronouncedly that of the 1982 keV γ-rays, increases with proton beam energy, (b) amongst the three, the 1982 keV γ-ray has the highest yield above E_p= 3.6 MeV and (c) the 495 as well as 871 keV γ-rays have, irrespective of incident beam energy, nearly identical yields at 0° and 90° while the 1982 γ-rays have a comparatively higher yields at the 0° detection angle. The near constancy of the yields of the 495 or 871 keV γ-rays at 0° and 90° angles is consistent with the angular isotropic distribution of γ-rays emitted as a result of the transition from a J= $1/2^+$ state.

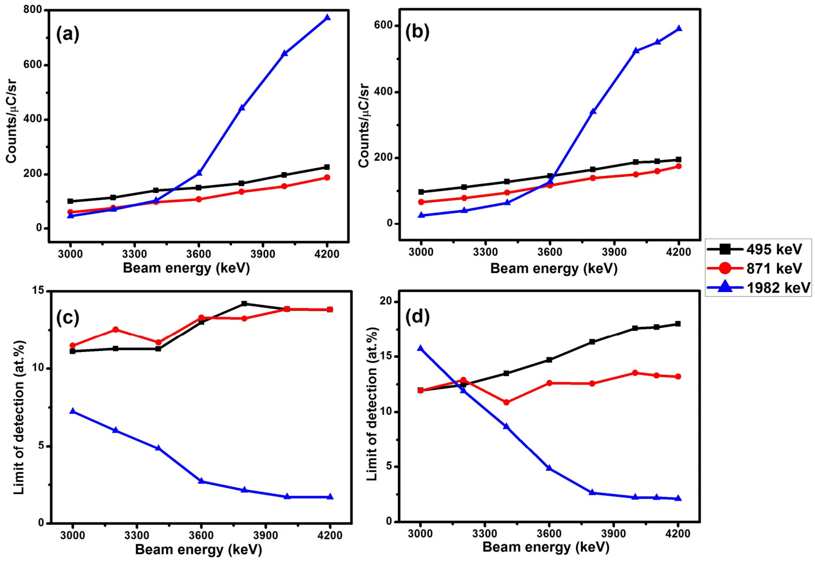

Fig.5.7: *Thick target yields of the 495, 871 and 1982 keV γ-rays emitted from the* ^{16}*O(p,γ)*^{17}*F,* ^{17}*O(p,p′γ)*^{17}*O and* ^{18}*O(p,p′γ)*^{18}*O nuclear reactions at (a) 0° and (b) 90° angles of detection. The curves in (c) and (d) represent the limits of detection of the reactions at 0° and 90° angles of detection respectively.*

5.4.2.2 Limits of detection

Fig.5.7 also shows the limits of detection (LOD) of the nuclear reactions in the calcium carbonate (25 wt%) and graphite (75 wt%) mixture at different bombarding energies and detection angles. The LODs are calculated on the basis of three times the standard deviation of the background under the relevant γ-ray peaks. These follow the trend witnessed for thick target yields and accordingly, the best LOD of ~1.7 at% is obtained for the ^{18}O(p,p′γ)^{18}O nuclear reaction for measurements at 0° angle with the 4.2 MeV proton beam. The LODs of ^{16}O(p,γ)^{17}F and ^{17}O(p,p′γ)^{17}O nuclear reactions, on the other hand, measure about 18 and 14 at% respectively under similar experimental conditions. Therefore $^{18}O(p,p'\gamma)^{18}O$ is the most suitable reaction for oxygen determination. The analysis of different materials showed that the LOD of the reaction varies considerably with the nature of the matrix. In materials composed of high Z elements that are not prolific prompt γ-ray emitters (e.g. lanthanides, tungsten, uranium etc.), the $^{18}O(p,p'\gamma)^{18}O$ nuclear reaction has a LOD of about 2 at%. Conversely, in materials consisting of low Z elements which are sensitive to PIGE (e.g. B, Li, Na, Al etc.) the LOD of the reaction is 15–20 at% due to a higher background around 1982 keV in the γ-ray spectra. Notably, for such elements as Al, P and S, the peak of 1982 keV γ-rays is situated on the Compton edge of the 2211, 2230 or 2230 keV γ-rays emitted from the $^{27}Al(p,p'\gamma)^{27}Al$, $^{31}P(p,\gamma)^{32}S$ and $^{32}S(p,p'\gamma)^{32}S$ nuclear reactions respectively. This is well illustrated by the γ-ray spectrum of SnS powder containing oxygen as an impurity in **Fig.5.8.**

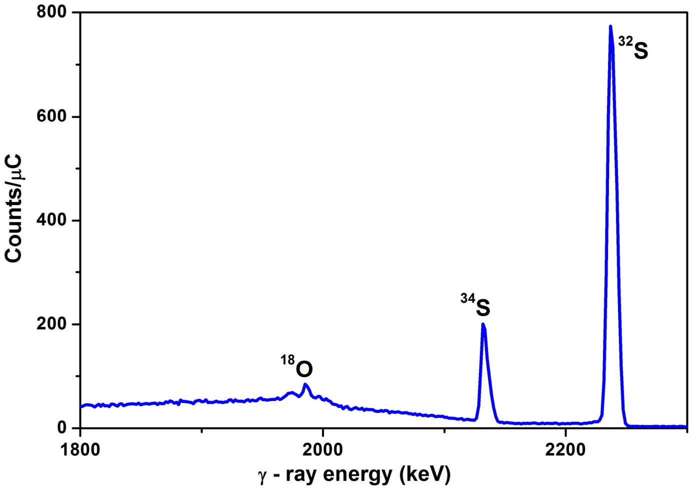

Fig.5.8: *Prompt γ-ray spectrum of SnS acquired with 4.0 MeV protons.*

5.4.2.3 *Probing depths and interferences*

Apart from nuclear or spectral interferences, the prevalence of moisture in the compounds can also be a cause of concern, as it may result in an overestimation of their oxygen contents. Presently, though an independent measurement on the content of moisture in the samples was not performed, it, if existing, is presumably removed during the creation of the vacuum. This is manifested in the stability of the targets under proton beam irradiation which is indicated by the constancy of the charge normalized yields of the 1982 keV γ-rays for repeated measurements. So far as the probing depth is concerned, for the $^{18}O(p,p'\gamma)^{18}O$ reaction it is ~60 µm in SiO_2, ~40 µm in TiO_2 and ~30 µm in UO_2 at E_p= 4.2 MeV considering that the reaction commences at E_p = 3.0 MeV. In view of the rather large probing depth, the method can be conveniently employed for the determination of bulk oxygen in materials.

5.4.3 Quantification

The content of oxygen or the atomic composition of a material was determined by the relative method. A binary oxide can be represented by a general formula A_xO_y where A is an element and x + y = 1. The atomic ratio i.e. x/y in the binary oxides was determined using the following formula that was derived from the standard thick-target yield equation **[85]**:

$$\frac{x}{y} = \frac{C_{A(std)} \times R_A \times \varepsilon_{O(std)}}{C_{O(std)} \times R_O \times \varepsilon_{A(std)}} \qquad (5.3)$$

$$\text{where } R_i = \frac{Y_{i(samp)}}{Y_{i(std)}} \qquad (5.4)$$

In **equation (5.3)** $C_{A(std)}$ and $C_{O(std)}$ represent the concentration of element A and oxygen in their respective standards, Y_i is the charge-normalised yield of the characteristic γ-rays of the element *i* (A or oxygen) in the sample (samp) or standard (std); $\varepsilon_{A(std)}$ and $\varepsilon_{O(std)}$ are the stopping cross-sections of the proton in the standards of element A and oxygen respectively. It is worthwhile mentioning that **equation (5.3)** it is valid for cases wherein the standard of the element A and that of oxygen are two different chemical entities but it can be suitably modified if the same compound serves as the standard for both elements.

It is implicit that the **equation (5.3)** is applicable for compounds whose constituent A is also sensitive to PIGE **(Table 1.7).** However, if this is not the case or there is a lack of a suitable standard of A, it is more appropriate to represent the compound by the formula $A_{1-x}O_x$ and the concentration of oxygen in terms of atomic fraction (i.e. x) can be calculated using the formula

$$x = \frac{\left(12M\varepsilon_A + NW_A\varepsilon_C\right)}{12M\left(\frac{\varepsilon_{O(std)}}{R_O C_{O(std)}} + \left(\varepsilon_A - \varepsilon_O\right)\right) + N\varepsilon_C\left(W_A - W_O\right)} \qquad (5.5)$$

where ε_A and ε_O are the stopping cross-sections of element A and oxygen respectively while M and N represent the weight fractions of compound ($A_{1-x}O_x$) and the graphite in the target respectively. Also, W_A and W_O are the atomic weights of element A and oxygen respectively.

The ternary (e.g. $LiCoO_2$) or quaternary ($LiFePO_4$) oxides can be represented by chemical formula $A_xB_yO_z$ or $A_xB_yC_zO_p$ where the sum of the atomic fractions of all the elements in a compound is unity. The atomic composition of these compounds can be calculated using formula similar to **equation (5.3)** which is not mentioned here for the sake of brevity. Importantly, it is presumed that all the constituent elements of the compounds are sensitive to PIGE. The reactions involving these and several other elements relevant to the present study and their characteristic prompt γ-rays are listed in **Table 1.7** for referencing **[81]**. The stopping cross-sections of the elements and compounds obtained from SRIM -2013 were used in calculations **[102]**.

5.4.4 Validation and analytical results

5.4.4.1 Binary oxides

The analytical efficacy of the $^{18}O(p,p'\gamma)^{18}O$ nuclear reaction was ascertained by analysing several binary oxides with well-defined stoichiometry. **Table 5.3** lists the measured contents of oxygen in some of these oxides along with their theoretical oxygen stoichiometry. The prompt γ-ray spectra of representative oxides of low, mid and high Z elements namely SiO_2, TiO_2 and Gd_2O_3 respectively used for the determination are shown in **Fig.5.9** for illustration. The spectrum of SiO_2 consists of a strong γ-ray peak at 1779 keV and that of TiO_2, at 981 keV attributable to the $^{28}Si(p,p'\gamma)^{28}Si$ and $^{48}Ti(p,p'\gamma)^{48}Ti$ nuclear reactions respectively. However, gadolinium emits low energy γ-rays and therefore these are not shown in the spectrum. The quantitative analyses of SiO_2 and TiO_2 specimens were carried out using **equation (5.3)** and, for the sake of comparison, also using **equation (5.5)** while the content of oxygen in Gd_2O_3 was determined using only **equation (5.5)** due to the unavailability of a proper standard of gadolinium. It can be observed from **Table 5.3** that the measured contents of oxygen in the first three and also in the other materials are in good (3-7%) agreement with the respective theoretical concentrations. Insofar as the **equations (5.3)** and **(5.5)** are concerned, the former is expected to yield more accurate results since it utilises standards for both the elements. However, as evidenced by the data in **Table 5.3**, both the equations provide nearly identical results. This inference underscores the adequacy of the **equation (5.5)** for the determination of oxygen in matrices composed of heavy metals, many of which do not produce prompt γ-rays (e.g. Sn, La) in the proton energy range used in the present study. In fact, the absence of strong prompt γ-ray producing reactions facilitates measurements with better precision (~1%) in heavier matrices as compared to the precision of ~3% observed for the lighter matrices.

The method was utilised to determine oxygen in a sintered disc of uranium oxide (UO_x) and tungsten powders. **Fig.5.10** shows the prompt γ-ray spectra of the two kinds of samples acquired with 4.2 MeV protons wherein the peaks due to the 1982 keV γ-rays are conspicuously present. Uranium does not emit any prompt γ-ray and the 1001 keV γ-ray in the spectrum of uranium oxide has its origin in ^{234m}Pa, a progeny of ^{238}U. Tungsten, on the other hand, emits 101, 111 and 122 keV γ-rays by way of the $^{182}W(p,p'\gamma)^{182}W$, $^{184}W(p,p'\gamma)^{184}W$ and $^{186}W(p,p'\gamma)^{186}W$ nuclear reactions respectively. The 1014 or 1779 keV γ-rays in the spectra are due to minor (~ 1 wt %) impurities of Al and or Si prevailing in the samples. The concentration of oxygen in the two specimens calculated using **equation (5.5)** is presented in **Table 5.3**. It is important to mention that the precision of the oxygen content in the UO_x specimen, estimated on the basis of five measurements with each lasting for about 45 minutes at a beam current of about 50 nA, is about 1%. The method, therefore, is well suited for the determination of oxygen and, indirectly O/U ratio, in uranium oxide samples with non-destructive analysis, rapidity and insensitivity to uranium oxidation states being the major advantages. So far as the other specimen is concerned, it serves as yet another example to demonstrate the applicability of the method to high Z matrices. Moreover, W powders are extensively used in fusion research and the method can be applied to study oxygen pick up and or its retention during processing.

Table 5.3: *Concentration of oxygen in different binary oxides determined using* $^{18}O(p,p'\gamma)^{18}O$ *nuclear reaction (triplicate or higher number of measurements)*

Oxide	Reference (at%)	Determined (at%)	
		Equation (5.3)	Equation (5.5)
Silicon dioxide	66.7	67.3 ± 1.0	65.0 ± 1.5
Titanium oxide	66.7	67.3 ± 1.0	66.5 ± 1.3
Zinc oxide	50.0	-	48.5 ± 1.2
Zirconium oxide [a]	-	68.5 ± 1.2	66.5 ± 1.0
Zirconium oxide [b]	-	66.2 ± 1.0	63.3 ± 1.5
Gadolinium oxide	60.0	-	64.0 ± 1.0
Tungsten powder	-	-	15.7*
Uranium oxide	-	-	62.6 ± 1.0

*- single measurement; a and b are two different samples of zirconium oxide

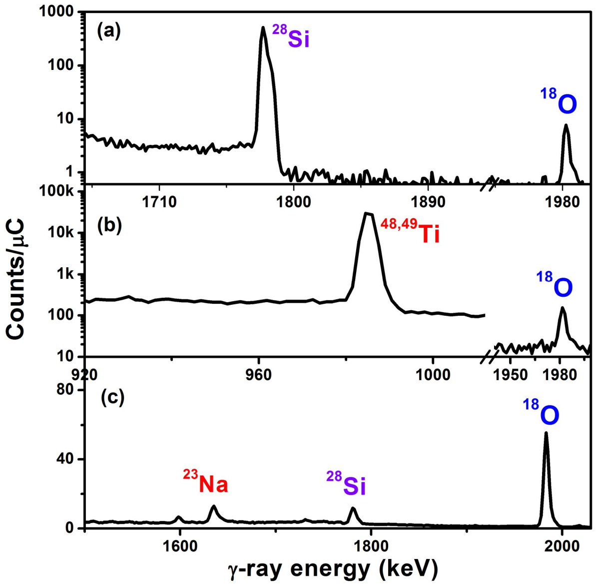

Fig. 5.9: *Prompt γ-ray spectra of (a) SiO_2, (b) TiO_2 and (c) Gd_2O_3 measured with 4.0 MeV protons respectively.*

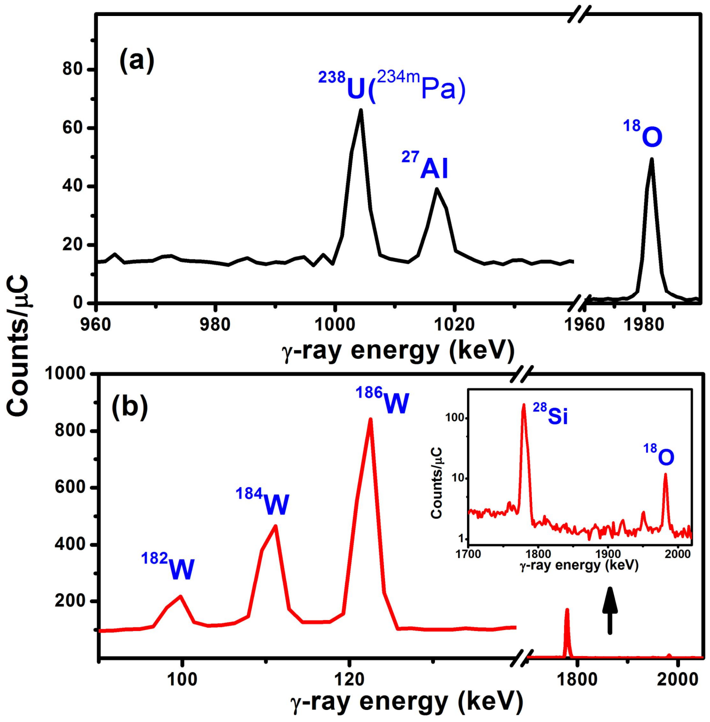

Fig.5.10: *Prompt γ-ray spectra of (a) uranium oxide and (b) tungsten oxide acquired with 4.2 MeV protons. The inset in fig (b) shows the peaks of Si and oxygen.*

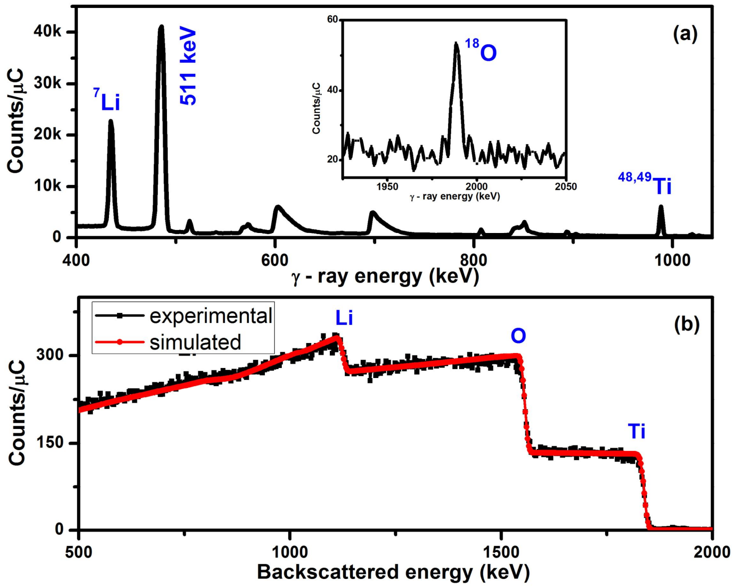

Fig.5.11*: Analysis of Li$_2$Ti$_2$O$_4$: (a) a PIGE spectrum and (b) a proton backscattered spectrum recorded with 4.0 and 2.0 MeV protons respectively. The inset in Fig.(a) shows the peak of oxygen.*

5.4.4.2 Ternary oxides

The method is equally applicable to ternary oxides, namely lithium titanate and lithium cobaltate as well and provides their analysis with reasonably good accuracy and precision. A typical PIGE spectrum of lithium titanate is shown in **Fig.5.11(a)** while the measured atomic compositions of the titanate and cobalate ceramics are presented in **Table 5.4.** PIGE exhibits high sensitivity (~10 ppm) to lithium. As a result, the spectrum consists of a very strong peak of the 478 keV γ-rays emitted from the ^{7}Li(p,p′γ)^{7}Li reaction. The higher sensitivity also requires the acquisition of data at a proton beam current of 2-3 nA to keep the dead time within acceptable (<5%) levels. Furthermore, the peak due to the 1982 keV γ-rays of oxygen is situated on an elevated background caused by the ^{7}Li(p, γ)^{8}Be nuclear reaction that emits 17.6 MeV γ-rays **[172]**. As a result, the data are collected for a comparatively longer period of time (~90 minutes) in order to ensure measurements with good statistics.

Lithium titanate and lithium cobaltate are important energy materials but are analytically intractable. It was, therefore, considered worthwhile to the analysis of the titanate ceramics by p-EBS in order to cross-validate the PIGE results. It is important to mention that p-EBS, by virtue of higher cross-sections of the $^{16}O(p,p)^{16}O$ scattering, has previously been utilised for analysing oxygen bearing materials including high temperature superconductors, for instance yttrium barium copper oxide ($YBa_2Cu_3O_x$) **[173,174]**. The spectrum (of $Li_2Ti_2O_4$) shown in **Fig. 5.11(b)** represents a typical proton-backscattered spectrum of titanate ceramics wherein the signal of O and also that of Ti / Li are distinctly observed. Notably, as is evident by the superimposed curve, it was simulated satisfactorily for quantification. The data presented in **Table 5.4** show that the backscattering spectrometry technique provides good results too but these are not entirely consistent with the theoretical compositions or those measured by PIGE. Rutherford backscattering spectrometry (RBS) is an absolute method but the accuracy of the method, as described recently by Colaux et al. depends on a number of parameters **[175]**. p-EBS is analogous to RBS except that the scattering cross section is non-Rutherford in nature. As a result, the accuracy of p-EBS depends, in addition to the factors applicable to RBS, on the accuracy of the experimentally or theoretically determined scattering cross-sections as well. Therefore the accuracy of the differential cross-sections of $^{6}Li(p,p)^{6}Li$, $^{7}Li(p,p)^{7}Li$, and O(p,p)O scattering and the assumption that scattering cross-sections for Ti and Co are entirely Rutherford may be among the factors behind the discrepancy in the compositions determined by p-EBS. The present method, however, does not suffer from such limitation and, therefore, can be considered to be superior to p-EBS. It is, in fact, superior even to the PIGE method described in reference **[176]** (which is performed with 8 MeV protons and is susceptible to interference from fluorine) and thus is the preferred choice for the complete compositional analysis of titanate and cobaltate ceramics. Furthermore, it is instructive to mention that due to the sensitivity of PIGE to Cr and Mn, the methodology can be extended to the analysis of $LiCrO_4$ and $LiMn_2O_4$ which are also important energy materials.

***Table 5.4**: Atomic composition of ternary oxides determined by PIGE and p-BS*

Oxide	Chemical formula	Determined [Li: Ti(Co): O]	
		PIGE	p-BS
Lithium titanate	$Li_2Ti_2O_4$	1: 1: 2.2	1: 1.1: 2.6
Lithium titanate	Li_2TiO_3	2: 1: 3.2	2: 0.8: 3.3
Lithium cobaltate	$LiCoO_2$	1: 0.9: 2.1	-

The present methodology was also extended to determine the content of oxygen in barium titanate and barium poly titanate ceramics. The determination of atomic composition of these ceramics by X-ray spectrometry is difficult due to extensive overlap between Ti K_α (4.51 keV) and Ba L_α (4.47keV) X-rays. However, Ti emits 981 keV γ-rays due to $^{48}Ti(p,p'\gamma)^{48}Ti$ reaction (**Table 1.7**) occurring simultaneously with $^{18}O(p, p'\gamma)^{18}O$ reaction. The concentrations of oxygen in these ceramics determined by the method are given in **Table 5.5**. Notably, a significant decrease in the content of oxygen is observed in the barium titanate ceramic on its treatment in hydrogen atmosphere at about 600°C. The reduction brought about by annealing in hydrogen atmosphere has important effect on the electrical properties of the ceramic. This method can be utilized for investigating a correlation between the oxygen content and the electronic properties of the material.

***Table 5.5:** Concentration of oxygen in different binary oxides determined using $^{18}O(p, p'\gamma)^{18}O$ nuclear reaction*

Oxide	Reference (at.%)	Determined (at.%)
n-Barium titanate	60	60.5
Reduced barium titanate	-	58.9
Barium tetratitanate	64.3	64.5
Barium nonatitanate	64.5	64.0

5.4.4.3 Multinary oxides

In order to further probe the potential of the method, it was applied to multinary compounds such as $LiFePO_4$ and $LiFePO_4/C$ which, understandably, are analytically more complex and challenging than the titanates. $LiFePO_4$ and its composite with carbon (i.e.

$LiFePO_4$/C) are promising cathode materials for Li-ion batteries. **Fig.5.12** shows the PIGE spectrum of $LiFePO_4$ acquired with 4.0 MeV protons wherein the peaks of the constituent elements are vividly present. However, two features of the spectrum need special mention. Firstly, the signal of oxygen is relatively weak since it is riding over the Compton edge of 2230 keV γ-rays emitted from the $^{31}P(p,\gamma)^{32}S$ reaction. Secondly, the γ-peak at 843 keV, attributable to Fe, is unusually broad and consists of a shoulder around about 837 keV. The origin of the 837 keV γ-rays lies in the $^{73}Ge(n,\gamma)^{74}Ge$ and $^{72}Ge(n,n'\gamma)^{72}Ge$ reactions taking place in the Ge crystal of the HPGe detector **[137]** while the neutrons involved in inducing these reactions are produced from the $^{7}Li(p,n)^{7}Be$ reaction (Q= -1.664 MeV) occurring in the $LiFePO_4$ target. Therefore, the true contribution of Fe was determined by fitting the envelope around 843 keV into two components. Meanwhile, the content of carbon in the $LiFePO_4$/C composite specimen was determined by means of the $^{13}C(p,p'\gamma)^{13}C$ reaction that emits 3089 keV γ-rays **[177]**. The compositions of the compounds thus measured are listed in **Table 5.6**. The combined uncertainty of the analysis which has contributions from the peak area measurement, the stopping cross section and the charge integration of the sample as well as the standard is estimated to be about 5% for the binary and about 8% for the quaternary or multinary compounds. In fact, standardless PIGE measurements can provide results with much better uncertainty, however, it requires a precise knowledge of reaction cross-sections over a wide range of proton energy, the efficiency of the detector for γ-rays of different energies and other parameters appearing in the equation relating the yield of the γ-rays with the concentration of the elements **[178]**.

For the sake of cross-validation, the multinary compounds were also analysed by proton backscattering spectrometry with a typical backscattered spectrum of $LiFePO_4$ shown in **Fig. 5.12(b)**. Though the signal (step) of Fe, P or O is prominent, that of Li is not as prominent as in the spectrum of $Li_2Ti_2O_4$ in **Fig. 5.11(b)** due to its comparatively lower content in the compound and relatively higher background.

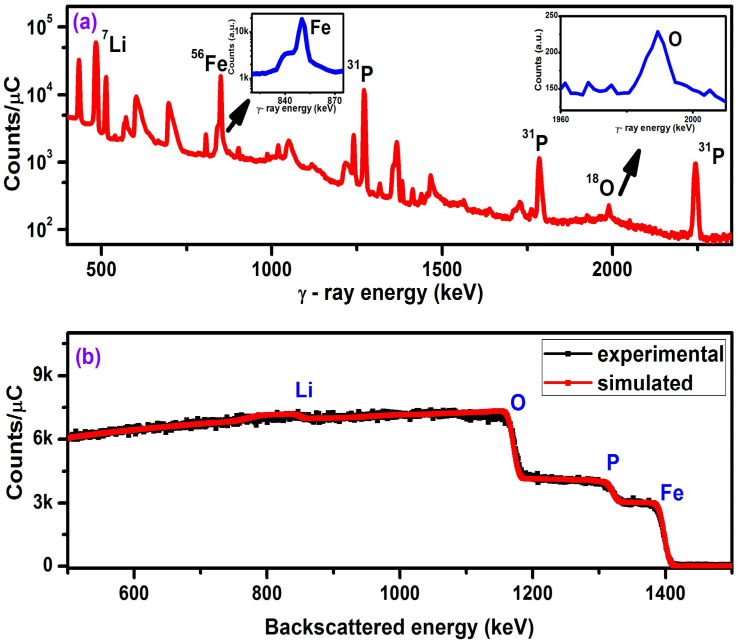

Fig.5.12: Analysis of $LiFePO_4$ (a) a PIGE spectrum and (b) a proton backscattered spectrum recorded with 4.0 and 1.5 MeV protons respectively. The insets in Fig (a) show the peaks of Fe and oxygen.

An examination of the data presented in **Table 5.6** shows that for $LiFePO_4$ the PIGE and p-EBS results are in good agreement but for $LiFePO_4$/C, a disagreement in values for Fe and, particularly for P prevails which, apart from the uncertainty associated with the differential scattering cross-sections of the different isotopes, may also arise due to the inhomogeneous distribution of the elements. It is to be noted that as compared to the probing depth of tens of microns of PIGE with 4.0 MeV protons, EBS performed with 1.5 MeV protons has a probing depth of only about 8 micron in $LiFePO_4$. These considerations suggest that PIGE provides a more effective approach for the compositional analysis of this important class of materials.

Table 5.6: *Atomic composition of different quaternary oxides determined by PIGE and p-BS*

Chemical formula	Determined[Li: Fe: P: O (C)]	
	PIGE	p-BS
$LiFePO_4$	1: 1: 0.9: 3.6	1: 0.9: 0.8: 3.4
$LiFePO_4$/ C	1: 1.2: 0.8: 4.4 (1.9)	1: 1.1: 1.1: 4.6 (2.2)

5.5 Conclusions

The measurement of prompt 5.27 MeV γ-rays emanating from $^{18}O(p,\alpha\gamma)^{15}N$ nuclear reaction induced by 3.0-4.2 MeV proton beam provides a new and useful approach for the detection and determination of bulk oxygen in materials. With a detection limit of about 1.3 at.% and a probing depth spanning over several tens of microns at 4.2 MeV proton energy, the present method is eminently suitable for analyzing materials with high Z constituents. The suitability is demonstrated by analyzing dysprosium oxide, uranium oxide and other oxides with reasonably good accuracy and precision. The method does not suffer interference from any element except fluorine and to a certain extent, nitrogen. However, due to higher sensitivity of proton induced γ-ray emission for low Z elements such as Li, B, Na, Al etc., the presence of these elements in high abundance can limit the applicability of the method.

The $^{18}O(p,p'\gamma)^{18}O$ nuclear reaction emitting 1982 keV γ-rays is employed in PIGE measurements for the determination of bulk oxygen in materials. The method is simple, rapid and non-destructive. It is endowed with a detection limit of ~2 at% in heavy matrices and ≥ 15 at% in light matrices, and has a probing depth of more than 30 μm at the 4.2 MeV proton energy. High precision measurement of oxygen in mid and high Z matrices is one of the discerning features of the method. It can, therefore, be applied to determine subtle changes in the oxygen stoichiometry in such materials. The method is largely free from nuclear or spectral interferences. However, due to the higher sensitivity of PIGE to low Z elements such as Li, B, Na, Al etc., the presence of these elements in high abundance can impair its detection limit and rapidity. Nevertheless, the simultaneous multielement detection capability of the technique can be exploited to determine the complete elemental composition of such compounds. It is amply demonstrated by analyzing complex oxides such as Li_2TiO_3 and $LiFePO_4$. Finally, though not probed explicitly, the simultaneous occurrence of the $^{16}O(p,\gamma)^{17}F$, $^{17}O(p,p'\gamma)^{17}O$ and $^{18}O(p,p'\gamma)^{18}O$ nuclear reactions emitting 495, 871 and 1982 keV γ-rays raises the possibility of isotopic analyses of oxygen in favourable materials.

Chapter 6

Detection and Depth Profiling of Silicon by PIGE: Application to SiC and Si_3N_4 Films

6.1 Introduction

The potential of ion beam techniques for depth profiling low Z elements such as H, B, N, F non-destructively has been discussed in the previous chapters. The methodologies for many of these elements are, in fact, well-established and are used routinely in IBA laboratories. In **Chapter 3**, two methods one based on PIGE and other on NRA are presented for depth proofing Li in LIBs. However Si, probably the most important electronic material of the modern times, is a notable exception. The literature survey shows that though the depth profiling of Si has been a subject of several studies, a robust method with good analytical features is still elusive. For instance, the elastic backscattering spectrometry (EBS) methods based on ^{28}Si(p,p)^{28}Si or ^{28}Si(α,α)^{28}Si scattering are particularly not attractive due to the absence of an isolated and strong resonance in the excitation functions **[179,180]**. Recently, Ntemou et al. have measured the differential cross-sections of ^{nat}Si(d,d)^{nat}Si scattering but did not demonstrate its efficacy for depth profiling applications **[181]**. So far as NRA is concerned, Gurbich and Molosdov have utilised ^{28}Si(d,p)^{29}Si reaction to depth profile Si in steel **[182]**. However, Kokkoris et al, in their study on the differential cross-sections, did not find the ^{28}Si(d,p)^{29} Si reaction adequately suitable for NRA purposes **[183]**. Recently, Demarche et al have used ^{28}Si(α,p$_0$)^{31}P nuclear resonance reaction for the analysis of shallow ^{28}Si implantations in SiO$_2$/Si **[180]**. But they did not discuss the applicability of the method for large depth analysis. It is important to note that the method utilises a 25 micron mylar stopper foil to prevent the detection of the backscattered α-particles.

In addition to NRA and backscattering spectrometry, particle induced γ-ray emission (PIGE) can also be utilised for depth profile measurements by making use of resonances in the reactions involved. Boni et al and, more recently, Jokar et al measured the differential cross sections of the ^{28}Si(p,p′γ)^{28}Si reaction that emits 1778 keV γ-rays and reported the existence of a resonance at 3.1 MeV proton energy **[184,185]**. Both studies were conducted on thin targets; the former utilised films of SiO_2 while the latter, those of SiO but the depth profiling capabilities of the resonance were not explored. In yet another study Chiari et al have measured the thick target yields of 1778 keV γ-rays emitted from this reaction in 2.5 to 4.1 MeV proton energy region **[186]**. The measurements were, however, essentially for the bulk determination of Si by PIGE. As a result, not only depth profiling, even the existence of a resonance in the excitation function of the reaction was not discussed. In summary, not much information on the depth profiling capabilities of the $^{28}Si(p,p'\gamma)^{28}Si$ resonance reaction exists in literature.

Through the present work we present our investigations on the efficacy of the resonance at 3.1 MeV in the $^{28}Si(p,p'\gamma)^{28}Si$ reaction for depth profiling of silicon in materials. The investigations entail the measurement of the yield curves of 1778 keV γ-rays for thin as well thick targets in 3.0 to 3.8 MeV proton energy region and an assessment of such analytical features as depth resolution, probing depth and detection sensitivity of the resonance. In addition, the methodological considerations for quantification, keeping particularly the rather larger width of the resonance in mind, are also described. The efficacy of the methodology is evaluated by analysing thin films and also thick targets.

6.2 Experimental details

6.2.1 Materials for analysis

The source and the preparation of materials have been described in **Chapter2, Section 2.2.**

6.2.2 Proton beam irradiation

The irradiation of the samples (targets) and the measurement of the emitted radiations are described in detail in **Chapter 2, Section 2.6**. Briefly, the samples were bombarded with energetic and a well-collimated proton beam (Φ~2mm) in 3.0 – 3.8 MeV region at normal incidence in a scattering chamber maintained at 1×10^{-5} torr vacuum. For depth profile experiments the incident beam energy was successively increased in steps of 4 keV in the vicinity of resonance energy (i.e. 3098 keV) and in steps of 10-20 keV above it. The beam current during irradiation was ≤30 nA.

6.2.3 Acquisition of γ-ray spectrum

The prompt γ-rays emitted from ^{28}Si(p,p′γ)^{28}Si reaction were detected by HPGe detector. The details of the features of the detector and the experimental geometries and the electronics of the data acquisition system are described in detail in **Chapter 2, Section 2.6**.The γ-ray spectra were recorded at each proton energy for a charge of 5-10 μC to obtain peaks with statistically significant counts.

6.3 γ-ray spectra / spectral features

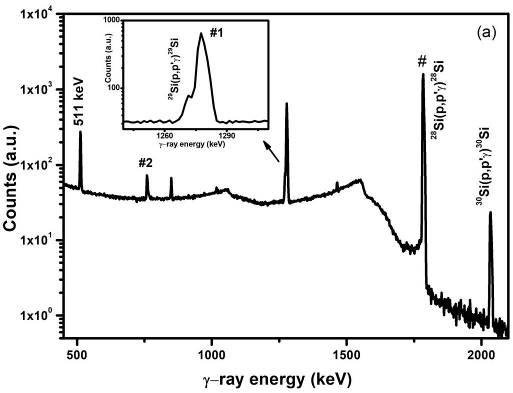

__Fig.6.1(a):__ Prompt γ-ray spectrum of Si acquired by HPGe detector on irradiating with 3.0 MeV protons

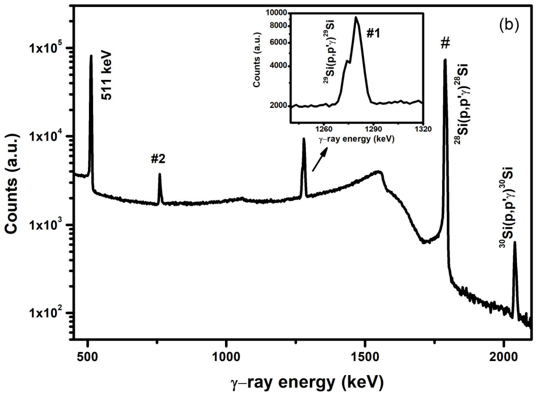

__Fig.6.1(b):__ Prompt γ-ray spectrum of Si acquired by HPGe detector on irradiating with 3.8 MeV protons

Fig.6.1 shows the high resolution γ-ray spectra acquired on irradiating the Si wafer with 3.0 and 3.8 MeV protons. The spectra consist of sharp peaks of 1778 keV prompt γ-rays emitted from ^{28}Si(p,p′γ)^{28}Si reaction. The different intensities of the γ-rays in the two spectra are reflective of the relative cross-sections of the reaction at the respective energies. The two other natural isotopes of Si, ^{29}Si and ^{30}Si, also undergo (p,p’γ) inelastic scattering reaction simultaneously, emitting 1273 and 2033 keV γ-rays respectively in the process. The intensities of the two γ-rays, however, are considerably less than the intensity of 1778 keV γ-rays. A close examination of the peak at 1273 keV suggests the presence a shoulder at about 1267 keV. It is attributed to the first escape peak of 1778 keV γ-rays while the corresponding second escape peak of considerably less intensity appears at 766 keV. Incidentally, the broad hump around 1560 keV arises due to the Compton scattering of the 1778 keV γ-rays. An important observation, though not directly related to the objective of the investigations, emerging from the spectral analysis is that due to the simultaneous occurrence of $^{28}\text{Si}(p,p'\gamma)^{28}\text{Si}$, $^{29}\text{Si}(p,p'\gamma)^{29}\text{Si}$ and $^{30}\text{Si}(p,p'\gamma)^{30}\text{Si}$ reactions that produce distinct and largely interference free γ-rays, PIGE can be utilised for the determination of the three isotopes of Si in favourable conditions.

6.4 Yield curve and identification of resonances

Fig. 6.2 shows the charge normalised thick target yield curve of 1778 keV γ-rays in 3.0 to 3.8 proton energy region. The area under the 1778 keV γ-ray peak obtained after the subtraction of linear background represents the intensity or yield of the peak. The curve consists of a prominent step at E_p= 3098 keV followed by a weak one around E_p = 3337 keV. At E_p> 3450 keV, the γ-ray yield increases almost continuously with proton beam energy and the curve is devoid of any discernible step. **Fig.6.3** shows the yield curve of 1778 keV γ-rays for a thin film i.e. Si_xN_y (110nm)/ GaAs. It is important to note that there is no spectral interference from either gallium or arsenic. Similarly no interference is observed from nitrogen, the other constituent of the film. The thick and thin target yield curves are in good agreement in essence, conveying the presence of a prominent resonance at ~ 3098 keV and a weak one at ~ 3337 keV proton energy. Importantly, the reaction has no resonance below E_p = 3098 keV. In fact, the yield of 1778 keV γ-rays decreases rapidly below 3098 keV and becomes statistically insignificant at $E_p \leq 2600$ keV.

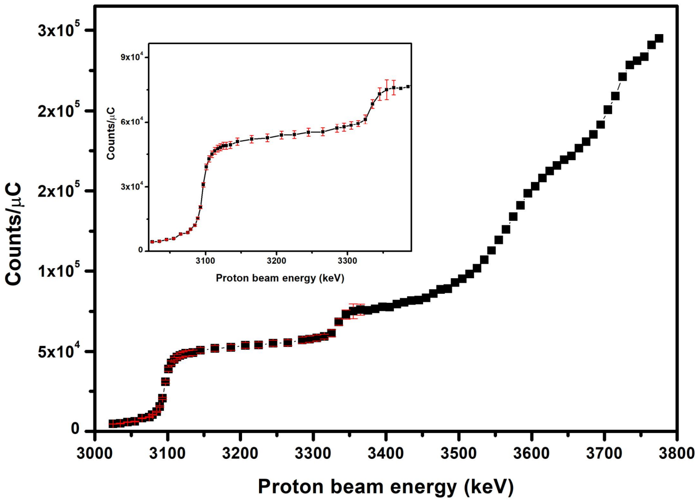

Fig. 6.2: *Thick target yield of 3098 keV γ-ray in 3.0- 3.8 MeV proton energy region. The target is elemental silicon*

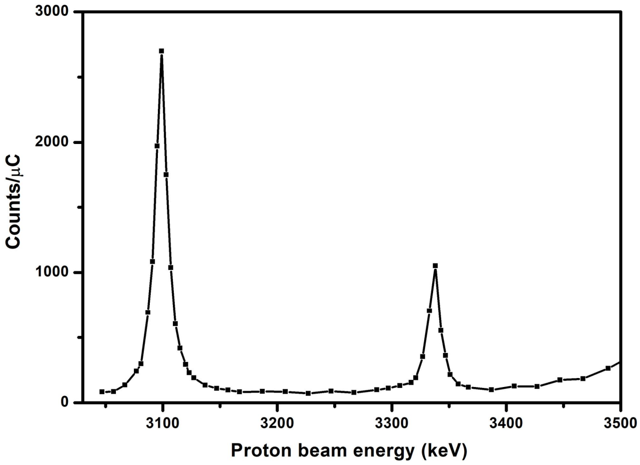

Fig. 6.3: *Thin target yield of 3098 keV γ-ray in 3.0 - 3.5 MeV proton energy region. The target is Si_3N_4 (110 nm)/GaAs.*

In order to determine the energy of the resonance and its width, the yield curves of the thick and thin targets were simulated using **equations (6.3)** and **(6.5)**. The theoretically generated yield curve superimposed on the experimentally determined thick target yield curve for the Si target is shown in **Fig 6.4.** The good agreement between the experimental and the simulated data is evident. The mid-point on the rise of the thick target step represents the resonance energy of the reaction and is determined to be 3098 keV by the first derivative of the simulated curve.

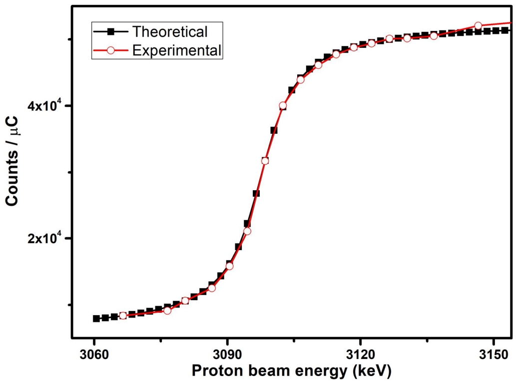

***Fig. 6.4:** Experimental and theoretical thick target yield curve for the Si target*

In a thin target, the energy corresponding to the maximum yield (E_{Ymax}) does not represent the resonance energy. The resonance, in fact, occurs at an energy lower to E_{Ymax} by an amount that depends on the thickness of the target and is given by $E_R = E_{Ymax} - 0.5\times\Delta E$. Presently, the E_R estimated from the yield curve of the thin target is **3098.0** keV. Apparently, the both kinds of targets yield fairly identical E_R; the difference of ~1 keV may arise from the energy spread of the beam, the uncertainty associated with the thickness of the Si_3N_4 film and the rather large width (discussed later) of the resonance. The comparatively higher value of the E_R determined using the thick target is nevertheless in agreement with a previous report on other reactions wherein it was shown that thick targets yield E_R with better precision and accuracy. Therefore, an energy of 3098±2 keV is assigned to the first resonance and, on similar grounds, 3337 ± 2 keV to the second resonance of the $^{28}Si(p,p'\gamma)^{28}Si$ reaction. The uncertainty is mainly due to energy spread of the beam arising from the instability of the terminal voltage. Notably, the resonance energies are in good agreement with the values reported in references. The simulation of the thick target yield curve showed the value of Γ for the resonance at 3098 keV to be 12 ± 0.5 keV. The value, in fact, represents the system resolution that has contributions from the width of the resonance, the energy spread of the beam and Doppler broadening, added in quadrature. The maximum combined contribution from the latter two factors is ~ 2 keV, therefore, the width of the resonance turns out to be

11.8 keV which agrees well with the previously reported values. Since the resonance at 3337 keV is rather weak and is not suitable for analytical measurements, no efforts were made to determine its width.

6.5 Interferences

The ^{28}Si(p,p′γ)^{28}Si reaction does not suffer from any spectral interference. However, interference can arise from ^{27}Al(p,γ)^{28}Si reaction. However this reaction is not prolific in the proton energy region of interest and the measurements with thick elemental Al foils showed that under identical experimental conditions the thick target yield of 1778 keV γ-rays emitted from this reaction is < 1% of that of the γ-rays from ^{28}Si(p,p′γ)^{28}Si reaction. Hence care must be exercised while depth profiling Si prevailing in low concentrations in Al-bearing matrices. Notably, the LOD for Si in Al matrix is about 5 at% due to the fact that the 1778 keV γ-rays are situated on the Compton background of 2230 keV γ-ray emitted from ^{27}Al(p,p′γ)^{27}Al reaction. All these reactions, understandably, occur simultaneously.

6.6 Methodology of depth profiling

The general equation describing the relationship between the concentration *C* of an element in a homogeneous sample of thickness Δx and the number of γ-rays N_γ emitted as a result of a nuclear reaction with cross-section σ at beam energy *E* is **[76,184]**

$$N_\gamma = c \cdot f \cdot A \cdot \varepsilon \cdot \Omega \cdot N_0 \int_{E-\Delta E}^{E} \frac{\sigma(E)}{S(E)} dE \qquad (6.1)$$

where f is the relative abundance of the isotope involved in the reaction, A is the Avogadro's number, ε is the detection efficiency of the detector for the emitted γ-rays, Ω is the solid angle of the detector, N_0 is the no. of incident particles, S is the stopping power of the ions of energy E in the sample and ΔE is the energy loss suffered by the ion beam while traversing the sample i.e. $\Delta E = \Delta x \times S$.

The cross section of the reaction as a function of energy in the vicinity of the resonance energy E_R is given by Breit-Wigner formula **[187,188]**

$$\sigma(E)=\frac{\sigma(E_R)\cdot\left(\Gamma/2\right)^2}{\left(E-E_R\right)^2+\left(\Gamma/2\right)^2} \qquad (6.2)$$

where $\sigma(E_R)$ is cross-section of the reaction at the resonance energy and Γ is the width of the resonance. It is important to mention that presently the influence of beam broadening factors such as the energy spread of the incident ion beam, straggling etc. on σ (E) have not been taken into consideration because these are assumed to be small compared to the width of the resonance.

The substitution of equation (2) in equation (1) gives rise the following yield equation for a thin target of thickness *Δx*

$$N_\gamma=\frac{c\cdot f\cdot A\cdot\varepsilon\cdot\Omega\cdot\sigma(E_R)\cdot N_0\cdot\Gamma}{2S(E)}\left[\arctan\frac{E-E_R}{\left(\frac{\Gamma}{2}\right)}\right]_{E-\Delta E}^{E} \qquad (6.3)$$

while for thick target, it is expressed by the formula

$$N_\gamma=\frac{c\cdot f\cdot A\cdot\varepsilon\cdot\Omega\cdot\sigma(E_R)\cdot N_0\cdot\Gamma}{2S(E)}\left[\arctan\frac{E-E_R}{\left(\frac{\Gamma}{2}\right)}+\pi/2\right] \qquad (6.4)$$

At higher beam energies the equation (6.4) can be written as

$$N_\gamma=\frac{\pi\cdot c\cdot f\cdot A\cdot\varepsilon\cdot\Omega\cdot\sigma(E_R)\cdot N_0\cdot\Gamma}{2S\left(E_R\right)} \qquad (6.5)$$

where c is the concentration of the element.

The shape of the γ-ray yield curve for a target depends on its thickness (i.e, on energy loss). These obtained for a Si targets using equation 6.4 assuming the resonance energy and resonance width to be 3098 keV and 12 keV respectively are given in **Fig 6.5**. for illustration.

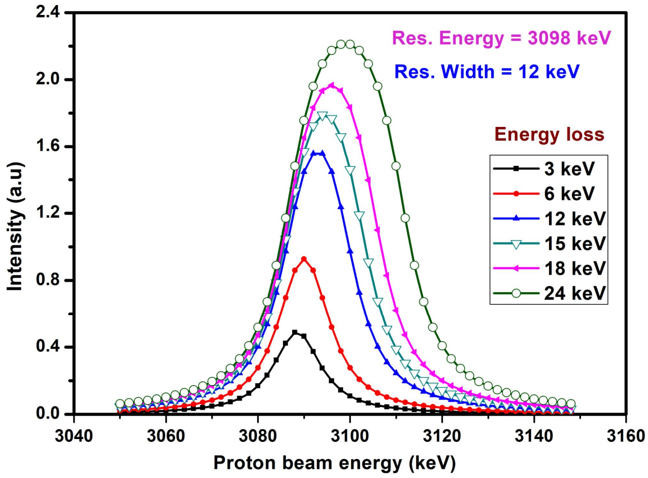

Fig. 6.5: *Theoretical γ-ray yield curves for the Si target*

6.7 Features of resonance: depth resolution, probing depth and limit of detection

Depth resolution, probing depth and limit of detection (LOD) are the three major attributes of a depth profiling methodology. The width of ~12 keV suggests that the depth resolution of the resonance is about 600 nm in Si and about 180 nm in uranium. The two elements are the typical representatives of light and heavy elements with significantly different physical densities. Since the reaction has no resonance below E_p= 3098 keV, but has one, no matter however weak, at 3337 keV, the resonance at 3098 keV has a probing depth of about 11 μm in Si and about 4 μm in uranium . So far as the LOD is concerned, it was calculated to be about 0.7 at.% from the thick target yield curve on the basis of 3σ (σ= standard deviation) of the baseline. The resonance apparently is not suitable for high resolution depth profiling. However this major limitation is, to a certain extent, compensated by a fairly large probing depth. In other words, the resonance is potentially applicable for large depth profiling of Si with rather coarse depth resolution.

6.8 Off-resonance cross-section: correction in yield

The prevalence of the off-resonance cross-section is indicated by the continuously increasing γ-ray yield in **Fig.6.2** in the intervening region between the resonances at 3098 keV and 3337 keV. Apparently while analysing thick films or bulk materials, the γ-yields at different energies must be corrected for the corresponding off- resonance contributions. For effecting the corrections, a factor F, synonymous with off-resonance cross section, was obtained from the thick target yield curve in **Fig.6.2** using the following formula

$$F_i = \frac{Y_i - Y_0 - \sum F_{i-1}.Y_0}{Y_0} \qquad (6.6)$$

where Y_0 is the γ-ray yield at the energy representing the beginning of the plateau region while Y_i is the yield at a higher energy i. It is to be noted the factor F can also be obtained from the yield curve of a thin film **(Fig.6.3)**. However due to very low counts in the off – resonance energy regions, a comparatively larger uncertainty is expected in the determination of the factor and hence is not considered for the quantitative analysis. Incidentally, the F factors determined from the two yield curves were in agreement within 30%.

6.9 Quantification and analysis of samples

The resonance was applied to several materials that included thin films of different thicknesses, for example Si_xN_y (110 nm)/GaAs and Si_xN_y (550 nm)/GaAs and also bulk compounds such as SiC single crystals in order to get a better insight into the analytical capabilities of the resonance. The first film typically represents a case wherein the thickness (i.e. ΔE) is much smaller than the width of the resonance while in the second, both are comparable. These are difficult scenarios as resonances are ideal for analysing thick films wherein ΔE is significantly larger than the width of the resonance i.e. the resonance occurs within the films at two or more energy steps beyond the resonance energy. Before embarking on the description of the methodology adopted for analysing the silicon nitride films, it is instructive to mention that the Si_xN_y (110 nm) and Si_xN_y (550 nm) films contain ~ 21 at % hydrogen. The content of hydrogen in the films was determined by $^{1}H(^{15}N, \alpha\gamma)^{12}C$ nuclear reaction that has a resonance at 6.385 MeV **[189]**. The films can therefore be represented by the general chemical formula $Si_xN_{1-(x+y)}H_y$.The content of Si in the films and in other samples as well, was determined by comparator method using elemental Si as the standard. This approach obviates the necessity of a priori knowledge of such parameters as σ_R, Γ or Ω appearing in the numerator of **equation (6.3)** which otherwise is the case if the fundamental method is employed for quantification. The content of x in the films can be calculated using the following expression which is obtained by combining **equations (6.3)** and **(6.5)**:

$$x = \frac{\pi^{-1} \cdot R \cdot M \cdot \varepsilon_{Si} - (1-y)\varepsilon_N + y\varepsilon_H}{\varepsilon_{Si} - \varepsilon_N} \qquad (6.7)$$

where R and M are defined by the expressions and ε is the stopping cross-section ($eV/10^{15}$ $atoms/cm^2$) of the element indicated in the subscript at the resonance energy

$$R = \frac{(Y_{Si})_{std}}{(A_{Si})_{film}} \qquad (6.8)$$

$$M = \int_0^{\infty} \left[\arctan \frac{E - E_R}{\Gamma/2} \right]_{E-\Delta E}^{E} dE \qquad (6.9)$$

Expressing more explicitly, R is the ratio of charge normalised thick target γ-ray yield for the standard and the area under the γ-ray yield curve of the film A_{Si} while M can be considered as the co-factor of the reaction cross-section in the film.

Table 6.1 lists the atomic composition of the two films determined using **equation (6.7)**. The parameter M for the films was determined by non-linear least square fitting using the Lorentzian function. The table also lists the thickness of the films expressed in terms of areal density ($at./cm^2$) and also in physical dimension(nm). The areal density of a film was determined by taking ΔE and its stopping cross-section (calculated on the basis of the atomic composition determined) into consideration. The thickness of the film in physical dimension was determined by dividing the areal density by its atomic density. It is to be noted that there exists a considerable scatter in the density of silicon nitride reported in literature [190]. The variations are more pronounced in films wherein the density depends on Si/N ratio and hydrogen content in a complex manner. The generally accepted density of bulk silicon nitride is 3.1 gm cm^{-3} while it ranges from 2.5 to 2.8 gm cm^{-3} for films **[190]**. Presently, the mean density (i.e. 2.65 gm cm^{-3}) has been used for the calculation of the thickness of the films. It can be observed that the determined thicknesses agree within 10% with the ellipsometric data.

Table 6.1: *Atomic composition and thickness of Si_3N_4 films*

Film	Atomic composition (at%)			Thickness	
	Si	N	H	Areal density (10^{18} atoms/cm^2)	Physical (nm)
Si_3N_4 (110 nm)	26	53	21	1.18	119
Si_3N_4 (500 nm)	34	45	21	5.26	529

The method was also employed for the determination of depth profiles of Si in specimens of SiC single crystals. The targets were irradiated with the beam at about 1° incident angle to avoid any accidental channelling. The depth distribution of Si in two different samples measured using this method is shown in the **Fig 6.6.**

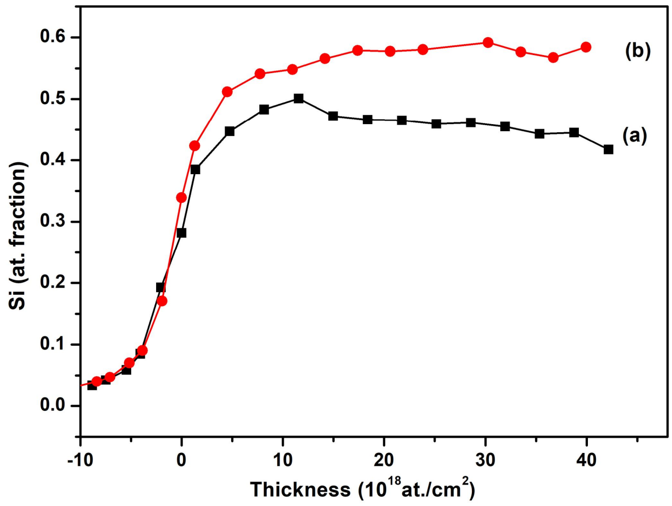

Fig. 6.6: *Depth profile of Si in SiC single crystals*

6.10 Conclusions

^{28}Si(p,p′γ)^{28}Si nuclear reaction that exhibits a resonance at 3098 keV and has a width of 12 keV is eminently suitable for the quantitative analysis of Si in thin films and for depth profiling the Si in thick targets including films and bulk materials. The method is simple and yields quantitative results with a combined uncertainty of < 10%.

Chapter 7

Summary and Future Research

7.1 Summary

Particle induced γ-ray emission (PIGE) is a prominent accelerator based ion beam analysis (IBA) technique for the elemental analysis of materials. It is based on the detection of prompt γ-rays emitted from nuclear reactions induced in a material on its irradiation with energetic charged particles. The particles are protons or α-particles, most often the former, with energy ranging from a few hundred keV to several MeV. The γ-rays are usually measured with high energy resolution using a semiconductor detector. The γ-ray producing reactions with the elements can be inelastic scattering, rearrangement collisions, radiative capture or Coulombic excitation. Accordingly, the basic principles underlying these reactions which are central to PIGE are described with suitable examples. Importantly, the experiments have been conducted with 0.4-4.1 MeV protons obtained from the 3 MV Tandetron (HVEE) at NCCCM, BARC, Hyderabad. The salient features of the accelerator and also the experimental set up that involves facilities for the irradiation of the materials in vacuum and equipments for the detection of the prompt γ-rays and charged particles are described.

The interaction of radiation with matter is of crucial importance in ion beam analysis. Herein, the radiation is usually of two kinds: charged particles and photons. The charged particles too have two sources: incident particles (projectiles) and those produced in a nuclear reaction (ejectiles). Importantly, the detection of the latter forms the basis of nuclear reaction analysis (NRA), a popular IBA technique for the characterization of materials. In fact, the technique has been employed for validating the experimental findings by PIGE on depth profiling of lithium and, therefore, the principles of NRA are elucidated comprehensively. Incidentally backscattering spectrometry, yet another prominent IBA technique, is based on the detection of (incident) particles scattered in the backward direction. This technique too has been used for validating the PIGE measurements on boron carbide and accordingly, the concepts underlying the technique too have been described. The photons, on the other hand can either be γ-rays or X-rays and their detection forms the basis, as is well known by now, of PIGE and particle induced X-ray emission (PIXE) respectively. Though PIXE has not been utilised in the present investigations, a brief description of the technique highlighting its analytical merits is presented. As a matter of fact, PIXE is often considered to be complementary to PIGE due to their sensitivity to elements in the different regions of the periodic table.

The charged particles, projectiles or ejectiles, lose their energy while traversing a medium. The loss of energy is defined in terms of stopping power or stopping cross-section and is of paramount importance for not only for designing an IBA experiment but also for qualitative and quantitative analyses. In fact, the non-invasive depth profiling capability of PIGE or NRA, probably one of the striking features of the two techniques that distinguishes them from other surface analytical techniques, has origin in the energy loss of the charged particles. Taking this into consideration, the concept of stooping power which is composed of nuclear and electronic stoppings, has been comprehensively elucidated. In this context, a brief description of the Stopping and Range of Ions in Matter (SRIM), a code to calculate the stopping power of an element or compound, is also presented along with several examples.

So far as the applicability of PIGE is concerned, it is, in general, sensitive to low Z elements though a few mid and high Z elements such as Cr, Mn, Fe, As, Hf, Au etc. can also be determined in percentage or sub-percentage levels. PIGE has two important analytical attributes: it can be utilized for the overall bulk determination of elements and, in favourable conditions, can also be employed for depth profiling purposes. The probing depth of PIGE, performed with about 4.0 MeV protons, can be a few tens of microns or even higher which, in a way, transcends the boundaries of surfaces and thus the emerging information can be considered to be the representative of the bulk. Depth profiling by, on the other hand, is performed using nuclear reactions that exhibit a strong, well isolated and narrow resonance in their excitation function. It must be explicitly emphasized that non-resonant γ-ray emitting nuclear reactions cannot be employed for depth profiling. The low Z elements such as Li, B, C , O and Si are major constituents of several technologically important materials that include energy materials such as $LiCoO_2$, $LiFePO_4$, oxide semiconductors or dielectrics namely SiO_2, ZnO, TiO_2, HfO_2, etc and materials used in nuclear energy such as boron carbide. PIGE has been utilized for the compositional analysis of these classes of materials. The studies entail the bulk determination of B/C ratio and also the determination of boron isotopic ratio in powered and sintered boron carbide ceramics, the depth profiling of Li in the Li-ion battery materials, the determination of bulk oxygen in oxide semiconductors and depth profiling of Si in silicon nitride and silicon carbide. The salient features of the methodologies developed and the major experimental findings are summarized below.

Lithium ion battery is a portable energy storage (electrochemical) device that is extensively used for powering different kinds of electronic gadgets. It is also being increasingly used in electric vehicles. The working of the LIB involves two steps: charging and discharging. The process of charging involves the movement of Li ions from a cathode, a Li based compound such as $LiCoO_2$, $LiFePO_4$ through an electrolyte which is also a Li containing compound, more often $LiPF_6$, to an anode, made generally of graphite while during discharging i.e. while powering the systems the Li ions move back to the cathode through the same path. Knowledge of the depth profile of Li in the cathode and anode wherein Li gets intercalated during charging, is important for designing batteries with improved capacity, energy density and cyclability. Neutron depth profiling with a probing depth of about 30μm has been the technique of choice for depth profiling Li in these materials. As an alternative to NDP which is conducted using neutron beams from a nuclear reactor and thus has limited access, two ion beam methodologies, one based on PIGE and another on NRA were developed and standardized for depth profiling Li in materials.

The PIGE method utilizes ^{7}Li(p,γ)^{8}Be proton capture reaction while the NRA method, 7Li(p,α)4He reaction. Depth profiling by ^{7}Li(p,γ)^{8}Be reaction is accomplished by the resonance at 441 keV and involves the measurement of 14.6 and 17.6 MeV γ-rays, characteristic of the reaction, by a NaI(Tl) detector. The method has a detection sensitivity of ~0.2 at.% and enables profiling up to a depth ≥20 µm with a resolution of ≥ 150 nm. The profiling to a fairly large depth is facilitated by the absence of any other resonance up to 1800 keV proton energy. The reaction has substantial off-resonance cross-sections. A procedure is deveoped for evaluating the off-resonance yields. Interferences from fluorine and aluminium are major limitation of this depth profiling methodology. The depth profile measurement by ^{7}Li(p,α)^{4}He reaction, on the other hand, utilises 2-3 MeV protons and entails the detection of α-particles at 90° or 150° angles. The reaction exhibits inverse kinematics at 150°. This method, too, suffers interference from fluorine due to the simultaneous occurrence of ^{19}F(p,α)^{16}O reaction. Kinematical considerations show that the interference is minimal at 90° and thus is the recommended angle of detection. The method is endowed with a detection sensitivity of ~ 0.1 at.%, a depth resolution of ~ 100 nm and a probing depth of about 30 µm in the absence and ~ 5 µm in the presence of fluorine in the material. Both methods yielded comparable depth profiles of Li in the cathode (lithium cobalt oxide) and the anode (graphite) of a Li-ion battery. The methods are comparable to NDP for depth profile measurements and also have potential for on line diffusion studies.

Boron carbide, a ceramic made essentially of low Z elements, has several attractive properties and thus applications in several fields. In nuclear energy, the material especially the one enriched with ^{10}B isotope is used in the manufacturing of control rods for the reactors. The isotopic ratio of B i.e. ^{10}B/ ^{11}B and B/C ratio influence the neutron absorption properties and physical characteristic of the material and thus are important considerations in designing the control rods for the different types of nuclear reactors. In order to determine $^{10}B/\ ^{11}B$ and B/C ratios in powder and also in sintered boron carbide a simple PIGE method was standardized. Performed at 4.0-4.2 MeV proton energy, the method utilizes $^{10}B(p,\alpha\gamma)^{7}Be$, $^{10}B(p, p'\gamma)^{10}B$ and $^{11}B(p, p'\gamma)^{11}B$ nuclear reactions for (a) the isotopic analysis of boron and (b) the determination of total boron, and $^{13}C(p,p\gamma)^{13}C$ nuclear reaction for the determination of carbon. The irradiation conditions were optimized by determining the thick targets yields of prompt γ-rays, characteristic of these reactions, in 3.0-4.2 MeV proton energy region. The quantitative analysis was performed by comparator method by making allowances for the attenuation of γ-rays in the specimens. The uncertainty in the determination of $^{10}B/^{11}B$ isotopic ratio and B/C atomic ratio is about 2% and about 5% respectively. The results were validated by proton elastic backscattering spectrometry (p-EBS) that utilises $^{10}B(p, p)^{10}B$, $^{11}B(p, p)^{11}B$ and $^{12}C(p, p)^{12}C$ elastic scatterings at ≥2.0 MeV proton energies. Incidentally p-EBS also provides information on the relative density of sintered boron carbide specimens. Though both PIGE and p-EBS can be used for analysis, the former with a probing depth of several tens of microns is the method of choice for bulk analysis while p-EBS is useful in discerning compositional variations in surface regions. The non-destructive nature and analytical potential make the methods suitable alternatives to chemical methods wherein the dissolution of the ceramic is difficult due to its pronounced chemical stability and high hardness.

The importance of the determination of oxygen stoichiometry in oxide materials is well known. It stems from the fact that an oxygen deficiency (ca. the nominal chemical stoichiometry) may bring about notable changes in the physical, chemical and structural properties of a material. In fact, some materials owe their properties to their oxygen deficient composition. In keeping with the requirements, several methods of oxygen determination have been developed over the years. These methods include ion beam analysis (IBA) methods as well. The IBA methods, however, are largely applicable to oxide films and have rather limited utility in the determination of bulk oxygen in powders and sintered bodies. In view of this shortcoming and the challenges faced by chemical methods, two PIGE methods with a potential to determine bulk oxygen with good accuracy and precision in wide ranging of oxygen bearing/oxide materials were developed.

The first method is based on $^{18}O(p,\alpha\gamma)^{15}N$ nuclear reaction and involves the measurement of 5.27 MeV γ-rays emitted following the de-excitation of ^{15}N nuclei. A treatment of the energetics of the reaction provides an insight into the origin of 5.27 MeV γ-rays. In addition, thick target γ- ray yields and the limits of detection are measured to ascertain the analytical potential of the reaction. The thick-target γ-ray yields are measured with a high purity germanium detector and a bismuth germanate detector at 0° as well as 90° angles in 3.0-4.2 MeV proton energy region. The best limit of detection of about 1.3 at.% is achieved at 4.2 MeV proton energy for measurements at 0° as well 90° angles with the bismuth germanate detector while the uncertainty in quantitative analysis is <8%. The reaction has a probing depth of several tens of microns. Interferences can arise from fluorine due to the occurrence of $^{19}F(p,\alpha\gamma)^{16}O$ reaction that emits 6-7 MeV γ-rays. The analytical potential of the methodology is demonstrated by determining oxygen in several oxide as well as non-oxide materials.

Another method that employs $^{18}O(p,p'\gamma)^{18}O$ nuclear reaction ($E\gamma = 1981$ keV) was standardized for determining bulk oxygen in materials. Performed with 3.8-4.0 MeV protons, the method has a detection sensitivity of about 1 and 5 at% in high Z and low or mid Z matrices respectively. It has a probing depth of 30-50 μm and is largely free from interferences. The method has been utilized in the analysis of a large number of binary (e.g. SiO_2, TiO_2), ternary (e.g. Li_2TiO_3, $LiCoO_2$) and multinary (e.g. $LiFePO_4$, $LiFePO_{4-x}F_x$)

oxides. The method has also been demonstrated to provide O/U ratio in sintered uranium oxide specimens with a precision of about 1 %. The method was further extended to the analysis of several electroceramics that included $BaTiO_3$, $BaTi_4O_9$, $Ba_2Ti_9O_{20}$, $BiFeO_3$, $CaMnO_3$ and more importantly $YBaCuO_7$. The method with its good analytical capabilities, non-destructive nature and suitability to a large number of simple and complex materials adequately fulfills the requirement of a simple, efficient and reliable method of oxygen determination in oxide materials.

Silicon is major constituent of several important semiconductors and dielectric materials. These materials, silicon carbide and silicon nitride, for example, are used as thin films or as bulk materials. For the determination of the content of silicon in a thin film and its thickness, and to determine the depth profiles of Si in the surface and the near surface regions of bulk materials, a PIGE methodology based on $^{28}Si(p,p'\gamma)^{28}Si$ nuclear reaction that emits 1778 keV characteristic γ-rays and exhibits a resonance at 3098 keV was developed. The related investigations involve the on recording the yield curves of the 1778 keV γ-rays for thin and thick targets in 3.0-4.1 MeV proton energy energy region and a comprehensive theoretical treatment of thin and thick targets yields for resonances using Breit-Wigner formula. The width of the resonance was estimated by way of simulation to be about 12 keV. The resonance has a depth resolution of about 600 nm and probing depth of about 11 μm in silicon. The method has been employee for determining the composition and thickness of silicon nitride films (110nm and 550nm) and for depth profiling Si in the near surface regions of silicon carbide crystals.

7.2 Future research

Ion beam analysis is an active research area. It's capability to examine low Z elements non-destructively in thick / thin targets can be advantageously utilized for many applications. The present investigations can be extended to the following areas.

1. Measurement of differential cross-section of $^{10}B(p,p'\gamma)^{10}B$ and $^{11}B(p,p'\gamma)^{11}B$ reactions using ^{11}B and ^{10}B- enriched thin targets. It would enable the determination of boron and $^{10}B/^{11}B$ isotopic ratio in thin and also in intermediate thick samples. As a result, the coatings of boron carbide can be analysed. Such coatings have applications as neutron detectors.
2. The high resolution γ-ray spectrum from $^{18}O(p,\alpha\gamma)^{15}N$ has complex structure. Though the factors responsible for the complexity have been described, a comparator simulation of the spectrum is desirable as it would give a better insight into the processes involved. The theoretically generated response functions vis a vis experimental parameters and detector features would help in more precise measurements.
3. The present studies have shown that PIGE technique is sensitive to ^{13}C and ^{18}O isotopes. Hence the technique can be extended to probe carbon or oxygen metabolism in favorable case. Such an application would also enable its extension into Bio-photovoltaics which is an emerging field in the area of non-conventional sources of energy.